論文 / 著書情報
Article / Book Information

題目(和文)	
Title(English)	Fukushima Revitalizics: Performance Evaluation of High-powered Battery for Nuclear Decommissioning and Heat Storage
著者(和文)	張煒辰
Author(English)	Weichen Zhang
出典(和文)	学位:博士(工学), 学位授与機関:東京工業大学, 報告番号:甲第12907号, 授与年月日:2024年9月20日, 学位の種別:課程博士, 審査員:木倉 宏成,小林 能直,赤塚 洋,相樂 洋,筒井 広明
Citation(English)	Degree:Doctor (Engineering), Conferring organization: Tokyo Institute of Technology, Report number:甲第12907号, Conferred date:2024/9/20, Degree Type:Course doctor, Examiner:,,,,
学位種別(和文)	博士論文
Type(English)	Doctoral Thesis

Fukushima Revitalizics: Performance Evaluation of High-powered Battery for Nuclear Decommissioning and Heat Storage

Doctoral Dissertation by:

Zhang Weichen

Of the degree of

Doctor of Engineering

Academic advisor: Assoc. Prof. Hiroshige KIKURA

Department of Nuclear Engineering, Graduate School of Science and Engineering

Tokyo Institute of Technology

September 2024

Contents

List of Figures

List of Tables

Chapter 1

Chapter.1 Introduction

1.1 Background

1.1.1 Impact of the TEPCO Fukushima Daiichi Nuclear Power Plant Accident

The Great East Japan Earthquake, which occurred on March 11, 2011, with a magnitude of 9.0, triggered a massive tsunami that resulted in a severe accident at the Tokyo Electric Power Company Holdings (TEPCO) Fukushima Daiichi Nuclear Power Plant (1F). This accident not only caused a radiation disaster but also had widespread societal impacts (**Figure 1.1**). The meltdown of the reactors released a significant number of radioactive materials into the environment, leading to extensive environmental contamination and substantial effects on the local community. Long-lived radionuclides such as Cesium-137 and Iodine-131 posed significant issues [1-1].

The Fukushima Daiichi accident had profound impacts both domestically and internationally. Approximately 160,000 residents around the disaster area were forced to evacuate [1-2], many of whom have been living in evacuation for extended periods (**Figure 1.2**). Concerns over health risks from radioactive contamination have been raised, with reports indicating an increase in thyroid cancer incidence [1-3]. Additionally, there have been considerable impacts on mental health, with many evacuees experiencing long-term stress and anxiety [1-4].

The local economy suffered devastating blows, significantly affecting primary industries such as agriculture, fisheries, and tourism [1-5]. The stigma surrounding Fukushima-produced agricultural and marine products persists, complicating economic recovery efforts. In response, various initiatives have been undertaken to support local industry recovery, including events promoting local produce and crafts and efforts to establish regional brands [1-6]. There are numerous challenges concerning radiation protection measures, emphasizing the importance of health management and mental healthcare for evacuees [1-7]. Long-term health risk assessment and monitoring, particularly for residents in affected areas, are crucial, necessitating the strengthening of regional healthcare services [1-8]. Furthermore, the regeneration of local communities and enhancement of social cohesion remain critical issues.

1.1.2 Current Status and Challenges of Fukushima's Reconstruction

Several significant developments have been observed in the reconstruction of Fukushima. The evacuation order areas are gradually being lifted, and some residents have returned, though the return rate remains low, with many still living as evacuees. Support measures for returning residents include housing reconstruction, infrastructure development, and job creation, yet many challenges persist [1-9].

Infrastructure reconstruction is ongoing, but the overall living environment has not fully recovered. Particularly in areas affected by radiation, decontamination efforts continue but have limitations, making complete decontamination challenging. The disposal and management of radioactive waste are also crucial issues, requiring the establishment of safe and effective methods [1-10].

Decommissioning the reactors requires advanced technology and long-term efforts, with numerous technical challenges still unresolved. High-performance, radiation-resistant batteries are essential for robots working in high-radiation environment [1-11]. Remote-operated and autonomous robots are being increasingly utilized, improving efficiency and safety in decommissioning tasks.

The effective use of renewable energy is vital for sustainable reconstruction in Fukushima [1-12]. Technologies enabling the use of solar and wind power during nighttime or low wind conditions are particularly necessary.

Given these circumstances, advanced technology and long-term efforts are essential for Fukushima's reconstruction, necessitating international cooperation and knowledge sharing. "Fukushima Revitalizics," an interdisciplinary research field focused on disaster recovery, is crucial for promoting sustainable development and community regeneration.

1.2 The Necessity of Fukushima Revitalizics

1.2.1 Definition and Significance of Revitalizics

The Fukushima Daiichi Nuclear Power Plant accident was not just a radiation disaster; it had widespread social and economic impacts. Recovering from such a large-scale disaster requires an interdisciplinary approach, integrating multiple fields of study. This gave rise to "Fukushima Revitalizics," a new academic discipline designed to support disaster recovery both academically and practically (**Figure 1.3**).

Fukushima Revitalizics is an interdisciplinary academic field dedicated to the restoration and revitalization of the Fukushima region following the Great East Japan Earthquake and subsequent nuclear disaster. This field integrates risk communication, environmental recovery, robotics engineering, educational programs, industrial promotion, community rebuilding, and social experimentation to create a comprehensive framework for sustainable development and disaster resilience (**Figure 1.4**).

Core elements of Fukushima Revitalizics include:

1. Renewable energy

Collaborative Projects

Fukushima Revitalizics engages in collaborative projects with local governments and industries to promote economic revitalization. These projects include partnerships with businesses to develop renewable energy solutions and other innovative technologies that support regional recovery and growth. For example, collaborations focus on solar thermal heat storage and hydrogen energy solutions, aiming to develop sustainable energy sources that can be locally produced and consumed, fostering economic resilience and energy independence.

Research and Development

Research is conducted on various aspects of industrial revitalization, including the development of new technologies and processes that enhance local industries' productivity and sustainability. These efforts are designed to create a robust industrial base that can support long-term regional recovery and economic growth.

2. Education and Human Resource Development

Student and Resident Education

Fukushima Revitalizics includes educational programs designed for various demographic groups, including students and local residents. These programs encompass courses in nuclear engineering, thermal-fluid dynamics, and risk communication engineering. For instance, courses such as "Nuclear Engineering Seminar" and "Thermal Fluid and Risk Communication Engineering Experiments" are offered to university students as part of their formal education.

Practical Training and Internships

The field places a strong emphasis on practical training and hands-on experience. Internships and practicums are organized for university students and graduate students to engage in activities such as ultrasonic testing and non-destructive testing (NDT) to understand the reliability and accuracy of risk detection methods. These practical experiences are crucial for developing the skills necessary to address the complex challenges associated with nuclear disaster recovery.

Community Education Programs

Educational initiatives also target younger students and local residents. Programs such as science classes and robotics workshops are aimed at elementary and middle school students, while community education efforts focus on enhancing residents' understanding of disaster recovery and risk management.

3. Social Experimentation

Integration of Academic Knowledge

Fukushima Revitalizics integrates academic research with practical applications through social experimentation. This involves testing and implementing research findings in real-world settings to evaluate their effectiveness and refine methodologies. For example, social experiments might include community-based projects that apply new decontamination techniques or renewable energy solutions.

Collaboration with Local Enterprises

Collaborative efforts with local enterprises and governments are crucial for the successful implementation of reconstruction strategies. These partnerships enable the practical application of research outcomes, contributing to the overall goal of regional revitalization and sustainable development. Social experiments often involve pilot projects that test new technologies or approaches in collaboration with local businesses and community organizations.

4. Risk Communication Engineering

Development of Risk Communication Engineering

A key component of Fukushima Revitalizics is the development of risk communication engineering. This involves creating methods and tools to effectively communicate the risks associated with radiation exposure to local communities, thereby helping residents understand and manage these risks. The goal is to restore a sense of safety and security among the residents of Fukushima by making complex risk information accessible and comprehensible.

Non-Destructive Testing and Risk Visualization

Non-destructive testing, particularly ultrasonic flaw detection, is employed to detect minute cracks in metal pipes, which is used as a model for teaching risk communication. Students learn to interpret and communicate the statistical reliability of their findings, enhancing their ability to explain technical information transparently and effectively.

5. Decontamination Science

Development and Application

Environmental recovery efforts are central to Fukushima Revitalizics. Decontamination science is developed and applied to address the various contaminants resulting from the nuclear disaster. Research focuses on identifying and optimizing decontamination methods based on the composition and characteristics of different contaminated materials.

Collaboration with Research Institutions

The field collaborates with institutions such as the Fukushima Environmental Creation Center and the Collaborative Laboratories for Advanced Decommissioning Science (CLADS) to advance decontamination technologies. These partnerships aim to develop effective strategies for environmental restoration and sustainable recovery.

6. Robotic Measurement Engineering

Advancement of Decommissioning Research

Robotic measurement engineering is a critical area within Fukushima Revitalizics. This research promotes the development of advanced robotic sensors and underwater robots, which are essential for the decommissioning of nuclear facilities. The goal is to create innovative tools and techniques that can safely and efficiently manage the decommissioning process.

Practical Experiments and Fieldwork

Fieldwork and practical experiments are conducted in collaboration with local institutions and research centers, such as the Japan Atomic Energy Agency's Naraha Remote Technology Development Center. These activities include the application of robotic technologies in real-world settings to gather data and refine methodologies.

1.2.2 Structure of Fukushima Revitalizics

In planning and implementing post-disaster recovery efforts, Fukushima Revitalizics requires a systematic and orderly framework to effectively integrate and manage diverse revitalization projects. Therefore, we have divided the revitalization work into three parts: Front End, Inner, and Back End. This classification helps to clarify the priority of each project, the order of implementation, and their interrelationships, ensuring a coordinated and efficient overall recovery process.

The Front-end projects focus on renewable energy. These are the first steps in the revitalization work and represent the most direct and visible outcomes. These projects can quickly attract investment and public attention, generating economic and social benefits and laying a solid foundation for subsequent work.

The inner projects mainly involve education and human resource development and social experimentation, which are the central elements of the revitalization efforts. Through education and training, we aim to improve the knowledge and skills of local residents, ensuring that they can actively participate in and support the revitalization efforts and are equipped to face future challenges.

The Back-end projects focus on risk communication engineering, decontamination science, and robotic measurement engineering, which are the most technically complex and challenging parts. These projects require highly specialized knowledge and technology to ensure that long-term environmental and health risks posed by the nuclear disaster are resolved in a safe and sustainable manner.

In this research, Front-end and Back-end are focused and supply technological solutions for Fukushima Revitalizics.

1.3 Importance and Current Status of Renewable Energy Utilization (Front End)

1.3.1 Importance and Characteristics of Renewable Energy

Renewable energy is increasingly important in modern society as an environmentally friendly and sustainable energy source. Following the Fukushima Daiichi Nuclear Power Plant accident, the introduction of renewable energy has become crucial for the recovery and sustainable development of the Fukushima region [1-13]. Renewable energy mainly includes solar power and wind power, each with unique characteristics and advantages.

Solar power converts sunlight directly into electricity, producing no carbon dioxide during generation, making it a very clean energy source. Many solar power facilities have been installed in Fukushima Prefecture since the earthquake [1-14], contributing to the region's energy supply (**Figure 1.5**). Solar power depends on daylight hours, so generation decreases at night or during cloudy weather, but technological advancements are continuously improving efficiency.

Wind power generates electricity by rotating turbines with wind energy, primarily through onshore and offshore wind farms. Wind power projects are progressing along the coast of Fukushima Prefecture, playing a vital role in renewable energy [1-15]. Wind power generation fluctuates with wind speed, requiring storage technology or combinations with other energy sources for stable supply.

The introduction of renewable energy offers various benefits for Fukushima's recovery, including reducing environmental impact, increasing energy self-sufficiency, revitalizing the local economy, and providing stable energy supply. Renewable energy generation produces minimal greenhouse gases, contributing to climate change mitigation. In Fukushima, renewable energy proliferation is expected to reduce environmental impact. Local energy production contributes to stable energy supply and local economic revitalization.

Moreover, introducing renewable energy creates new employment opportunities and fosters the development of related industries, contributing to local economic revitalization [1-16]. In Fukushima, numerous renewable energy projects have been launched, supporting regional economic growth. The diverse use of renewable energy diversifies energy supply, enabling risk dispersion during disasters. This enables the Fukushima region to build a disaster-resilient energy system.

As part of Fukushima Revitalizics, understanding the importance and characteristics of renewable energy and providing energy solutions suitable for the local community is crucial. Continued technological innovation and policy support are expected to advance the introduction of renewable energy, promoting efforts toward a sustainable society.

1.3.2 Importance of Heat Storage System

Heat storage systems play a crucial role in the realm of renewable energy. As shown in **Figure 1.6**, these systems are designed to collect and store surplus electricity generated from renewable sources, such as solar and wind power, by converting it into thermal energy. This stored thermal energy can then be used during periods when there is insufficient sunlight, such as at night, or when wind conditions are not favorable for wind power generation. By effectively managing energy supply and demand, heat storage systems ensure a reliable and continuous energy supply [1-17]. They can reconvert the stored thermal energy back into electricity to meet power needs or directly provide heat for various applications. This capability makes heat storage systems indispensable in optimizing the use of renewable energy sources, enhancing grid stability, and reducing dependence on fossil fuels.

There are several types of heat storage system, such as molten salt thermal energy storage, water thermal energy storage, paraffin thermal energy storage and phase change material (PCM) thermal energy storage, the advantages and disadvantages are shown in **Table 1.1**. These heat storage methods are often hindered by their high costs, which significantly limit their widespread adoption. These systems are expensive due to the cost of materials and the need for advanced technology to maintain efficiency. Molten salt systems, for instance, require costly corrosion-resistant materials and high-temperature operation management. Water storage systems need extensive insulation to prevent heat loss and sophisticated designs to avoid freezing in cold climates, both of which add to the overall expense. Paraffin storage systems suffer from low thermal conductivity and the high cost of high-purity paraffin, as well as the need to accommodate significant volume changes during phase transitions. PCM systems, while efficient, involve expensive materials and require precise thermal management to ensure effective phase changes. Additionally, issues such as low thermal conductivity, potential thermal degradation, and complex system integration further complicate their implementation. Consequently, the high initial investment and operational costs overshadow their technical benefits, making these storage systems financially challenging to deploy on a large scale.

For considering these disadvantages, stone heat storage system is focused in this research. The advantages compared with other kinds of heat storage system are:

1. Cost-Effectiveness: One of the most compelling reasons to choose a stone heat storage system is its affordability. Stones are naturally abundant and inexpensive, which significantly reduces the overall installation costs compared to other storage materials like molten salts, paraffin, or phase change materials (PCMs). The low material costs, coupled with simpler infrastructure requirements, make stone heat storage a financially viable option for large-scale applications. This cost efficiency allows for broader adoption and scalability, making it an attractive choice for both small and large-scale energy storage projects.

2. Minimal Environmental Impact: Stone heat storage systems are also environmentally friendly. Stones are a natural and readily available resource, and their use does not involve the extraction of rare or hazardous materials. This results in a low environmental footprint both in terms of resource extraction and end-of-life disposal. Unlike some chemical storage systems that can pose environmental risks, stones do not degrade or release harmful substances over time. This sustainability factor aligns well with the principles of green energy and supports the goal of reducing the overall environmental impact of energy storage solutions.

3. System Stability: The stability and reliability of stone heat storage systems are significant advantages. Stones are chemically inert and physically stable, making them an excellent medium for long-term thermal energy storage. They can withstand repeated heating and cooling cycles without significant wear or degradation, ensuring consistent performance over many years. Additionally, stone heat storage systems require minimal maintenance compared to other systems that may involve complex mechanical or chemical processes. This stability reduces operational costs and enhances the reliability of the energy storage system, providing a dependable solution for managing energy supply and demand.

In conclusion, stone heat storage systems offer a combination of cost-effectiveness, environmental sustainability, and system stability. These attributes make them an excellent choice for integrating renewable energy sources, ensuring reliable and efficient energy storage, and contributing to a sustainable energy future.

1.4 Importance and Current State of Decommissioning Technology (Back End)

1.4.1 Overview of the Decommissioning Process

The decommissioning process refers to a series of operations conducted after the shutdown of a nuclear power plant. Initially, the reactor is safely shut down, and spent fuel is cooled. Cooling is crucial to remove radioactive decay heat and maintain the fuel in a stable state. This stage requires stable operation of cooling systems and concentration of technical and human resources. Next, the spent fuel is removed and transferred to appropriate storage facilities. This step involves thorough radiation protection measures to minimize worker exposure [1-18].

Once fuel removal is completed, decontamination of equipment and buildings containing radioactive materials is performed. Decontamination is essential to minimize worker exposure and reduce environmental radiation levels [1-19]. Advanced technology and efficient progress using the latest techniques and equipment are required for effective decontamination. Following decontamination, the dismantling of the reactor and associated facilities takes place, necessitating proper handling and management of radioactive waste to ensure a safe decommissioning process.

In the final stage, the site is restored to a reusable state, including environmental regeneration and sustainable land use planning. Throughout the decommissioning process, safety management and environmental protection are prioritized, necessitating technical challenges and meticulous planning.

1.4.2 Advances in Decommissioning Robot Technology

Advances in robot technology play a crucial role in the decommissioning work at Fukushima Daiichi [1-20]. Due to the extreme danger of high-radiation environments, remote-controlled and autonomous robots are employed. These robots are designed to inspect the interior of reactors and perform decontamination and dismantling tasks.

Advancements in robot technology have made it possible to perform tasks that were previously difficult for humans, significantly improving the safety and efficiency of the decommissioning process. For instance, TEPCO's "scorpion-type robot" demonstrates high maneuverability in confined spaces and complex terrains, supporting operations in high-radiation environments. This robot is equipped with cameras and sensors, allowing real-time monitoring and data collection from the site [1-21].

International cooperation and technology sharing are also advancing. The International Atomic Energy Agency (IAEA) collaborates with nuclear agencies and research institutions worldwide to provide technical support for the decommissioning work at Fukushima Daiichi [1-22]. This allows the latest robotic technologies and know-how to be utilized in Fukushima's decommissioning efforts (**Figure 1.7**).

The introduction of AI (Artificial Intelligence) and machine learning is also significant in the advancement of robot technology. AI-equipped robots can recognize environments in real-time and autonomously select optimal work routes, enhancing efficiency and safety. For example, AI technology enables robots to plan routes that avoid high-radiation areas and proceed autonomously with tasks.

Furthermore, "swarm control technology," where multiple robots with different functions work collaboratively, is gaining attention. This technology improves overall work efficiency by having different robots perform specific tasks [1-23]. For example, some robots conduct inspections and data collection, while others handle decontamination and dismantling.

Advances in robot technology are not limited to the decommissioning work at Fukushima Daiichi but are also applied to other nuclear facilities and tasks in radiation environments worldwide (**Figure 1.8**). This enables safe and efficient decommissioning processes globally. Additionally, the experience and technology from Fukushima are expected to play a crucial role in responding to future nuclear disasters.

To achieve efficient utilization of robots for waste removal, a high-performance battery is indispensable.

1.4.3 The Role of High-Performance Batteries

High-performance batteries are essential for decommissioning robots to operate for extended periods in high-radiation environments. According to the “Progress and Future Approach of Related Measures for the Battery Industry Strategy” which is announced by the Ministry of Economy in Japan, the definition of high-performance battery is shown in **Table 1.2**. In order to reach the definition of high-performance battery, in this research, the latest technology which is called the all-solid-state battery (ASSB) is taken into consideration. The performance comparison of formal lithium battery and ASSB is shown in **Table 1.3**. From the comparison, ASSB almost reach the definition of high-performance battery which is announced by the Ministry of Economy in Japan.

Solid-state batteries offer numerous advantages, making them a highly promising energy solution for various applications. Firstly, as shown in **Figure 1.9**, solid-state batteries use solid electrolytes instead of the liquid electrolytes found in traditional lithium-ion batteries, significantly enhancing safety by reducing the risks of leakage and fire [1-24]. Secondly, they have higher energy density, meaning they can store more energy for the same volume or weight, thus extending the operational time of devices. Additionally, solid-state batteries have a longer cycle life, maintaining performance over many charge and discharge cycles, making them suitable for applications requiring long-term reliable power.

However, despite these advantages, the performance of solid-state batteries under high radiation conditions still needs to be studied. High-radiation environments, such as those found in nuclear power plants and space applications, pose significant challenges to the stability and lifespan of battery materials. Specifically, the structural integrity and electrical stability of solid-state batteries under radiation need thorough investigation. Understanding the chemical and physical changes that occur in solid-state batteries under radiation is crucial for ensuring their reliable operation in such demanding conditions.

1.5 Research Objectives and Structure

1.5.1 Research Objectives

The overall objective of this study is to focus on both the Front-end and Back-end of Fukushima Revitalizics, providing practical technological solutions for its advancement. Specifically, the research focuses on the following three key areas:

1. Performance evaluation of heat storage system using Local Thermal Non-Equilibrium (LTNE) model:

The objective is to clarify the importance and applicability of gravel heat storage systems as an effective means of utilizing wind and solar power during nighttime or periods of weak wind. By applying the LTNE model for heat transfer simulations, the study investigates the heat storage efficiency of gravel heat storage furnaces. The focus is on designing and manufacturing a test heat storage furnace based on the LTNE model, providing a detailed analysis of heat exchange between fluids and solids, and verifying the accuracy of this simulation method. This aims to provide efficient thermal energy storage solutions for energy management in the Fukushima region.

2. Performance Evaluation of All-Solid-State Batteries using Pulsed Ultrasound:

The objective is to develop a pulsed ultrasound transmission time difference evaluation method for assessing the charge and discharge characteristics of all-solid-state batteries. By vertically installing ultrasonic sensors in a laminated all-solid-state battery and measuring the displacement of ultrasonic reflection waveforms between electrodes during charging and discharging, the method enables non-destructive monitoring of internal structural changes in the battery. The aim is to establish a new method for real-time monitoring of battery health, improving battery management systems, and providing a reliable evaluation tool for high-performance battery technology used in robots for nuclear debris removal.

3. Radiation Resistance Evaluation of All-Solid-State Batteries:

The objective is to evaluate the radiation resistance of all-solid-state batteries to determine their applicability in equipment such as decommissioning robots. By conducting experiments in high-radiation environments and using potential measurement evaluation methods and pulsed ultrasound transmission time difference evaluation methods, the study investigates the electrical performance and structural stability of all-solid-state batteries under different radiation levels. The goal is to provide scientific evidence to ensure the stable operation of all-solid-state batteries in high-radiation environments in the Fukushima region, supporting nuclear waste management and decommissioning operations.

1.5.2 Structure and Overview of Each Chapter

The structure flow of this research is shown in **Figure 1.10**. This research consists of five chapters: Chapter 1 "Introduction," Chapter 2 "Performance Evaluation of Heat Storage System using Local Thermal Non-Equilibrium Model," Chapter 3 "Performance Evaluation of All-Solid-State Batteries using Pulsed Ultrasound," Chapter 4 "Radiation Resistance Evaluation of All-Solid-State Batteries," and Chapter 5 "Conclusion."

Chapter 1 "Introduction": This chapter outlines the background of the research, the necessity of Fukushima

Revitalizics, the importance of decommissioning and renewable energy technologies.

Chapter 2 "Performance Evaluation of Heat Storage System using the Local Thermal Non-Equilibrium Model": This chapter elucidates the importance and applicability of stone heat storage systems. It uses the LTNE model to conduct heat transfer simulations and evaluate the efficiency of heat storage tank.

Chapter 3 "Performance Evaluation of All-Solid-State Batteries using Pulsed Ultrasound ": This chapter focuses on developing a pulse ultrasonic propagation time difference evaluation method to assess the charge-discharge characteristics of all-solid-state batteries.

Chapter 4 "**Radiation Resistance Evaluation of All-Solid-State Batteries**": This chapter clarifies the significance of all-solid-state batteries for decommissioning robots, particularly their radiation resistance. It includes experimental evaluations of their performance in high-radiation environments.

Chapter 5 "**Conclusions**": This chapter summarizes the findings from each chapter, discusses the practical implications of the research for Fukushima Revitalizics, and outlines the future direction of research.

By addressing these areas, this research aims to contribute to the sustainable recovery and technological advancement necessary for the revitalization of Fukushima.

References

[1-1] Victor Winiarek, Marc Bocquet, Olivier Saunier, Anne Mathieu, Estimation of errors in the inverse modeling of accidental release of atmospheric pollutant: Application to the reconstruction of the cesium-137 and iodine-131 source terms from the Fukushima Daiichi power plant.(2012)Atmospheres, Vol.117

[1-2] Hasegawa reiko, Disaster Evacuation from Japan's 2011 Tsunami Disaster and the Fukushima Nuclear Accident, (2013)IDDRI,

[1-3] Shunichi Yamashita, Shinichi Suzuki, Satoru Suzuki, Hiroki Shimura, and Vladimir Saenko, Lessons from Fukushima: Latest Findings of Thyroid Cancer After the Fukushima Nuclear Power Plant Accident, (2018) Thyroid, Vol.28

[1-4] Masaharu Maeda, MD, Mental Health Consequences and Social Issues After the Fukushima Disaster, (2017)Asia Pacific Journal of Public Health, Vol.29, pp.36-46.

[1-5] Bachev Hrabrin, Socio-economic and environmental impacts of match 2011 earthquake, tsunami and fukushima nuclear accident in Japan, (2014) ASERS Publishing, Vol.2, pp.127-222.

[1-6] Nana kaneko, Reconstituting Communities: Localized Folk Performing Arts and Matsuri Festivals in Post3.11 Japan, (2020)Sustainable Future for Human Security, Vol.7, pp.2-11.

[1-7] Becker, Steven M., The Fukushima Dai-Ichi Accident Additional Lessons from a Radiological Emergency Assistance Mission, (2013) Health physics, Vol.105, pp.455-461.

[1-8] Shuhei Nomura1, Marta Blangiardo, Masaharu Tsubokura, Akihiko Ozaki, Tomohiro Morita, Susan Hodgson, Postnuclear disaster evacuation and chronic health in adults in Fukushima, Japan: a long-term retrospective analysis, BMJ journals, Vol.6, pp.1-11.

[1-9] Xuan Bien Do, Return migration after the Fukushima Daiichi nuclear disaster: the impact of institutional and individual factors, (2020)Disasters, Vol.44, pp.569-595.

[1-10] Joonhong Ahn, Cathryn Carson, Mikael Jensen, Kohta Juraku, Shinya Nagasaki, Satoru Tanaka, (2015)Reflections on the Fukushima Daiichi Nuclear Accident.

[1-11] Yinlin Chang, Shuliang Zou, Guang Lin, Dewen Tang, Cuiyue Wei, Shoulong Xu, Research on Radiation Damage and Reinforcement of Control and Sensing Systems in Nuclear Robots, (2024) Electronics, Vol.13, 1214.

[1-12] Julia Nesheiwat, Jeffery S. Cross, Japan's post-Fukushima reconstruction: A case study for implementation of sustainable energy technologies, (2013) Energy Policy, Vol.60, pp.509-519.

[1-13] Hui Zhang, Chris Dolan, Si Meng Jing, Justine Uyimleshi, Peter Dodd, Bounce Forward: Economic Recovery in Post-Disaster Fukushima, (2019) susyainability, Vol.11, 6736.

[1-14] K.Muraoka, Energy situations in Japan before and after the Fukushima nuclear accident, (2015) EPJ Web of Conferences, Vol.98, 05003.

[1-15] Izumi Ushiyama, (2019) Wind Energy Programme in Japan, pp.41-62.

[1-16] K.Kaygusuz, Energy services and energy poverty for sustainable rural development, (2011) Renewable and Sustainable Energy Reviews, Vol.15(2), pp.936-947.

[1-17] Gang li, Xuefei Zheng, Thermal energy storage system integration forms for a sustainable future, Renewable and Sustainable Energy Reviews, Vol.62, pp.736-757.

[1-18] M.Laraia, 2 - Overview of nuclear decommissioning principles and approaches, (2012) Nuclear Decommissioning, pp.13-32.
[1-19] Yamamoto, Loren G. MD, MPH, MBA, Risks and Management of Radiation Exposure, (2013) Pediatric Emergency Care, Vol.29, pp.1016-1026.
[1-20] Naoki Mizuno, Yuichi Tazaki, Tatsuya Hashimoto, Yasuyoshi Yokokohji, A comparative study of manipulator teleoperation methods for debris retrieval phase in nuclear power plant decommissioning, (2023) Advanced Robotics, Vol.37, pp.541-559.
[1-21] Shota Yamaguchi, Kenji Iseya, Kazuma Kobayashi, Satoshi Mitsui, Toshifumi Satake, Naoki Igo, Decommissioning Robot Retrieves Fuel Debris from High Altitude, (2021) IEEE International Conference on Agents (ICA).
[1-22] Patrick O'Sullivan, Vladan Ljubenov, IAEA activities on decommissioning, (2014) International nuclear safety journal, Vol.3, No.4.
[1-23] Dengxiu Yu, Jiacheng Li, Zhen Wang, Xuelong Li, An Overview of Swarm Coordinated Control, (2024) IEEE Transactions on Artificial Intelligence, Vol.5, pp.1918-1938.
[1-24] Longfei Han, Li Wang, Zonghai Chen, Yongchun Kan, Yuan hu, Hao Zhang, Xiangming He, Incombustible Polymer Electrolyte Boosting Safety of Solid-State Lithium Batteries: A Review, (2023) Advanced functional materials, Vol.33, Issue 32, 2300892.

Table 1.1 Types and characteristics of heat storage systems

Types of thermal energy storage systems	Storage Material	Advantages	Disadvantages
Molten salt thermal energy storage	Molten salt	･High energy density ･Usable at high temperatures	･High cost ･Corrosion issues
Water thermal energy storage	Water	･Inexpensive ･Simple technology	･Low energy density ･Requires amounts of water
Paraffin thermal energy storage	Paraffin wax	･High energy density ･Usable at moderate temperatures	･High cost ･Limited temperature range
PCM thermal energy storage	Phase change from solid to liquid	･High energy density ･ Compact	･High cost ･Requires complex control

Table 1.2 Definition of high-performance battery

Performance	Details
Energy Density	Twice the current energy density (700-800 Wh/L or higher)
Safety	Reduce the risk of ignition and leakage by not using flammable electrolytes
Rapid Charge	Enable rapid charging with high current to reduce charging time (1/3 of Li-ion)
Aging degradation	Extend the lifespan through the development of highly durable electrodes and cells

Table 1.3 Definition of high-performance battery

Performance	Lithium Battery	All-Solid-State Battery (JD Power)
Energy Density	150-350Wh/L	400-900Wh/L
Safety	Liquid electrolyte	Solid electrolyte
Rapid Charge (C rate)	1C-6C	0.2C-20C
Aging degradation	300-500Cycles	300-11000 Cycles

Fig.1.1 The damage led to nuclear meltdowns and a number of hydrogen explosions

Fig.1.2 Residents around the disaster area were forced to evacuate

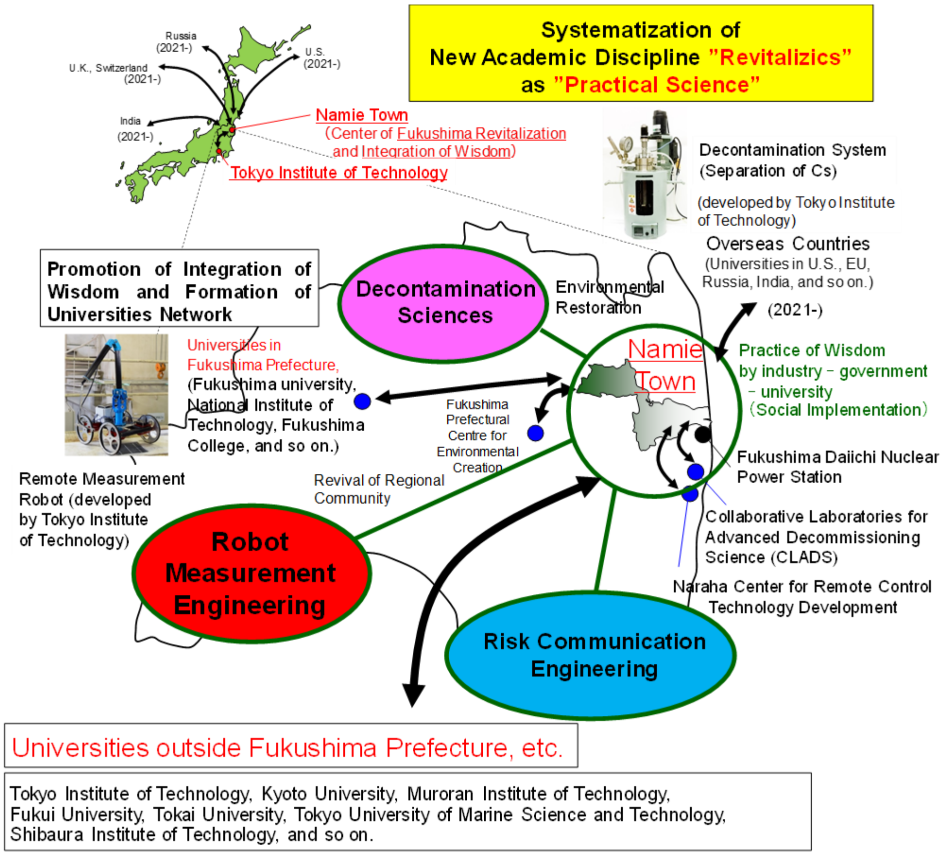

Fig.1.3 Fukushima Revitalizics

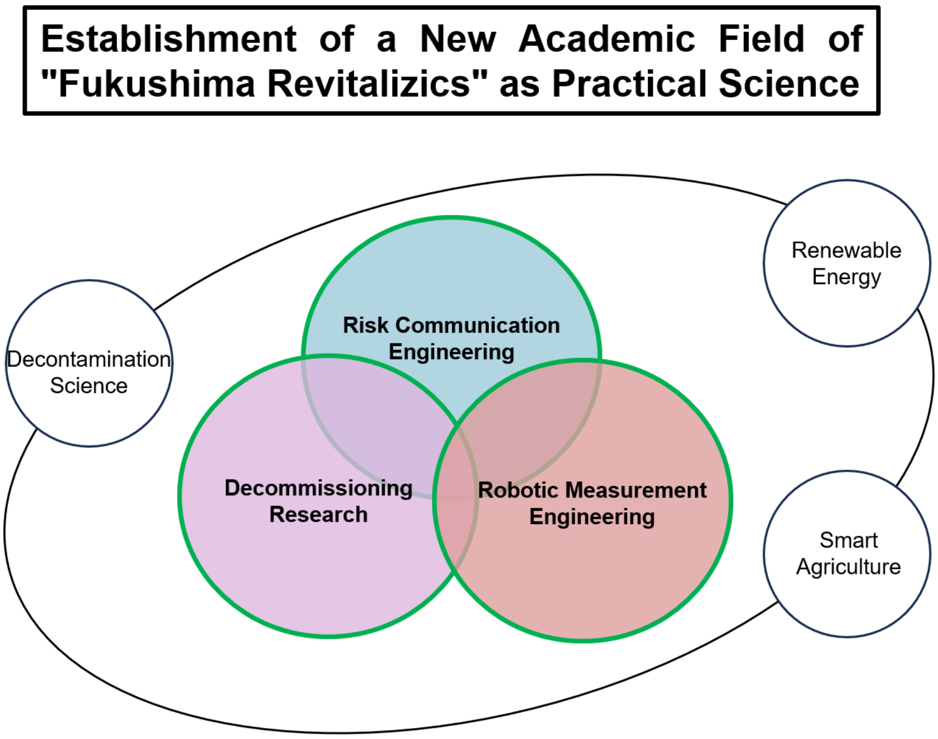

Fig.1.4 Building the New Academic Field of "Fukushima Revitalizics" as a Practical Science

Fig.1.5 Solar panel in Fukushima

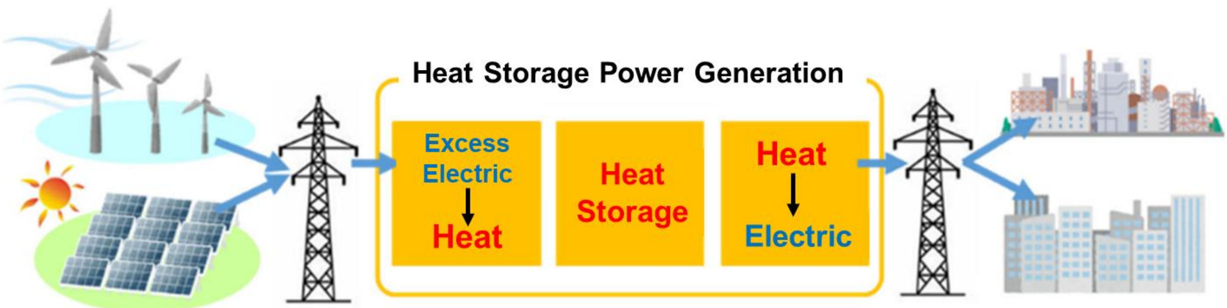

Fig.1.6 Heat storage system plays an important role in renewable energy

Fig.1.7 Fukushima robot test field

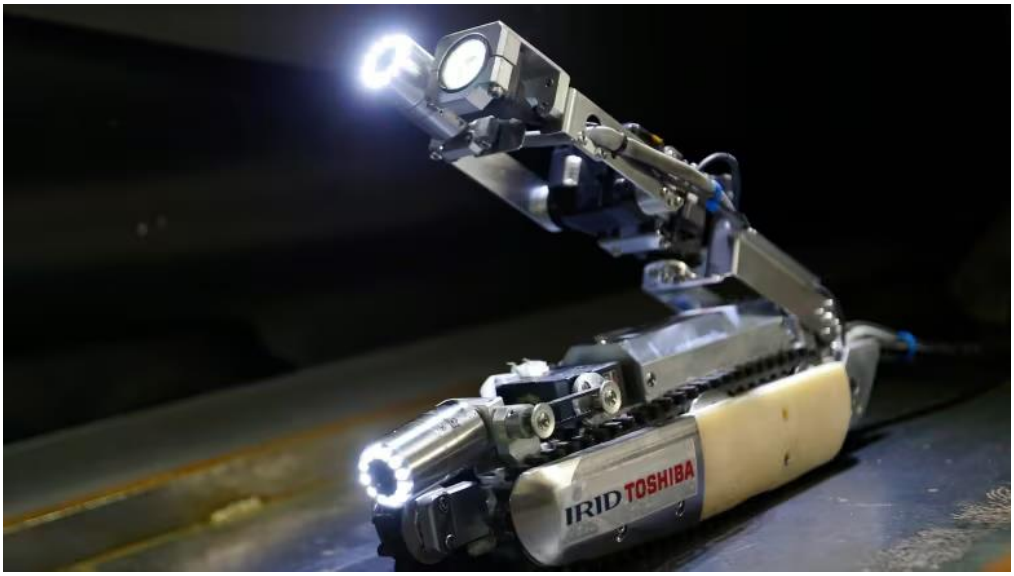

Fig. 1.8 Decommissioning robot of Toshiba

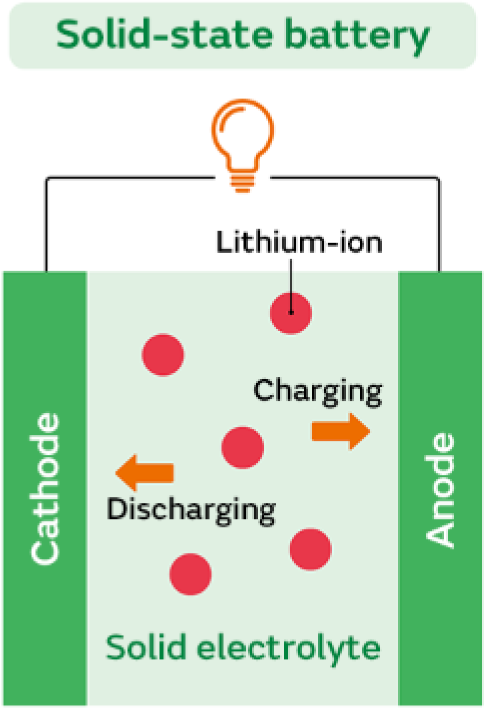

Fig.1.9 How all-solid-state batteries works

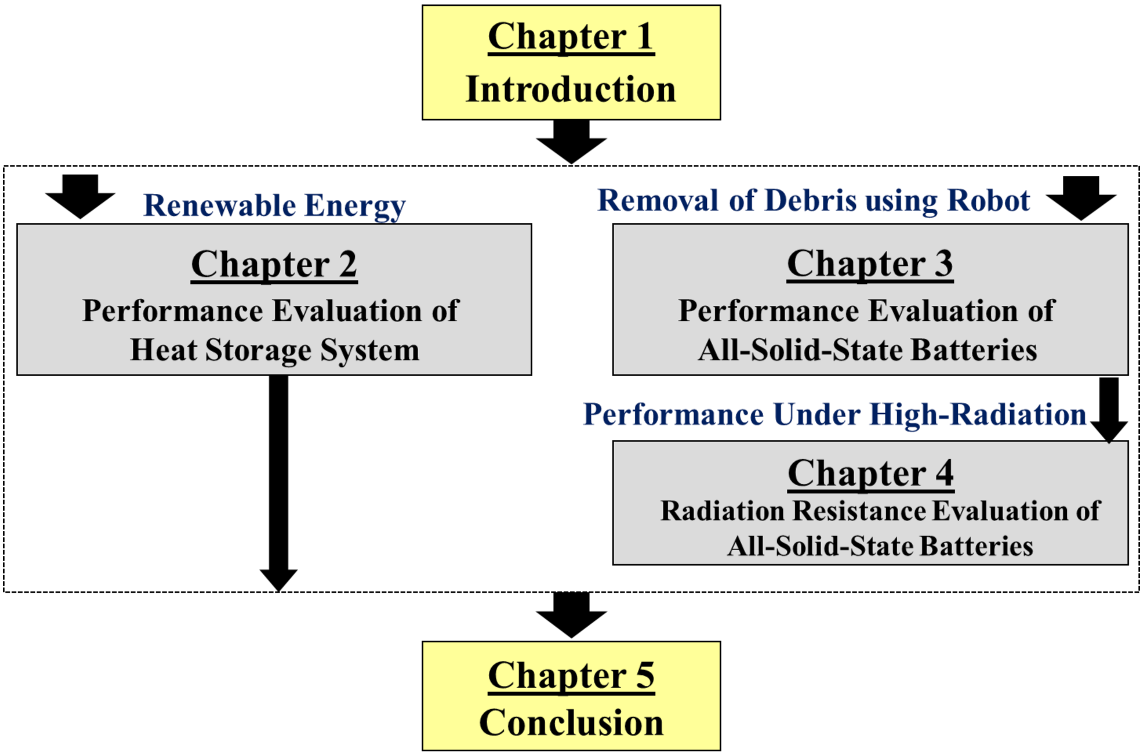

Fig. 1.10 Structure flow of this research

Chapter 2

Chapter2. Performance Evaluation of Heat Storage System using the Local Thermal Non-Equilibrium Model

2.1 Research Background

2.1.1 Importance of Heat Storage System

On a global scale, solar power and wind power are two of the most promising renewable energy sources [2-1]. They play a crucial role in reducing carbon emissions and addressing climate change. As technology advances and societal awareness of environmental protection increases, the proportion of solar and wind energy in the energy structure is gradually rising. However, the intermittent and unstable characteristics of these two energy sources can lead to interruptions in power supply during periods of insufficient sunlight (such as at night) or low wind conditions. This challenge has prompted researchers and engineers to seek effective solutions to ensure the continuous and stable supply of renewable energy [2-2].

Heat storage systems have emerged as a key technology to address this issue. The basic principle of heat storage systems is to convert excess electrical energy generated during peak solar and wind power production into heat energy [2-3]. When electricity demand increases or renewable energy supply is insufficient, the stored heat energy can be converted back into electricity through thermoelectric conversion processes, providing a continuous and stable power supply [2-4]. This approach not only improves energy utilization efficiency but also ensures energy supply reliability during periods of deficit.

Moreover, heat storage systems have additional benefits, including simple structure, low maintenance costs, and environmental friendliness. By converting electrical energy into thermal energy for storage, heat storage systems not only reduce dependency on fossil fuels but also enhance the utilization rate of renewable energy, thereby lowering the overall carbon footprint of the energy system [2-5].

There are several types of heat storage systems, such as molten salt energy storage, water energy storage, paraffin energy storage and PCM energy storage which are mentioned in Chapter 1. Considering with the disadvantage of these systems, Zanganeh, et al [2-6~2-10]. utilized the combination of air as heat transfer fluid and stone as the storage material in a tank. Field for heat storage system is shown in **Figure 2.1** and heat storage tank is shown in **Figure 2.2**. This combination offers a heat storage system with a good price- performance ratio. Air offers several advantages, such as no cost, wide range of the operating temperature, non-corrosive, non-toxic, and possibility of direct heat transfer with the storage material. On the other hand, stones are low cost and available anywhere. The use of stones has several advantages, such as: abundant and economical storing material, applicability in a wide temperature range, and enables the possibility of a direct heat transfer between the working fluid and the storage material. Combining these two materials as HTF and storage material offers a heat storage system with the lowest cost among the existing heat storage systems.

2.1.2 Principles of Stone Heat Storage system and Thermal Stratification

The process cycle of heat storage system is shown in **Figure 2.3**. In charging process, high temperature air is charged from the top of the tank and push the ambient temperature air out of the tank. The high temperature will heat the stone in the tank to restore the heat energy. After charging process, the tank will be kept under no flow and the energy is stored in the tank. When the energy charged in the tank need to be used, ambient temperature air will be charged into the tank in the opposite direction for charging process, and the high temperature air will be pushed out from the tank to use the heat energy stored in the tank. Charging process, storing process and discharging process are the full cycle of a stone heat storage tank.

In order to evaluate a performance of a stone heat storage tank, parameter which is called "Thermal stratification" is the most important. Thermal stratification is important to assure a constant extraction temperature during discharging. As shown in **Figure 2.4**, two cases of thermal stratification are shown as (a) high thermal stratification and (b)moderate thermal stratification. The difference between these two cases is the output temperature. Storage system with a high degree of thermal stratification (a), can obtain constant output air temperature better than a moderate one (b). In this research, thermal stratification is focused for evaluating the performance of stone heat storage tank and both numerical simulation and experimental validation methods were used.

2.2 Research Objectives

This research aims to demonstrate the importance and applicability of heat storage systems as an effective means to utilize energy generated from wind and solar power during nighttime or periods of low wind. By applying the Local Thermal Non-equilibrium (LTNE) model for heat transfer simulations, this study evaluates the heat storage efficiency of a stone heat storage tank. The LTNE model used in this research accounts for temperature differences between the solid and fluid/gas parts within porous materials, allowing for the calculation of temperature changes in both phases. Based on the heat transfer simulation results, a test heat storage tank was designed and fabricated to analyze the heat exchange between the fluid and solid phases in detail, thereby verifying the accuracy of the simulation methodology. Although further analysis is required to relate these simulation results to economic viability, the study provides valuable simulation outcomes for developing an economic renewable energy utilization system that balances variable renewable energy by converting part of it into heat for stone heat storage during the day or windy periods, and using the stored heat for power generation during the night or low wind periods.

2.3 Numerical Simulation Methods

2.3.1 Introduction to CFD Software

In this section, the numerical settings used in the present study is presented. CFD simulations were performed by using a commercial CFD software ANSYS Fluent version 16.0. Air was used as the heat transfer fluid and lime stone was selected as the storage material. For the CFD simulation, several assumptions are used for the model, such as: axisymmetric computational domain, incompressible fluid flow, the fluid properties are assigned as piecewise linear interpolations of tabulated data from literature, while constant properties are used for the wall, and radiation is neglected.

2.3.2 Local Thermal Non-Equilibrium (LTNE) model

The Local Thermal Non-Equilibrium (LTNE) model is a sophisticated approach used to analyze heat transfer in porous media, where the solid and fluid phases can have different temperatures. Unlike the Local Thermal Equilibrium (LTE) model, which assumes that the solid and fluid phases are at the same temperature, the LTNE model accounts for the temperature difference between these phases. This distinction is crucial in accurately modeling heat transfer processes in systems where the thermal conductivity and heat capacity of the solid and fluid phases differ significantly. The equations used for fluid and solid and heat transfer coefficient are shown below, the parameters and values are shown in **Table2.1**.

The equation for fluid phase:

$$\varepsilon(\rho c_v)_f \frac{\partial T_f}{\partial t} + (\rho c_p)_f \boldsymbol{u} \cdot \nabla T_f = \nabla \cdot (k_f \nabla T_f) + h\alpha(T_s - T_f) \quad 2.1$$

The equation for solid phase:

$$(1-\varepsilon)(\rho c)_s \frac{\partial T_s}{\partial t} = \nabla \cdot (k_s \nabla T_s) - h\alpha(T_s - T_f) \quad 2.2$$

For equation of fluid phase, it describes the temperature changes in the air within the porous medium, including both convective and conductive heat transfer, as well as heat exchange with the solid phase. $\varepsilon(\rho c_v)_f \frac{\partial T_f}{\partial t}$ represents the rate of change of internal energy in the gas phase per unit volume, where ε is porosity, $(\rho c_v)_f$ is volumetric heat capacity of air, $\frac{\partial T_f}{\partial t}$ is the rate of change of air temperature with respect to time. $(\rho c_p)_f \boldsymbol{u} \cdot \nabla T_f$ represents convective heat transfer in fluid phase, where $(\rho c_p)_f$ is mass heat capacity of air, $\boldsymbol{u}$ is velocity vector of air, ∇T_f is temperature gradient of air. $\nabla \cdot (k_f \nabla T_f)$ represents conductive heat transfer in fluid phase, $h\alpha(T_s - T_f)$ represents heat exchange between the fluid and solid phases.

For equation of solid phase, it describes the temperature changes in the solid within the porous medium, including conductive heat transfer and heat exchange with the fluid phase. $(1-\varepsilon)(\rho c)_s \frac{\partial T_s}{\partial t}$ represents the rate of change of internal energy in solid phase per unit volume, where $(1-\varepsilon)$ is volume fraction of the solid in the medium, $(\rho c)_s$ is volumetric heat capacity of the solid, $\frac{\partial T_s}{\partial t}$ is the rate of change of solid temperature with respect to time. $\nabla \cdot (k_s \nabla T_s)$ represents conductive heat transfer in the solid phase, $-h\alpha(T_s - T_f)$ represents heat exchange between the solid and air phases.

Heat transfer coefficient between air and stone computed using Wakao and Kaguei correlation

$$\mathrm{Nu} = 2 + 1.1\mathrm{Re}^{0.6}\mathrm{Pr}^{1/3} \quad 2.3$$

$$h = \frac{N_u \cdot k}{d_p}$$

2.3.3 Model Construction and Parameter Setting

Geometry used for the numerical simulation and experimental validation was based on the geometry of the pilot-scale experimental heat storage (**Figure2.5**). The heat storage tank is cylindrical shape and was made from stainless steel, with a diameter of 260mm and a height of 850mm. The computational domain in **Figure 2.5** was divided into three regions. Region number1 and 3 are the upper and lower air zone respectively, that only consist of air. Region number 2 is the porous zone of the crushed limestone, with the height of 750mm. **Table 2.2** shows the resume of tank geometry. The CFD simulation results will be focus only on the porous zone.

The initial and boundary conditions are defined according to the charging and discharging processes. At the beginning of the charging process, the temperature along the domain was uniformly set at the minimum temperature. T_{min} is the minimum temperature inside the storage tank which is 25°C. During the charging process, the air enters the storage tank from the inlet position (x/L=0) at a constant axial velocity and temperature and continues to flow in the downward direction. **Table 2.3** shows the general setting for the heat storage initial and boundary condition.

The temperature distribution at the end of the charging process is set as the initial condition for the discharging process. The direction of the air flow is reversed. The mass flow rate of inlet air during each charging and discharging processes are assumed to be equal.

The packed bed height is presented in the dimensionless form (x/L). The temperature of the packed bed can be written in the dimensionless form, using equation:

$$\theta = \frac{T - T_{min}}{T_{max} - T_{min}} \qquad 2.4$$

2.4 Verification of Simulation with Experiment

2.4.1 Experimental Apparatus

In this experimental investigation, the limestone with the size of 12mm was used, which is shown in **Figure 2.6**. The selected limestone was then filled into the storage tank and arranged as a packed bed. **Figure 2.7** presents the photograph of the packed bed of limestone inside the storage tank.

The insertion of each K-type thermocouples was done step by step after one layer of limestone was filled in the storage tank, to avoid damaging the thermocouple sensors. The distance between each thermocouple is 100mm. The sensors were set at the center of the storage tank to monitor the temperature distribution inside the storage tank in the axial direction. The end connection of each thermocouple was extended and connected to the temperature data logger. The storage tank was insulated using Rockwool material to hold its position during the experimental investigation.

After the installation of the storage tank, the other equipment was installed according to the piping and instrumentation diagram. **Figure 2.8** shows the photograph of a full heat storage system at the end of the experimental apparatus installation. The outlet air of the heat storage system was cooled using a self-designed tube heat exchanger, where the air and the coolant were flowing in the opposite direction before the vented out from the system.

Two processes will be performed during the experimental investigation, such as the charging and discharging process. The temperature and flow rate of ambient temperature air supplied from a compressor were set using a pressure regulator and a purge meter type of flow rate controller. A check value was placed before the heater to assure a one-way operation during the heat storage charging process. During the charging process, the air was heated using Sakaguchi Dennetsu Micro Cable Air Heater MCA-1500N which can heat the air until 500ºC. A total of 9 K-type thermocouples were placed along the storage tank to monitor the temperature distribution inside the tank.

2.4.2 Experimental Procedure

Two processes will be performed during the experimental investigation, such as the charging and discharging process. The flow direction during the charging process is shown in **Figure 2.9**, with the procedure as follow:

1) Setting the pressure regulator (component 2) to get air pressure of 0.05Mpa gauge
2) Turning on the air compressor (component1)
3) Adjusting the air flow rate by setting it from the flow rate controller (component3)
4) Opening valve-4(Valve-22 is closed)
5) Turning on the Micro Cable Air Heater (component6)
6) The heated air is directed to the heat storage from the top by opening Valve-10 (Valve-9 is closed)
7) Measurement of the temperature distribution inside the heat storage by using thermocouple TI-02 to TI-10 (connected to data logger)
8) The air leaving heat storage will be vented out from the system by opening Valve-24

The flow direction during the discharging process is similar to the charging process but in reverse direction, with the detail shown in **Figure 2.10** and the procedure as follow:

1) Setting the pressure regulator (component 2) to get air pressure of 0.05Mpa gauge
2) Turning on the air compressor (component1)
3) Adjusting the air flow rate by setting it from the flow rate controller (component3)
4) Opening valve-22(Valve-4 is closed)
5) The ambient air is directed into the heat storage from the bottom by opening Valve-23(Valve-24 is closed)
6) Measurement of the temperature distribution inside the heat storage by using thermocouple TI-02 to TI-10 (connected to data logger)
7) The air leaving heat storage will be vented out from the system by opening Valve-9 (Valve-8 is closed)

The heat storage was operated under both charging and discharging processes for a total of 16 hours. **Table 2.4** and **Table 2.5** shows the conditions of experimental investigation.

2.4.3 CFD and Experiment Results for Charging Process

Figure 2.11 shows the thermal stratification result of CFD simulation. The tank is charged with 8 hours and the thermal stratification is shown in each hour. The red indicates the high temperature and the blue indicates the low temperature. For experiment results, the temperature distribution inside the storage tank was monitored using 9 K-type thermocouples. **Figure 2.12** shows the recorded data set of the temperature inside the storage tank from each thermocouple during 8 hours of charging process. Since thermocouple TE01 and TE09 were positioned at the upper and air zone, these thermocouples were used to measure the inlet and outlet air temperature during the charging and discharging process respectively. From the Figure we can see that the temperature along the packed bed increases as the charging duration increases. During the first hour of charging process, the inlet air temperature keeps increasing until it reached 180^{o}C.

Comparison between the results from the experimental investigation and the CFD simulation were performed to check its difference between the two methods. **Figure 2.13** shows the comparison of the CFD simulation and the experimental investigation were presented in the dimensionless form of temperature distribution as a function of a dimensionless storage tank height. The comparison was continued until it reached 8 hours of the total charging. The CFD simulation results were presented by the solid line, and the recorded temperature data from the experimental investigation were presented by the dotted marks. After the end of charging process, the difference between CFD simulation and experiment validation is 2.93%.

2.4.4 CFD and Experiment Results for Discharging Process

The process was continued to be discharging process, as the initial condition of the discharging process was equal to the final condition of the heat storage at the end of the charging process. For the CFD simulation, the inlet temperature during the discharging process was assumed to be constant at 25^{o}C. **Figure 2.14** shows the thermal stratification result of CFD simulation. The tank is discharged with 8 hours and the thermal stratification is shown in each hour. The red indicates the high temperature and the blue indicates the low temperature. For experiment results, **Figure 2.15** presents the recorded data set of the temperature inside the storage tank from each thermocouple during 8 hours of the discharging process.

Figure 2.16 shows the comparison of the CFD simulation and experimental results for each 1 hour of discharging process. The comparisons between the results from the CFD simulations and the experimental investigation were presented in the dimensionless form of temperature distribution as a function of a dimensionless storage tank height. The comparison was continued until it reached 8 hours of discharging process. The CFD simulation results were presented by the solid line, and the recorded temperature data from the experimental investigation were presented by the dotted marks. After the end of discharging process, the difference between CFD simulation and experiment validation is 13.42%.

From the **Figure 2.13** and **Figure 2.16** can be seen that slight difference occurs between the results from the CFD simulation and experimental validation. Particularly on the top part of the packed bed during the charging process and the middle part during the discharging process. Several factors may cause the differences between these results. At first, the initial bed temperature was assumed to be constant in the CFD simulation while in actual experimental condition the initial bed temperature has around 1^{o}C difference. The inlet air temperature was assumed to be constant for the CFD simulation even though the recorded data from the experimental validation gave some changes during the first hour of charging process. Moreover, the size of the lime stone filled in the tank was not uniform. The variation in the limestone size is within 3mm.

2.4.5 Changing Parameters Considering the Humidity of Coast Area of Fukushima

For the Front-end of Fukushima Revitalizics, performance evaluation of heat stone energy storage gives technological solutions for revitalization of Fukushima area. Setting stone heat storage at the coast area of Fukushima should be taken into consideration. The weather of coast area of Fukushima may affect the heat storage efficiency and performance of a heat storage tank. Since the annual average humidity of Fukushima coast area is 68%, some parameters used in LTNE model should be recalculated because of the humidity changing. These parameters are: density of air, thermal conductivity of air, specific heat capacity of air, kinematic of air and Prandtl number of air. Equations and values from references for these parameters are shown below:

1. Density of moist air

$$\rho_{wet} = \rho_{dry} \cdot (1 - W) + \rho_{steam} \cdot W \qquad 2.5$$

Where density of dry air ρ_{dry} = 1.184kg/m^3, density of steam ρ_{steam}=0.804kg/m^3. W is the steam percentage in the air.

2. Thermal conductivity of moist air

$$\boldsymbol{k_{wet}} = 0.027\text{W/(m/K)} \qquad 2.6$$

3. Specific heat capacity of moist air

$$c_{p,wet} = (1 - W) \cdot c_{p,dry} + W \cdot c_{p,steam} \qquad 2.7$$

4. Kinematic viscosity of moist air

$$\boldsymbol{\mu_{wet}} = 1.85 \times 10^{-5} pa \cdot s \qquad 2.8$$

5. Prandtl number of moist air

$$P_{r,wet} = \frac{\mu_{wet} \cdot c_{p,wet}}{k_{wet}} = 0.694 \qquad 2.9$$

Parameters used in LTNE model considering humidity of air and the value of them are shown in **Table 2.6**.

2.5 Feasibility for Renewable Energy Usage with Stone Heat Storage

2.5.1 Advantages and Considerations for using Stone as a Heat Storage Material

There are several types of stone which can be used as storage material which is shown in **Table.2.7**. The reason for choosing limestone is that comparing with other types of stone, limestone has higher specific heat capacity and the lowest price as $5/ton. Considering the decomposition of limestone which will be happen when temperature is above 900°C (shown as chemical equation 2.10), other kinds of stone storage material should be used such as basalt and magnesite which is listed in **Table 2.7**.

$$CaCO_3 \rightarrow CaO + CO_2 \qquad 2.10$$

Stone heat storage is designed for collecting the excess energy from solar power and wind power, and provide energy restored to the consumption when there is not enough sunlight and wind. For restoring the excess energy, converting electrical energy into thermal energy for storage is needed and this procedure offers three main advantages:

1.Energy Storage Capacity:

Batteries are suitable for small to medium-scale energy storage (approximately 100 MW), with storage durations typically lasting several hours. This makes batteries effective for short-term energy management. However, for large-scale energy systems, the capacity and cost of batteries limit their application. Heat storage systems can store much larger amounts of energy (100-1,000 MW), significantly exceeding the storage capacity of batteries. By utilizing media such as stone, molten salts, or graphite, heat storage systems can maintain low costs and high energy conversion efficiency even at high capacities.

2.Storage Duration:

Batteries have relatively short storage durations, usually limited to several hours, which restricts their use for long-term energy supply. Heat storage systems, on the other hand, can store energy for much longer periods, ranging from several hours to several days, and under certain conditions, even weeks. This long-duration storage capability makes heat storage systems particularly advantageous in balancing energy supply and demand over extended periods, especially during times of insufficient solar and wind energy supply.

3.Low Cost

It has excellent features, such as the possibility of lower costs even compared to promising hydrogen storage of the same scale.

2.5.2 Comparison of Energy Storage Capacity and Application Scenarios of Solar Energy Utilization Paths

There are two primary approaches to the utilization of solar energy: the first approach involves converting solar energy into electricity through the utilization of photovoltaic cells. Subsequently, the surplus electricity is utilized to heat storage media, and the thermal energy that is stored is converted back into electricity when it is required. The second approach involves directly utilizing solar energy to heat storage media, and then converting the thermal energy into electricity through thermal conversion devices when it is required. By contrasting the specific energy storage capacities and application scenarios of these two routes, we are able to gain a better understanding of the advantages that each of these paths offers and the conditions under which they are applicable.

Photovoltaic Power Generation with Surplus Heat Storage

In the first route, solar energy is converted into electricity through the use of photovoltaic cells. The surplus electricity is then used to heat storage media, and the thermal energy that has been stored is converted back into electricity when it is required. One of the benefits of this approach is that it makes effective use of the photovoltaic technology that is already in existence. In general, photovoltaic cells have an energy conversion efficiency that is relatively high, typically falling somewhere between 15 and 20 percent. Additionally, the technology is mature and relatively inexpensive.

It is possible for photovoltaic systems to make full use of solar energy for the generation of power during the day, and then use the thermal energy that has been stored for power generation during the night or when the weather is cloudy. This results in an improvement in the efficiency with which energy is utilized. In addition, photovoltaic systems are extremely versatile, making them appropriate for energy storage as well as distributed energy systems on a scale ranging from small to medium.

Direct Solar Thermal Power Generation

The second route makes direct use of solar energy to heat the storage medium, and when it is necessary, it converts the thermal energy into electricity by utilizing thermal conversion devices (such as steam turbines). One of the characteristics and difficulties of this method is that it has technical requirements that involve high temperatures. Direct solar thermal power generation (also known as CSP) is a system that is both complicated and expensive because it requires materials that are resistant to high temperatures and optical equipment that is precise.

Despite the fact that direct solar thermal power generation has the potential to be used for large-scale energy storage, the photovoltaic power generation with surplus heat storage path is currently more practical and cost-effective. This is because of the high technical requirements and high costs associated with this method. This technique not only takes advantage of the benefits offered by photovoltaic technology, but it also addresses the intermittent nature of energy supply by utilizing heat storage, which ultimately results in the utilization of energy that is both efficient and reliable.

2.6 Conclusion

In this study, analysis of the thermocline heat storage operating parameters, using stone as the storage material, during both charging and discharging cycle, was investigated. Studies on the performance of the heat storage unit was investigated using CFD simulations. The simulation results were furthermore validated by the results from experimental investigation.

The result obtained from CFD simulations and experimental investigation were in good agreement. After the end of charging process, the difference between CFD simulation and experiment validation is 2.93%. After the end of discharging process, the difference between CFD simulation and experiment validation is 13.42%.

Only slight differences can be seen because of the fluctuation in the inlet air temperature and the non-uniformity of the limestone size that was used for the experimental validation.

For considering the humidity of Fukushima coast area, parameters such as density of air, thermal conductivity of air, specific heat capacity of air, kinematic of air and Prandtl number of airs should be recalculated. In high humidity conditions, the air contains a significant amount of water vapor. When this water vapor comes into contact with the stones, it may be absorbed by the stones or condense on their surfaces. This hygroscopic effect can cause changes in the surface temperature of the stones, thereby affecting the heat transfer efficiency. The absorption process consumes a portion of the heat energy, thereby reducing the overall heat storage efficiency. In high-temperature conditions, the moisture within the stones will evaporate, carrying away heat. This evaporative cooling effect can significantly impact the efficiency of the thermal storage system. Evaporative cooling lowers the temperature of the stones, reducing their heat storage capacity and thereby decreasing the system's heat storage efficiency in high humidity environments.

References

[2-1] A.Demirbas, Global Renewable Energy Projections, (2009) Energy sources, Vol.4, pp.212-224.

[2-2] Joseph Oyekale, Mario Petrollese, Vittoria Tola, Giorgio Cau, Impacts of Renewable Energy Resources on Effectiveness of Grid-Integrated Systems: Succinct Review of Current Challenges and Potential Solution Strategies, (2020) Energies, Vol. 13, 4856.

[2-3] Toru Okazaki, Yasuyuki Shirai, Taketsune Nakamura, Concept study of wind power utilizing direct thermal energy conversion and thermal energy storage, (2015) Reneable Energy, Vol.83, pp.332-338.

[2-4] Wolf-Dieter, Steinmann, Dan Bauer, Henning Jockenhofer, Maike Johnson, Pumped thermal energy storage (PTES) as smart sector-coupling technology for heat and electricity, (2019) Energy, Vol.183, pp.185-190.

[2-5] André Sternberg and André Bardow, Power-to-What? – Environmental assessment of energy storage systems, (2014) Energy environment science, Vol.8, pp.389-400

[2-6] Zanganeh, G., A. Pedretti, S. Zavattoni, M. Barbato, and A. Steinfeld. "Packed-bed thermal storage for concentrated solar power - Pilot-scale demonstration and industrial-scale design." (2012) Solar Energy 86: pp. 3084-3098.

[2-7] Zavattoni, S.A., M.C. Barbato, A. Pedretti, and G. Zanganeh. "CFD simulations of a pebble-bed Thermal Energy Storage system accounting for porosity variations effects." SolarPACES 2011 conference. Paper ID: 24636.

[2-8] Zavattoni S., Barbato M., Pedretti A., Zanganeh G., Steinfeld A., "Effective thermal conductivity and axial porosity distribution of a rockbed TES system: CFD modeling and experimental validation", (2012) SolarPACES Conference, September 11 -14, Marrakech, Morocco.

[2-9] Simone A.Zavattoni,Maurizio C.Barbato,Andrea Pedretti,Giw Zanganeh,Aldo Steinfield, "High Temperature Rock-bed TES System Suitable for Industrial-scale CSP Plant – CFD Analysis Under Charge/Discharge Cyclic Conditions" (2014) Energy Procedia, pp.124-133

[2-10] G.Zanganeh, A.Pedretti, A.Haselbacher ,A.Steinfeld, "Design of packed bed thermal energy storage systems for high-temperature industrial process heat" (2015) Applied energy : pp.812-822

[2-11] L. Eppelbaum, M. Modelevsky Jr., A. Pilchin, Geothermal investigations in the dead sea rift zone, israel: implications for petroleum geology, Journal of Petroleum Geology (1996), Vol.19, pp.425-444.

Table 2.1 Parameters and values for LTNE model equation

Parameter	Symbol	Value	Unit
Porosity	ϵ	0.45	$-$
Specific heat capacity of air	$(\rho c_p)_f$	1005	$J/(kg \cdot K)$
Thermal conductivity of air	k_f	0.026	$W/(m \cdot K)$
Density of air	ρ_f	1.225	kg/m^3
Kinematic viscosity of air	μ	1.81×10^{-5}	$Pa \cdot s$
Prandtl number of air	P_r	0.71	$-$
Specific heat capacity of the stone	(ρc_s)	800	$J/(kg \cdot K)$
Thermal conductivity of the stone [2-11]	k_s	2.5	$W/(m \cdot K)$
Diameter of the stone	d_p	0.012	m
Velocity of the fluid	$\boldsymbol{u}$	0.015	m/s
Reynolds number	R_e	12.21	$-$
Nusselt number	N_u	5.94	$-$
Convective heat transfer coefficient	h	12.87	$W/(m^2 \cdot K)$
Heat exchange surface area density	α	275	m^2/m^3
Volumetric specific heat capacity of the fluid	$(\rho c_v)_f$	1231.125	$J/(m^3 \cdot K)$
Volumetric specific heat capacity of the solid	$(\rho c_v)_s$	2×10^6	$J/(m^3 \cdot K)$

Table 2.2 Dimensions of the storage units

Parameter	Dimension
d_{tank}	260mm
L_{tank}	850mm
L_{stone}	750mm
Wall thickness	4mm
ε	0.45
m_{stone}	58.79kg

Table 2.3 Boundary conditions for the heat storage operation

Parameter	Setting condition
Inlet boundary condition	Mass-flow rate inlet
Outlet boundary condition	Pressure outlet
Charging inlet air temperature	200°C
Discharging inlet air temperature	25 °C
Ambient air temperature	25 °C

Table 2.4 The condition setting for experimental validation (Charging)

Parameter	Experimental condition
Limestone size	12mm
Charging duration	8 hours
Discharging duration	8 hours
Initial tank temperature	25°C
Inlet air temperature	180 °C
Inlet mass flow rate	0.001kg/s

Table 2.5 The condition setting for experimental validation (Discharging)

Parameter	Experimental condition
Limestone size	12mm
Charging duration	8 hours
Discharging duration	8 hours
Initial tank temperature	25°C
Inlet air temperature	25 °C
Inlet mass flow rate	0.001kg/s

Table.2.6 Parameters and values for LTNE model equation considering humidity of Fukushima

Parameter	Symbol	Value	Unit
Porosity	ϵ	0.45	$-$
Specific heat capacity of humid air	$(\rho c_p)_f$	1013.63	$J/(kg \cdot K)$
Thermal conductivity of humid air	k_f	0.027	$W/(m \cdot K)$
Density of humid air	ρ_f	1.182	kg/m^3
Kinematic viscosity of humid air	μ	1.85×10^{-5}	$Pa \cdot s$
Prandtl number of humid air	P_r	0.694	$-$
Specific heat capacity of the stone	(ρc_s)	800	$J/(kg \cdot K)$
Thermal conductivity of the stone [2-11]	k_s	2.5	$W/(m \cdot K)$
Diameter of the stone	d_p	0.012	m
Velocity of the fluid	$\boldsymbol{u}$	0.015	m/s
Reynolds number	R_e	12.21	$-$
Nusselt number	N_u	5.94	$-$
Convective heat transfer coefficient	h	12.87	$W/(m^2 \cdot K)$
Heat exchange surface area density	α	275	m^2/m^3
Volumetric specific heat capacity of the fluid	$(\rho c_v)_f$	1231.125	$J/(m^3 \cdot K)$
Volumetric specific heat capacity of the solid	$(\rho c_v)_s$	2×10^6	$J/(m^3 \cdot K)$

Table 2.7 Types of stone for storage material

Stone Type	Thermal conductivity (W/m·K)	Specific heat capacity (J/kg·K)	Highest Temperature (°C)	Price ($)
Granite	2.0～3.5	790	400～600	$ 25/ton
Limestone [2-11]	2.5～3.2	910	800～900	$ 5/ton
Basalt	1.8～2.2	840	700～1000	$ 40/ton
Magnesite	5.0～6.0	900	>1200	$ 450/ton

Fig.2.1 Field for heat storage system

Fig. 2.2 Heat storage system tank

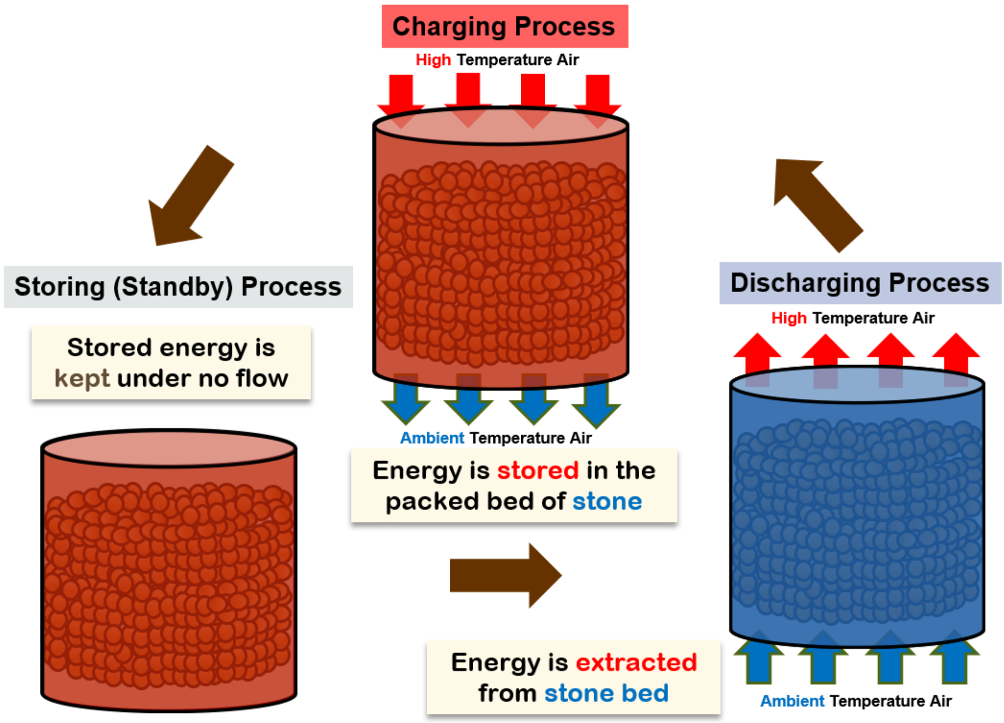

Fig.2.3 Process cycle of stone heat storage

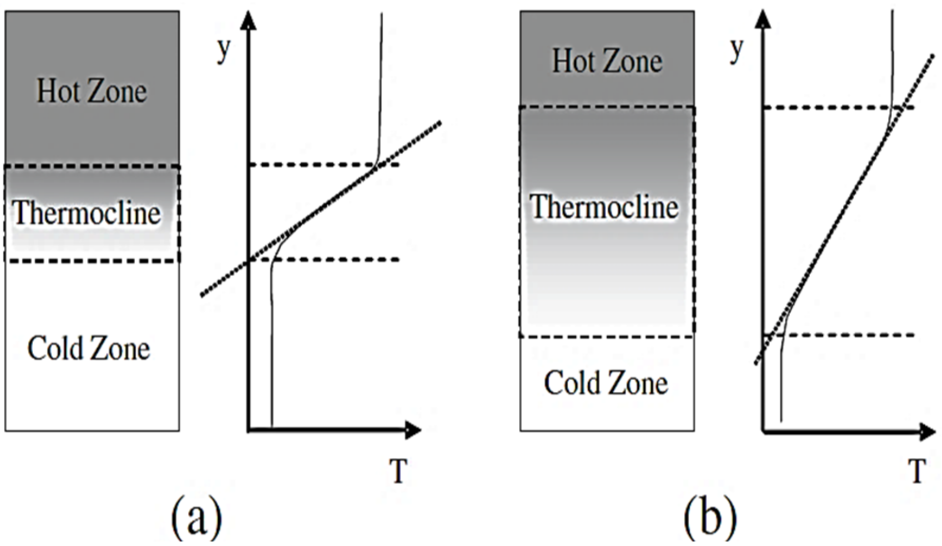

Fig.2.4 Thermal stratification of stone heat storage tank

(a) High thermal stratification case (b) Moderate stratification case

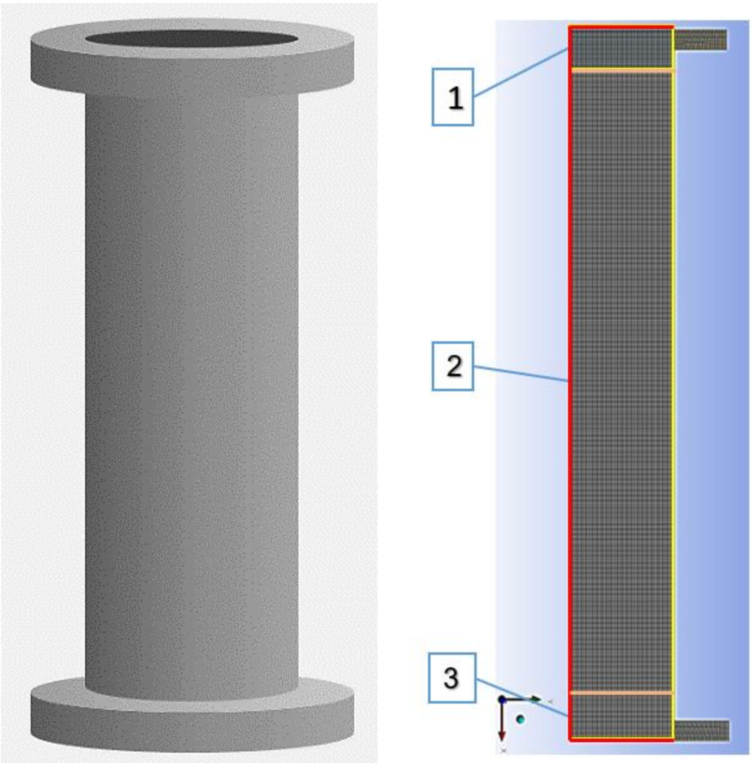

Fig.2.5 Pilot-scale experimental tank and its 2D axisymmetric geometry

Fig.2.6 The size of limestone in this experiment


Fig.2.7 Photograph of the packed bed of rocks inside the storage tank

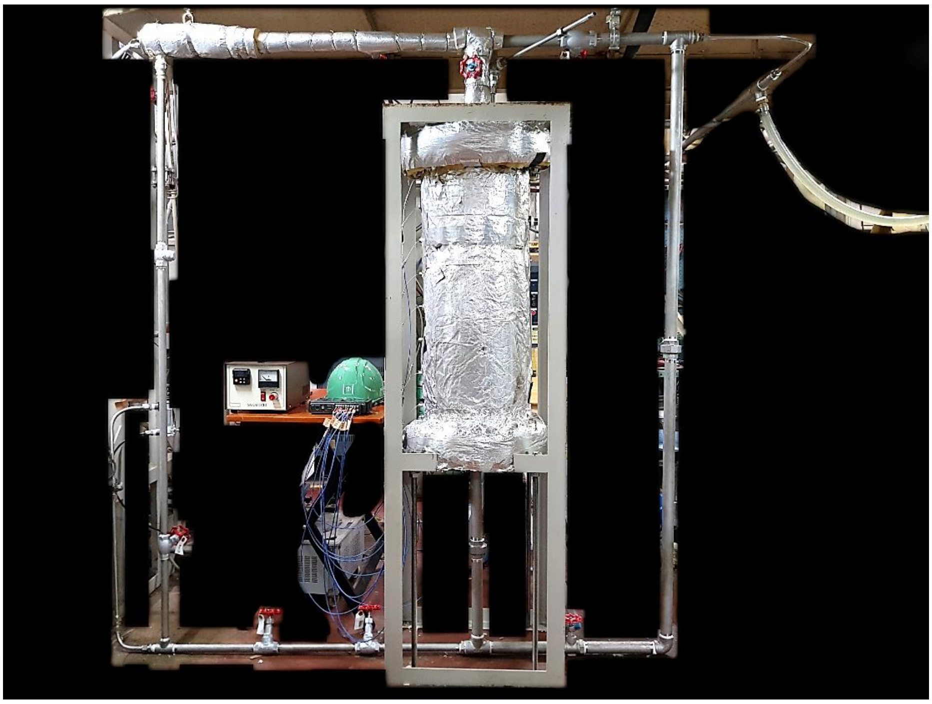

Fig.2.8 Photograph of the full heat storage system

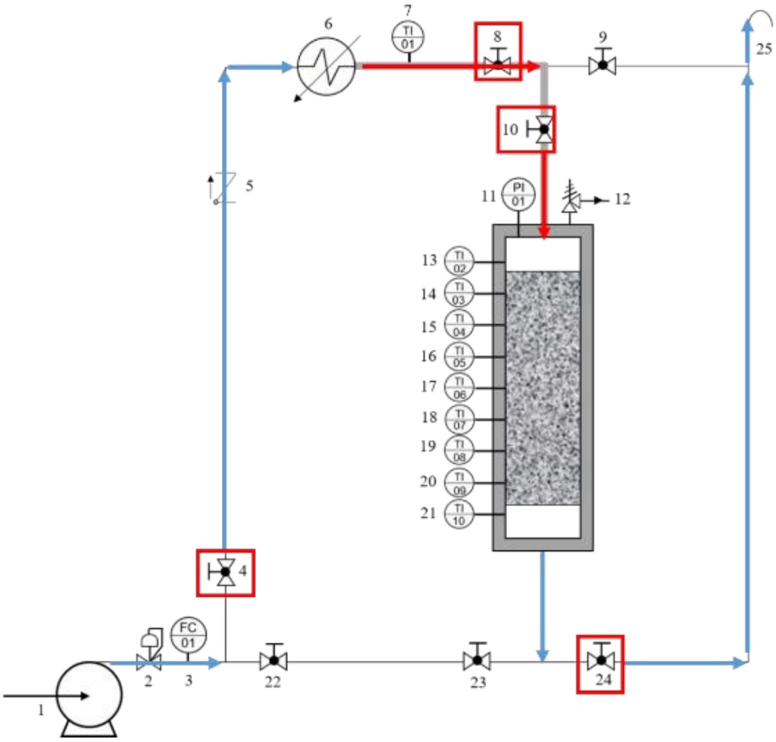

Fig.2.9 The direction of the air flow during the charging process

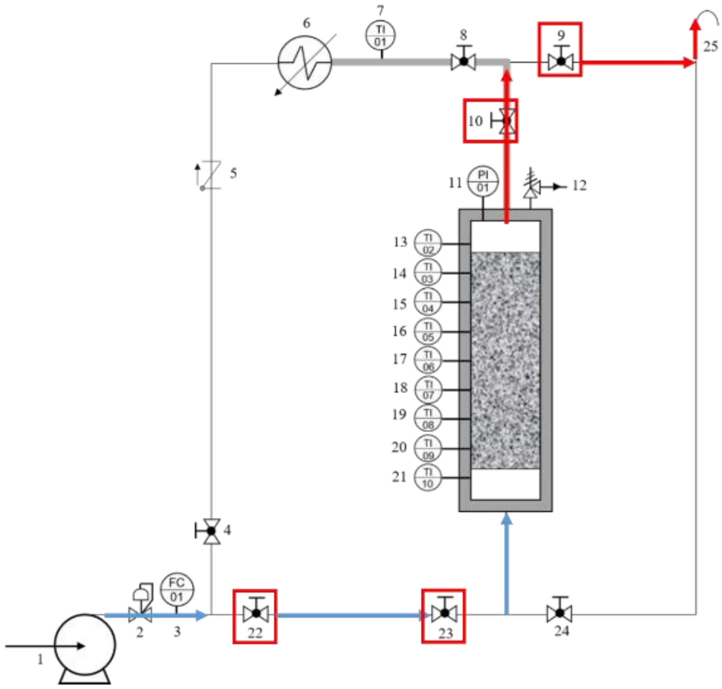

Fig.2.10 The direction of the air flow during the discharging process

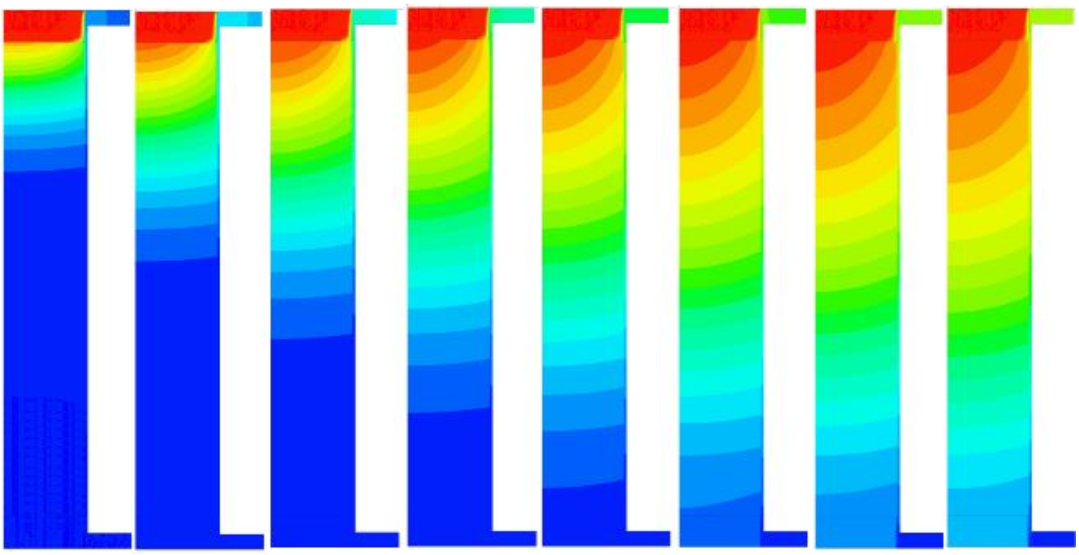

Fig.2.11 Thermal stratification for 8 hours charging

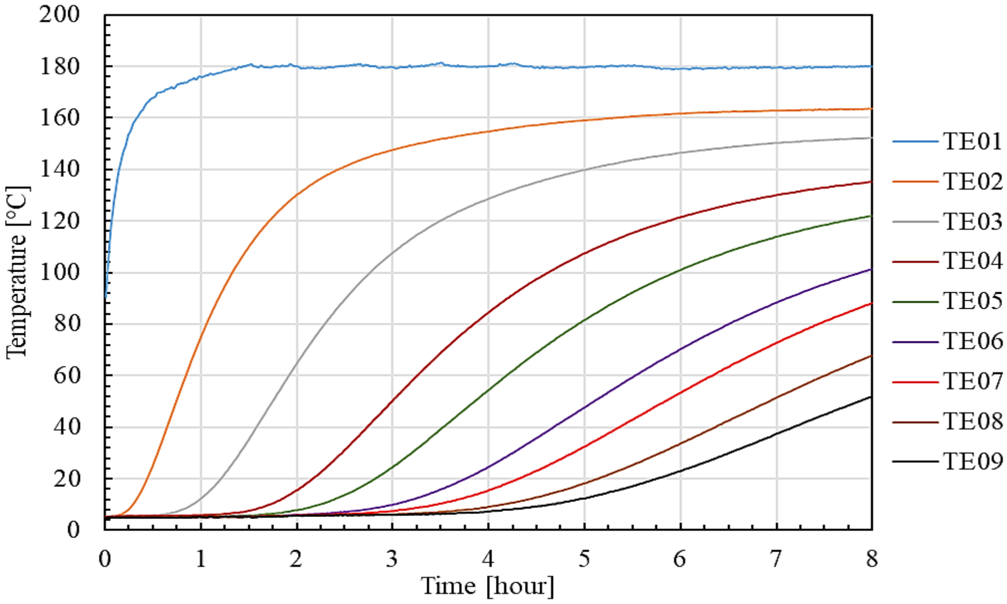

Fig.2.12 Temperature reading for each thermocouple as a function of time during the charging process

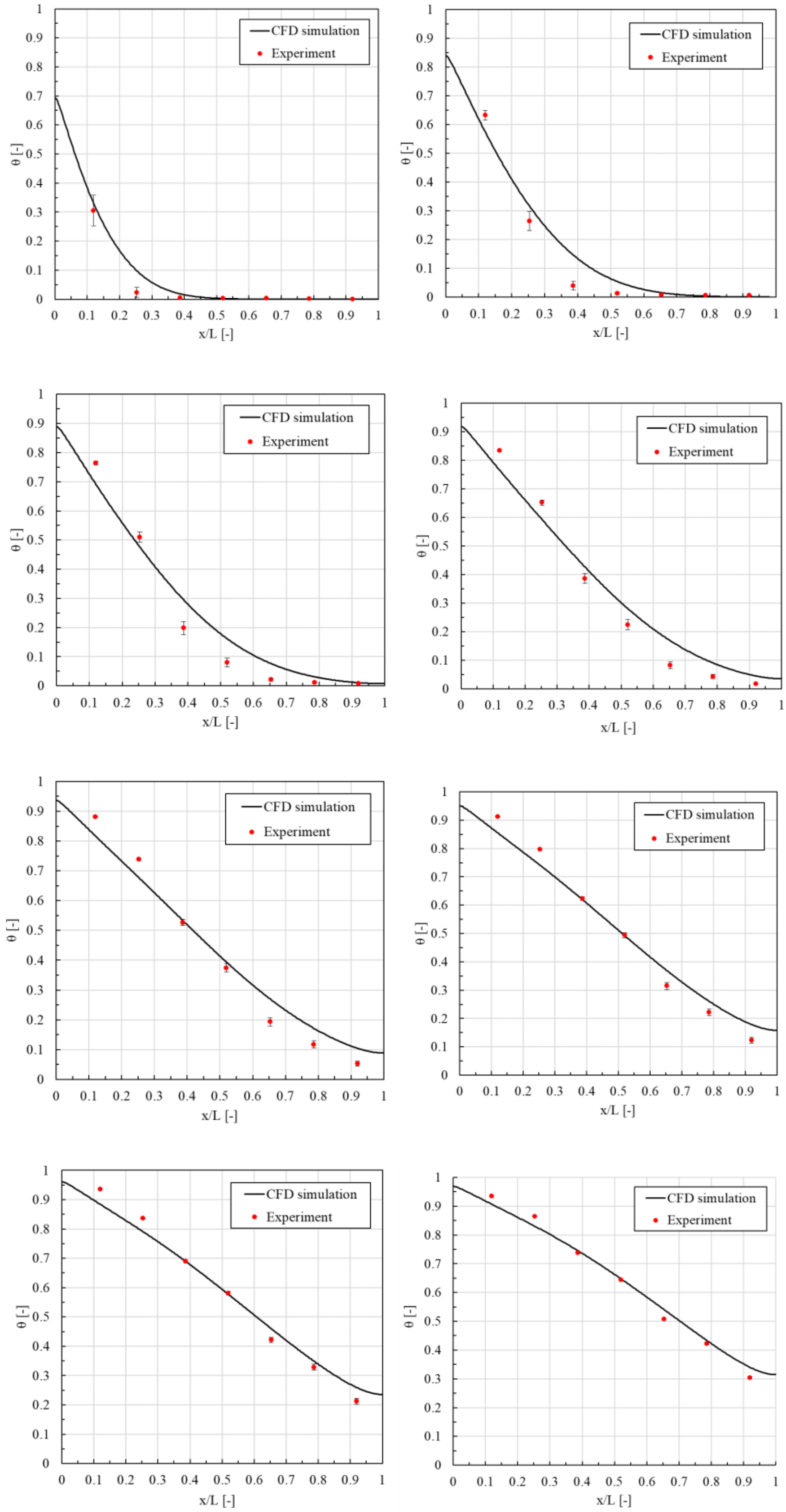

Fig.2.13 Comparison between the temperature distributions obtained from the CFD simulation and the experimental investigation during charging process

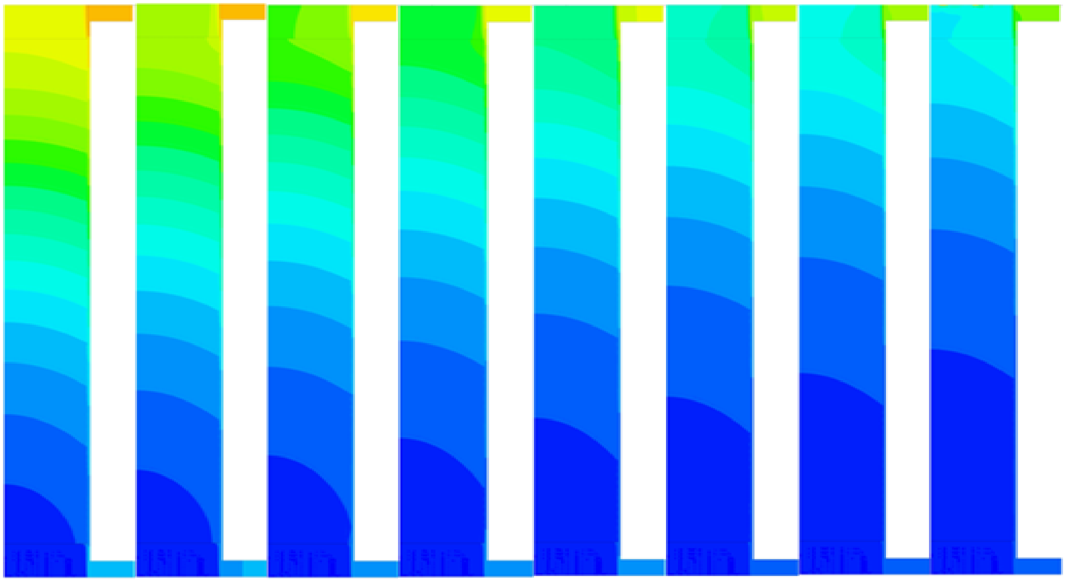

Fig.2.14 Thermal stratification for 8hours discharging

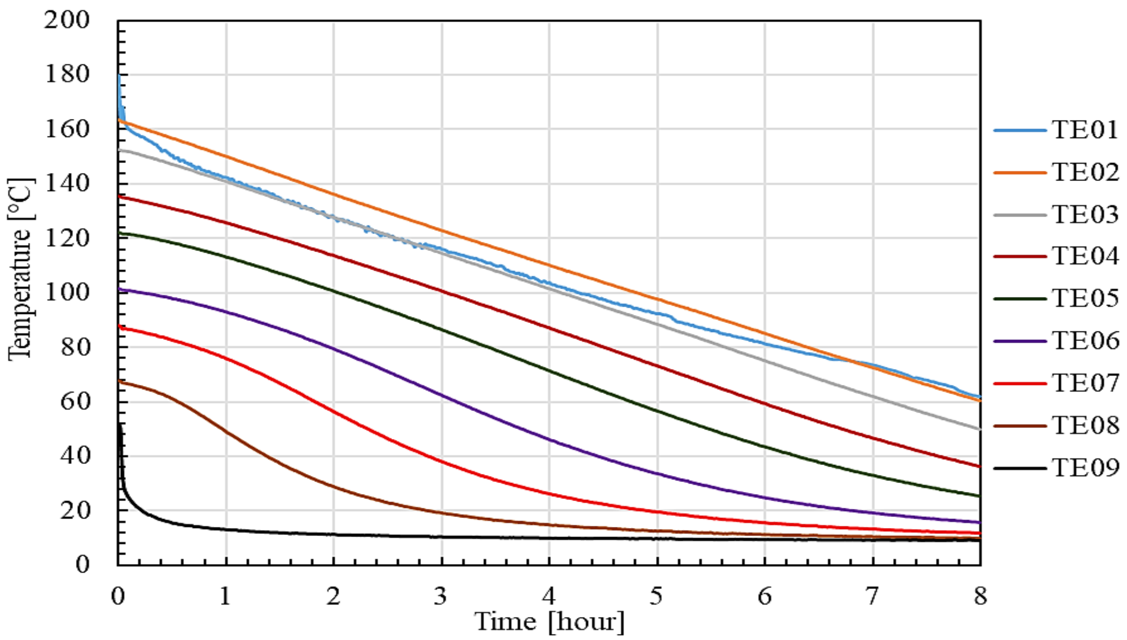

Fig.2.15 Temperature reading for each thermocouple as a function of time during the discharging process

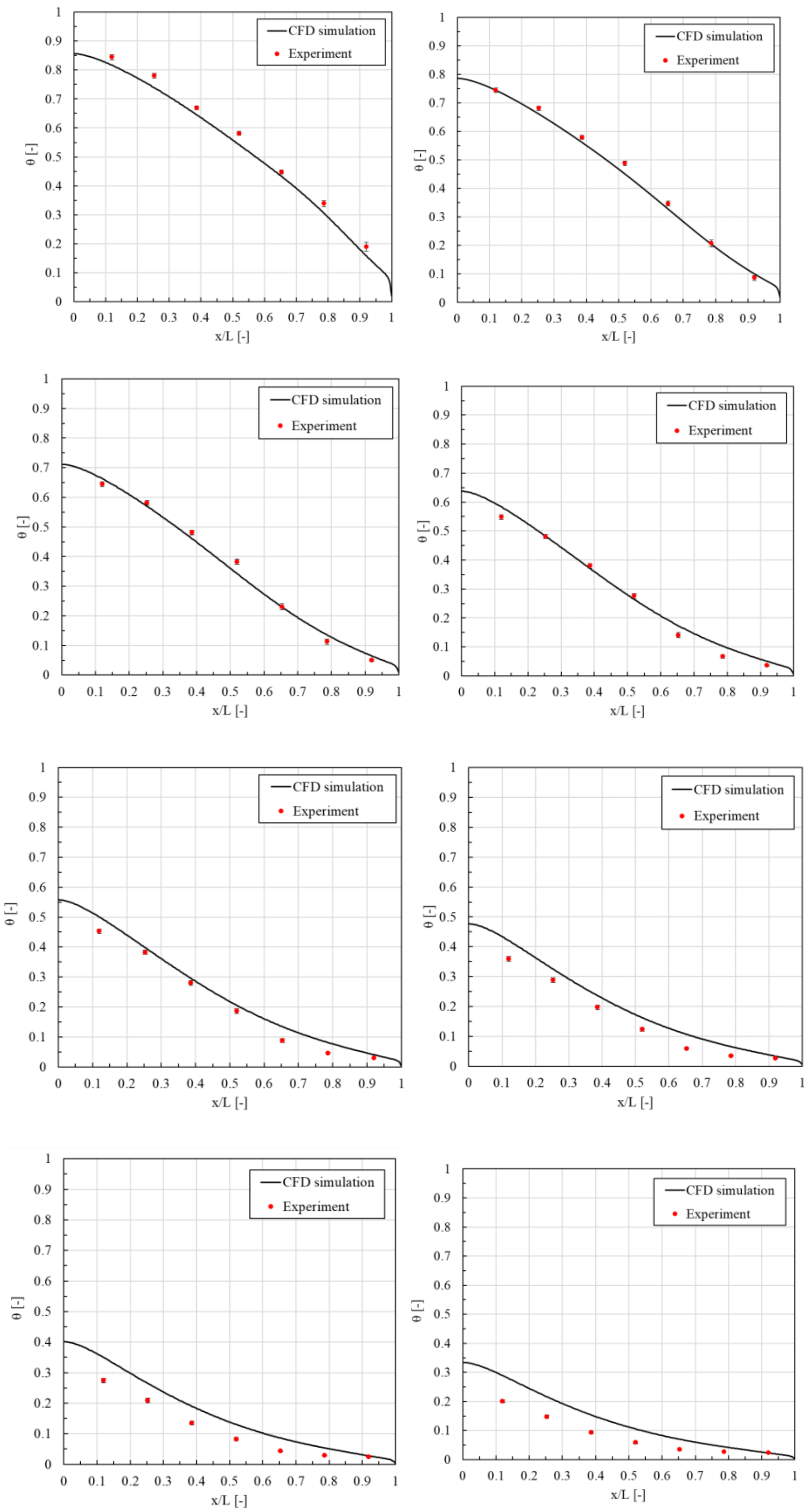

Fig.2.16 Comparison between the temperature distributions obtained from the CFD simulation and the experimental investigation during discharging process

Chapter 3

Chapter3. Performance Evaluation of All-Solid-State Batteries using Pulsed Ultrasound

3.1 Research Background

Decommissioning is an important issue for the recovery from the accident at TEPCO's Fukushima Daiichi Nuclear Power Station. The experience of decommissioning has shown that the need to mobilize robots is crucial, and the increasing use of remote-controlled robots and autonomous robots has improved the efficiency and safety of decommissioning operations [3-1]. However, the decommissioning of nuclear reactors requires more advanced technology and long-term commitments, and many technical challenges remain unresolved. Various types of autonomous robots and remote-controlled devices have been deployed so far to investigate the inside of the reactor containment vessel and to some extent to elucidate where fuel debris accumulates and how it was formed. In order to make more effective use of autonomous robots to carry out surveys and decommissioning work remotely by autonomous robots, a specially developed battery is needed with a highly sophisticated radiation resistance, a high C-rate of more than 40-200, a high depth (100%) charge and discharge, a large capacity of more than 10-200 Ah, and non-flammable. Regarding the electrical performance, All-Solid-State AMP-Battery (ASS-AMP-B) developed by AMPOWER, Co. Ltd. seems to be applicable for. This battery is quite promising as a tool that can be used in decommissioning work robots, but it is unclear why such overwhelmingly superior performance is so high compared to conventional batteries and all-solid-state ones that have been developed so far. It is also unclear about radiation resistance. Therefore, beforehand, in this paper, the radiation resistance of ASS-AMP-B was preliminarily examined using the Co^{60} radiation facility of the Tokyo Institute of Technology, and found that ASS-AMP-B maintains its electrical performance even during radiation, as described in Chapter 4.

In this Chapter 3, the electrical and structural stability of the ASS-AMP-B was investigated to confirm whether this battery can be used as a decommissioning work robot with the high electrical performance. There are several methods for evaluating electrode structure, including X-rays [3-2], electron microscopy [3-3], and ultrasound [3-4]. Since the mechanical properties of lithium-ion battery electrodes, such as density and Young's modulus, are related to the state of charge (SOC), ultrasonic non-destructive testing is used to characterize battery SOCs in terms of such mechanical properties.

3.2 Electrical/Structural Stability of the Battery under Radiation

3.2.1 Development of methods for assessing structural stability

The radiation resistance of specification described in Section 3.1 of the previous section is naturally required as radiation resistance when viewed in terms of electrical output, but this will be discussed in the next chapter (Chapter 4). Such electrical stability alone is not sufficient for radiation resistance, and it is important to evaluate the stability of the internal structure of the battery.

In this chapter, we describe the results of research and development of a method for evaluating changes in the internal structure of batteries using a new ultrasonic measurement method that is different from the conventional evaluation method.

3.2.2 All-Solid-State Lithium-ion Battery and Internal Structure

The rechargeable lithium-ion battery is made of one or more power-generating compartments called cells. Each cell has essentially three components, positive electrode, negative electrode and electrolyte.

A positive electrode connects to the battery's positive or + terminal. A negative electrode connects to the negative or - terminal. And a chemical called an electrolyte in between them.

The positive electrode is typically made from a chemical compound called lithium-cobalt oxide ($LiCoO2$) or lithium iron phosphate ($LiFePO4$). The negative electrode is generally made from carbon (graphite). The electrolyte varies from one type of battery to another.

The electrolyte carries positively charged lithium ions from the anode to the cathode (**Figure.3.1**). The movement of the lithium ions creates free electrons in the anode which creates a charge at the positive current collector. The electrical current then flows from the current collector through a device being powered (cell phone, computer, etc.) to the negative current collector. The separator blocks the flow of electrons inside the battery.

While the battery is discharging and providing an electric current (**Figure 3.2**), the anode releases lithium ions to the cathode, generating a flow of electrons from one side to the other. When plugging in the device, the opposite reaction happens, the cathode releases lithium ions and anode receives them.

Lithium-ion batteries are widely used in various applications, including electric vehicles, portable electronic devices, and stationary energy storage systems. However, due to the use of flammable liquid electrolytes, they pose significant safety risks, such as leakage, combustion, and even explosion, which can lead to serious safety concerns. Particularly in high-energy-density applications, the volatility and flammability of liquid electrolytes threaten the safety of batteries in high-temperature environments. All-solid-state batteries (ASSBs) offer safe and stable operation by eliminating the risks of leakage and combustion associated with liquid electrolytes. The high mechanical strength and ionic conductivity of solid electrolytes also provide the potential for higher energy density. Despite offering high bulk lithium-ion conductivity, ASSBs face low rate and cycle performance due to high internal resistance to lithium-ion transfer at the solid–solid electrode–electrolyte interface.

Although experimentally challenging to confirm, the origin of interface resistance depends on the combination of electrodes and electrolytes and their preparation routes [3-5]. Among the technical challenges faced by ASSBs, the most significant is the issue of volume changes in electrodes during charge and discharge cycles. As lithium ions are inserted and extracted throughout the charge and discharge operations of ASSBs, electrode materials expand and contract [3-6]. This volume change reduces the adhesion between the electrodes and the solid electrolyte, increasing internal resistance. Consequently, lithium-ion movement decreases, shortening battery life and efficiency. The reduction in adhesion at the electrode-electrolyte interface can severely impact long-term stability and performance in terms of cycle life.

To address this issue, extensive research and development have been conducted [3-7~3-17]. For instance, improvements in the properties of solid electrolytes and the development of new manufacturing techniques have progressed. Research is being conducted on better electrode materials, such as composite materials that provide flexibility and materials that suppress expansion and contraction. Similarly, efforts are being made to improve mechanical strength and ionic conductivity in the manufacture of solid electrolytes. However, these technologies alone are insufficient to completely solve the problem, and the performance of ASSBs gradually declines with repeated charge and discharge cycles.

3.2.3 Evaluation of Lithium-ion Battery Structure and Durability by Ultrasonic Measurement Method

Therefore, it is necessary to quantitatively and easily measure the structural changes related to battery performance degradation due to repeated charge and discharge [3-18]. Developing a technology to accurately evaluate interfacial changes between electrodes and electrolytes during charge and discharge cycles is essential. Davies et al. measured the time of arrival and amplitude of ultrasonic signals throughout the charge-discharge cycles in lithium iron phosphate batteries ($LiFePO_4$) using the ultrasonic contact method, clarifying the relationship between the battery's state of charge (SOC) and state of health (SOH) [3-19]. Gold et al. proposed a method to estimate SOC using a new physical probe based on ultrasonic transmission, explaining the relationship between the first propagated longitudinal wave (fast wave) and the second propagated longitudinal wave (slow wave) and the power of lithium batteries, particularly the relationship between the delay time of the slow wave and power [3-20]. Ladpli et al. attached piezoelectric ultrasonic transducers to both ends on the same side of lithium batteries using adhesive, conducted a series of studies on SOC and SOH using the ultrasonic guided wave method, and obtained favorable results. This method involved attaching ultrasonic piezoelectric transducers to the battery surface with adhesive, acquiring time-series signals with a high signal-to-noise ratio [3-21~3-23]. Popp et al. used piezoelectric transducers placed on the surface of lithium-ion batteries to measure the time-of-flight (TOF) of ultrasonic signals. This approach was developed to monitor the SOC of the batteries in a cost-effective manner. The study validated the method under various conditions, showing an error of 1.29% in TOF measurements and 16.85% in SOC estimation under challenging scenarios. This method simplifies SOC monitoring and is suitable for integration into battery management systems (BMS), highlighting its practical applicability and cost efficiency [3-24]. Copley et al. employed a single ultrasonic sensor to predict the internal structure of lithium-ion batteries. The ultrasonic signals detected changes in the battery's internal state, correlating these changes with the SOC and SOH. By utilizing a single sensor, the approach reduces complexity and cost while providing valuable insights into the battery's internal condition without needing to disassemble it, thus enhancing battery monitoring and maintenance [3-25]. Chang et al. proposed using air-coupled ultrasound for real-time measurement of lithium-ion batteries' SOC. This method analyzes the propagation characteristics of ultrasonic waves in the battery, establishing a nearly linear relationship between the ultrasonic signal parameters (amplitude and phase velocity) and the SOC. The non-contact nature of air-coupled ultrasound offers a practical and efficient way to monitor SOC, validating its feasibility and accuracy for real-time applications [3-26].

In these measurement processes, data are extracted cycle-by-cycle and conveniently overlaid to observe the progression. However, the sensitivity to detect minute structural changes affecting the origin of interface resistance, depending on the electrode-electrolyte combination, is too low. Despite the quality of these results, this method, while capable of evaluating the internal state of the battery with high precision, has the limitation of not being able to provide continuous real-time monitoring.

The purpose of this study is to improve the durability performance of ASSBs by accurately evaluating the hysteresis associated with volume changes in electrodes using ultrasonic measurements. This study aims to introduce ultrasonic measurement technology to monitor the internal state of the battery in real-time, enhancing long-term performance and safety.

3.2.4 Pulsed Ultrasonic Propagation Time Difference Evaluation Method of All-Solid-State Battery Internal Structure

In this study, a pulsed ultrasonic propagation time difference evaluation method has been used as shown in **Figure 3.3.** Ultrasonic waves gradually decay as they travel through the medium, but if there is a boundary where the material properties (acoustic impedance) suddenly change during the process, some of them are reflected and transmitted in the opposite direction. By capturing the presence or absence and strength of these reflected sound waves (reflected waves), it is possible to detect boundaries, delamination, voids, etc. of materials in the middle of the propagation path.

The intensity (reflectance) reflected at the interface surface can be expressed by the following formula (**Figure 3.4**) using the characteristic values of the acoustic impedance of the incident material and the impedance of the transmitted material. The impedance value is determined by the density of the material and the speed of sound.

Here, the phase shift due to the characteristics of the medium is

1. If ($Z_1 > Z_2$), the phase of the reflected wave is not reversed, and the transmitted wave is symmetrical as it is.
2. If ($Z_1 < Z_2$), the phase of the reflected wave is inverted, and the phase of the reflected wave is shifted by 1/2 wavelength, where (Z_1) indicates the characteristic impedance of the incident medium, and (Z2) indicates the characteristic impedance of the reflected medium.

3.3 Performance Evaluation Experiment of All-Solid-State AMP-Battery using Pulsed Ultrasonic Propagation Time Difference Evaluation Method

3.3.1 Materials and Battery Configuration

The general configuration of ASSBs consists of a solid electrolyte, cathode material, and anode material. Solid electrolytes used in ASSBs include sulfides and oxides, which possess lithium-ion conductivity. Sulfide electrolytes exhibit high ionic conductivity, while oxide electrolytes provide excellent chemical stability and mechanical strength.

Cathode materials typically used in ASSBs are lithium nickel manganese cobalt oxides (NMC), known for their high energy density. NMC materials are widely adopted due to their superior cycle life and high capacity, which contribute to the overall performance enhancement of the battery. On the other hand, lithium metal is commonly used as the anode material. Lithium metal plays a crucial role in achieving high energy density in ASSBs, owing to its high theoretical capacity and low potential.

In this study, we conducted experiments using AMPOWER's all-solid-state batteries ASS-AMP-B. AMPOWER's ASS-AMP-B utilize high-performance solid electrolytes and electrode materials, offering excellent electrochemical properties. This allows for a detailed analysis of internal structural changes during the charge and discharge cycles of the battery.

3.3.2 Ultrasound Measurement System

The ultrasonic measurement system is illustrated in **Figure 3.5**. This measurement system includes a high-power composite ultrasonic transmitter/receiver (JPR600C), a 1 MHz frequency ultrasonic transducer, a charger (Skyrc D200neo), and a discharger (Hitec AD350). For controlling the charge and discharge processes, Skyrc's dedicated software, ChargeMasterV1.19, is utilized. To confirm the ultrasonic reflection waveform and control the composite ultrasonic transmitter/receiver, Japan Probe's dedicated software is used. The ASS-AMP-B used in this experiment is AMP7197247, with a rated capacity of 15,000mAh, operating voltage of 3.85V, and rated current of 4.4A. The battery temperature is maintained at 25°C, and the current during charging and discharging is kept constant for measurement. Specific equipment specifications are shown in **Tables 3.1-3.4**. This system enables detailed observation of internal structural changes during the charge and discharge processes of the all-solid-state battery and allows high-precision recording of reflection waveforms.

3.3.3 Experimental Procedure

In this experiment, we will measure internal changes of ASS-AMP-B during charge and discharge cycles by using a 1MHz ultrasonic transducer to record reflection waveforms. First, we connect the anode and cathode of the ASS-AMP-B to the charger Skyrc D200neo, and then connect the charger Skyrc D200neo to the discharger Hitec AD350 to control the charging and discharging processes. This setup ensures smooth charging and discharging between the charger and discharger. Next, we fully charge the ASS-AMP-B. At this stage, charging is performed using the rated current of 0.2C (4.4A). Once the charging is complete, as shown in Fig.3.7, we use a 1MHz ultrasonic transducer to measure the battery and record the reflection waveforms from the PC. This data represents the initial state.

Subsequently, we begin discharging the ASS-AMP-B. Discharge is carried out at a constant current of 0.2C (4.4A). During discharge, reflection waveform data is recorded every 1500mAh using a 1MHz ultrasonic transducer. This allows for detailed measurement of internal changes in the battery during the discharge process. Next, we recharge the ASS-AMP-B. Charging is performed similarly to discharging, at a constant current of 0.2C (4.4A). During charging, reflection waveform data is also recorded every 1500mAh using a 1MHz ultrasonic transducer (**Figure 3.6**). This helps track internal changes in the battery during the charging process.

After completing all charge and discharge cycles, we analyze how the reflection waveforms shift during charging and discharging, elucidating their dynamic changes. Additionally, we evaluate the hysteresis phenomenon caused by volume changes in the electrodes. Hysteresis reflects the history effect of the expansion and contraction of electrode materials and is highly sensitive to changes in the internal structure of the battery. Measuring these shifts and hysteresis is crucial for observing material properties and structural changes inside the battery, providing significant information regarding the battery's health and performance.

3.4 Experimental Results and Discussion

3.4.1 Analysis of Reflection Waveforms during Charging

Figure 3.7 shows the reflection waveforms during charging of the ASS-AMP-B. The battery was charged at 0(fully discharged), 1500, 3000, 4500, 6000, 7500, 9000, 10500, and 12000mA at a constant current of 0.2C. rate.
During the charge process, it was observed that the primary reflection wave of the ASS-AMP-B gradually shifted slightly in the negative direction along the horizontal axis. Using the waveform position of the fully discharged state of the ASS-AMP-B as a reference, the relationship between the charge capacity and the displacement of the primary reflection waveform of the ASS-AMP-B is shown in **Figure 3.8**. The horizontal axis of each point corresponds to the charge capacity, and the vertical axis represents the reflection waveform difference.

3.4.2 Analysis of Reflection Waveforms during Discharging

As in the charging process, the ASS-AMP-B was fully charged and then discharged. The results of recording the ultrasonic reflection waves every 1500mAh during the discharge are shown in **Figure 3.9**. The primary reflection wave from the ASS-AMP-B is located in the central part of the reflection waveform, between 10 and 15 microseconds.

During the discharge process, it was observed that the primary reflection wave of the ASS-AMP-B gradually shifted slightly in the positive direction along the horizontal axis. Using the waveform position of the fully charged state of the ASS-AMP-B as a reference, the relationship between the discharge capacity and the displacement of the primary reflection waveform of the ASS-AMP-B is shown in **Figure 3.10**. The horizontal axis of each point corresponds to the discharge capacity, and the vertical axis represents the reflection waveform difference.

3.4.3 Comparative Analysis of Reflection Waveforms

Based on the above results, the relationship between the time of the primary reflection waveform of the ASS-AMP-B and the battery capacity during the charging and discharging processes is plotted in the same graph (**Figure 3.11**) with the results of **Figure 3.8** and **Figure 3.10**. As shown in **Figure 3.11**, the red dots represent the results of the charging process, and the blue dots represent the results of the discharging process. The red line indicates the regression line for the charging results, and the blue line indicates the regression line for the discharging results.
The errors bards between red and blue curves are clearly separated in the charge/discharge capacity below 7500mAh, but almost overlapped above 7500mAh. Therefore, the data obtained above 7500mAh in the charge and discharge are combined together, and the combined data are plotted in **Figure 3.12**. As can be seen in **Figure 3.12**, we can say clearly that some hysteresis exists between charge and discharge process below 7500mAh. This hysteresis phenomenon clearly shows the relationship with the internal structure of the battery. This hysteresis seems to be caused by the structural difference of the electrode layer between charge and discharge process. This kind of hysteresis in the electrode layer structure has not been yet reported.

The hysteresis observed during the charge-discharge cycle indicates the physical delay or history-dependent behavior as the electrode materials expand and contract with the insertion and extraction of lithium ions. This allows for more precise monitoring of minor structural changes and degradation processes inside the battery. The phenomenon where the reflection waveform shifts in the negative direction along the horizontal axis during the charging process corresponds to the expansion of the electrode materials, while the shift in the positive direction during the discharging process corresponds to the contraction of the electrode materials. The trend of these shifts and their linearity strongly suggests the presence of hysteresis. Additionally, from the slope and displacement amount of the regression lines, detailed information about the characteristics and degradation progress of the electrode materials can be obtained.

3.4.4 Analysis of Hysteresis Phenomenon measured by Ultrasonic Reflection Waveforms

Other techniques for measuring volume changes have been proposed in the past, but many of these methods do not consider hysteresis. This study proposes the use of ultrasonic measurement technology as a low-cost method to measure hysteresis, leveraging the characteristics of ASSBs. Ultrasonic measurement is suitable for high-precision monitoring of internal volume changes because it can non-invasively and in real-time identify internal structural changes. Ultrasonic technology records changes in adhesion between the solid electrolyte and the electrodes in real-time, providing immediate information about the battery's health and performance. This concept, which holds groundbreaking potential for ASSB research, combines novelty and relevance.

Durability testing largely depends on the consistency of hysteresis in volume changes of the electrodes during charge and discharge. Hysteresis refers to the history effect or physical delay caused by the expansion and contraction of the electrodes. Evaluating the durability of ASSB heavily relies on accurately measuring this hysteresis. By assessing the interaction and adhesion changes between the electrode and solid electrolyte in real-time, significant insights can be provided for improvement methods, leading to a deeper understanding of the underlying processes of battery degradation.

The battery's electrodes are composed of a mixture of active material particles, conductive carbon, and binder additives adhered to a current collector. Batteries using conversion-type electrodes exhibit higher energy storage density but suffer from much more severe capacity loss compared to batteries using intercalation-type electrodes. Capacity loss is believed to be the result of poor contact between the active material and current collector or the destruction of the solid electrolyte interface (SEI) layer.

To achieve higher energy density, conversion-type materials (such as metal oxides, sulfides, and fluorides) are being intensively studied. Conversion reactions can accommodate more lithium ions than intercalation reactions, resulting in much higher capacity. However, they also face serious issues such as high hysteresis, low-rate capability, and rapid capacity loss. The inevitable volume changes during the cycling of conversion compounds (for example, 81.3% in $Fe3O4$) are believed to cause capacity loss. Volume expansion leads to pulverization of the active material, poor contact with the binder and current collector, and the destruction of the SEI layer. It has also been shown that capacity loss depends on the current density (C-rate). Previous studies have reported that capacity loss is more gradual at low current densities and can be recovered by lowering the C-rate at high C-rates. These results indicate that the mechanism of capacity loss is not fully understood. From a structural perspective, the crystal structure of conversion-type electrodes is completely decomposed and reconfigured during the initial cycles. Therefore, the structural changes of electrode materials during subsequent lithium insertion/extraction follow a different path from those of the initial reactions. This means that structural understanding inferred from initial discharge/charge cannot directly interpret the cycling performance of conversion-type materials. Different local environments of strain, defects, and other microscopic factors may lead to different electrochemical properties in long-term cycling. So far, the mechanism behind the severe capacity loss over the cycling of conversion compounds has not been clarified.

3.4.5 OCV Curve of All-Solid-State AMP-Battery (ASS-AMP-B) During Charge and Discharge Cycles.

Figure 3.13 shows the change in voltage during the charge and discharge, and change in OCV (open circuit voltage), which is given by the doted green line. The x axis is the charge/discharge capacity, y axis is the OCV. The red line values for charging are slightly higher voltage than OCV, and its difference is very little. For the blue line for discharging, they are slightly lower than OCV. The OCV curve lies between the charging and discharging curves, and the voltage difference between the charging and discharging curves is given by V=IR. Thus, it states that the changes in voltage during charging and discharging are almost equal to the changes in the OCV. When examining the results for the charging process, the SOC within the range of 0 to 1 closely resembles the structural results previously mentioned. Furthermore, the analysis indicates a significant similarity between the structural and electrical results during the charging process. However, before delving into this comparison, it is essential to discuss the discharging process. For the SOC values above 50%, there is a notable similarity with the structural results. Conversely, when the SOC drops below 50%, the OCV results do not exhibit hysteresis, whereas the structural analysis does reveal hysteresis. This indicates that while the electrical measurements do not display hysteresis, the structural measurements do.

3.4.6 Similarity between OCV charging curve and ultrasonic reflection waveform difference charging curve

As described above, if the volume change of the anode material given to the OCV during charging is the ultrasonic reflected waveform charging curve, these two curves should be found to coincide with the differential equation. Therefore, the results of the analysis and verification of the similarity of differential equations are described.

Curve A in **Figure 3.14** shows the relationship between the converted voltage measured by ultrasonic measurement and SOC (yellow dot is the measured value and the dotted line is the logarithmic approximation formula of $y=0.4611\ln(x)+4.1235$. For the conversion of the ultrasonic measurement value into the electrical voltage, the highest and lowest values for ultrasonic measurement are converted to the highest and lowest voltages in the charge/discharge curves obtained in **Figure 3.13**, assuming that the electrode structures parameter obtained by ultrasonic measurement directly show the electrical voltage. Curve B shows the relationship between electrical charging voltage and SOC (blue solid line is the measured value and the dotted line is the logarithmic approximation formula of $y=0.4699\ln(x)+4.0837$. The similarity between the both curves A and B indicates the above assumption on the direct relationship between the electrode structures parameter obtained by ultrasonic measurement and the electrical voltage in the charging process. Considering the similarity between the charging voltage and OCV, as mentioned above in **Figure 3.13**, the Nerenst equation of OCV is given by the logarithmic approximation formula of $y=0.4699\ln(x)+4.0837$. Also, it may say that the electrode structure change in charging process closely represented by the Nernst equation of the OCV.

The differential equations of the both logarithmic approximation formula is $dV/dSOC=0.4611/x$ and $=0.4699/x$, respectively. The constants of the both differential equations are very close. This suggests that the differential equations are attributed to the same phenomenon, and that the electrochemical reaction process, which is the OCV value when charging with a constant current, can be regarded as a phenomenon of the same chemical reaction process by the ultrasonic measurement method of this study. In other words, it has been clarified that the parameters that determine the OCV charging characteristics in constant current charging determined by the internal structure of the all-solid-state battery can be determined by the ultrasonic measurement method of this method.

Thus, the differential equation for the changes in the OCV during charging was found to closely match the structural changes. On the other hand, for the discharge, there exists a large difference between the OCV and the electrode structure as described in **Figure 3.12** and **Figure 3.13**. Thus, we can say that the OCV remains constant despite significant structural changes in the electrodes during charging and discharging. This indicates that the anode electrode composite material of the ASS-AMP-B possesses high elasticity. Consequently, it has been determined that the ASS-AMP-B is an ultra-high-performance all-solid-state lithium battery that can be used as a power source for decommissioning robots.

3.5 Conclusion

In this study, the internal structural changes of ASSB during the charge-discharge process were monitored in real-time using ultrasonic measurement technology. By evaluating the results, the hysteresis related to the volume changes of electrode materials was accurately measured, and its impact on the performance and lifespan of ASSB was clarified. The experimental results demonstrated that ultrasonic measurement technology could non-invasively and accurately capture internal changes, making it an effective method for real-time monitoring of adhesion variations at the electrode and solid electrolyte interface.

The differential equation for the changes in the OCV during charging was found to closely match the structural changes. It was observed that the OCV remains constant despite significant structural changes in the electrodes during charging and discharging. This indicates that the anode electrode composite material of the ASS-AMP-B possesses high elasticity. Consequently, it has been determined that the ASS-AMP-B is an ultra-high-performance and non-flammable all-solid-state lithium-ion battery that can be used as a power source for decommissioning robots.

References

[3-1] M. A. Hannan, M. M. Hoque, A. Hussain, Y. Yusof, and P. J. Ker, ‘‘State-ofthe-art and energy management system of lithium-ion batteries in electric vehicle applications: Issues and recommendations,’’ IEEE Access, vol. 6, pp. 19362–19378, 2018.

[3-2] R. Xiong, J. Cao, Q. Yu, H. He, and F. Sun, ‘‘Critical review on the battery state of charge estimation methods for electric vehicles,’’ IEEE Access, vol. 6, pp. 1832–1843, 2018.

[3-3] V. A. Sethuraman, L. J. Hardwick, V. Srinivasan, and R. Kostecki,‘‘Surface structural disordering in graphite upon lithium intercalation/deintercalation,’’ J. Power Sources, vol. 195, no. 11, pp. 3655–3660,Jun. 2010.

[3-4] D. Schneider, ‘‘Silicon anodes will give lithiumion batteries a boost,’’ IEEE Spectr., vol. 56, no. 1, pp. 48–49, Jan. 2019.

[3-5] J. H. Lee, H. M. Lee, and S. Ahn, ‘‘Battery dimensional changes occurringduring charge/discharge cycles—Thin rectangular lithium ion and polymer cells,’’ J. Power Sources, vols. 119–121, pp. 833–837, Jun. 2003.

[3-6] X. Wang, Y. Sone, and S. Kuwajima, ‘‘In situ investigation of the volume change in li-ion cell with charging and discharging satellite power applications,’’ J. Electrochem. Soc., vol. 151, no. 2, pp. A273–A280, Jan. 2004.

[3-7] J. Noël and G. Kerschen, ‘‘Nonlinear system identification in structural dynamics: 10 more years of progress,’’ Mech. Syst. Signal Process., vol. 83, pp. 2–35, Jan. 2017.

[3-8] K. R. Kganyago and P. E. Ngoepe, ‘‘Structural and electronic properties of lithium intercalated graphite LiC6,’’ Phys. Rev. B, Condens. Matter, vol. 68, Nov. 2003, Art. no. 205111.

[3-9] R. Lammering, U. Gabbert, M. Sinapius, T. Schuster, and P. E. Wierach, Lamb-Wave Based Structural Health Monitor. Polymer Composites. Luxemburg, Germany: Springer, 2018.

[3-10] Superior Lithium Polymer Battery (SLPB) Cell Specification, Kokam Company, Suwon, South Korea, 2017.

[3-11] F. Grimsmann, F. Brauchle, T. Gerbert, A. Gruhle, M. Knipper, and J. Parisi, ‘‘Hysteresis and current dependence of the thickness change of lithium-ion cells with graphite anode,’’ J. Energy Storage, vol. 12, pp. 132–137, Aug. 2017.

[3-12] M. Bauer, M. Wachtler, and H. Stöwe, J. V. Persson, and M. A. Danzer, ‘‘Understanding the dilation and dilation relaxation behavior of graphite-based lithium-ion cells,’’ J. Power Sources, vol. 317, pp. 93–102, Jun. 2016.

[3-13] M. Luthfi, ‘‘State estimation of lithium ion battery using non-invasive method,’’ M.S. thesis, Carinthia Univ. Appl. Sci., Villach, Austria, 2018.

[3-14] M. J. S. Lowe, ‘‘Matrix techniques for modeling ultrasonic waves in multilayered media,’’ IEEE Trans. Ultrason., Ferroelectr., Freq. Control, vol. 42, no. 4, pp. 525–542, Jul. 1995.

[3-15] A. Demčenko and Mažeika, ‘‘Calculation of Lamb waves dispersion curves in multilayered planar structures,’’ Ultragarsas, vol. 44, no. 3, pp. 15–17, 2002.

[3-16] A. G. Hsieh, S. Bhadra, B. J. Hertzberg, P. J. Gjeltema, A. Goy, J. W. Fleischer, and D. A. Steingart, ‘‘Electrochemical-acoustic time of flight: In operando correlation of physical dynamics with battery charge and health,’’ Energy Environ. Sci., vol. 8, pp. 1569–1577, Mar. 2015.

[3-17] UNECE - United Nations Economic Commission for Europe.2017. WLTP—Worldwide Harmonized Light-Duty Vehicles Test Procedure.

[3-18] C. Yang. (2017). Distributed Piezoelectric Transducers and Their Applications in Structural Health Monitoring.
[3-19] G. Davies, K. W. Knehr, B. Van Tassell, T. Hodson, S. Biswas, A. G. Hsieh, and D. A. Steingart, Journal of The Electrochemical Society 164(12), A2746–A2755 (2017)
[3-20] L. Gold, T. Bach, W. Virsik, A. Schmitt, J. Mueller, T. E. Staab, and G. Sextl, ''Probing lithium-ion batteries' state-of-charge using ultrasonic transmission—Concept and laboratory testing,'' J. Power Sources,vol. 343, pp. 536–544, Mar. 2017.
[3-21] P. Ladpli, F. Kopsaftopoulos, and F.-K. Chang, ''Estimating state of charge and health of lithium-ion batteries with guided waves using built-in piezoelectric sensors/actuators,'' J. Power Sources, vol. 384, pp. 342–354, Apr. 2018.
[3-22] P. Ladpli, C. Liu, F. Kopsaftopoulos, and F.-K. Chang, ''Estimating lithium-ion battery state of charge and health with ultrasonic guided waves using an efficient matching pursuit technique,'' in Proc. IEEE Transp. Electrific. Conf. Expo, Asia–Pacific (ITEC Asia–Pacific), Jun. 2018, pp. 1–5.
[3-23] P. Ladpli and F.-K. Chang, ''Battery state monitoring using ultrasonic guided waves,'' U.S. Patent WO 2017 223 219 A1,Jun. 21, 2017.
[3-24] H. Popp, G. Glanz, K. Alten, I. Gocheva, W. Berghold, and A. Bergmann, ''Mechanical frequency response analysis of lithium-ion batteries to disclose operational parameters,'' Energies, vol. 11, no. 3, p. 541, Mar. 2018.
[3-25] R.J. Copley, Prediction of the internal structure of a lithium-ion battery using a single ultrasound wave response, (2023) Journal of Energy Storage, Vol.72,108778.
[3-26] Jun jie Chang, Xuefeng Zeng, Tao Lei wan, Real-time measurement of lithium-ion batteries' state-of-charge based on air-coupled ultrasound, (2019) AIP Advanced, Vol.9, paper number 085116.

Table 3.1 Balance Charger/Discharger (Skyrc D200neo) Specifications

AC input voltage	100-240V
DC input voltage	10-30V
Charging current range:	0.1-20A
Discharging current range	0.1-2.0A

Table 3.2 Discharger (Hitec AD350) Specifications

Output voltage	5V
Input voltage	5V
Current rating	40A
Discharge power	350W
Discharge current	0.1～40A

Table 3.3. Specifications of All-Solid-State AMP-Battery

Operating voltage	3.85V
Maximum voltage	4.4V
Charging rate	0.2C
Discharging rate	0.2C
Cell capacity	15000mAh

Table 3.4. Pulser/Receiver Specifications

Pulse voltage	10～600V
Transmission frequency	30kHz ～10MHz
Receiver frequency band	300Hz～10MHz

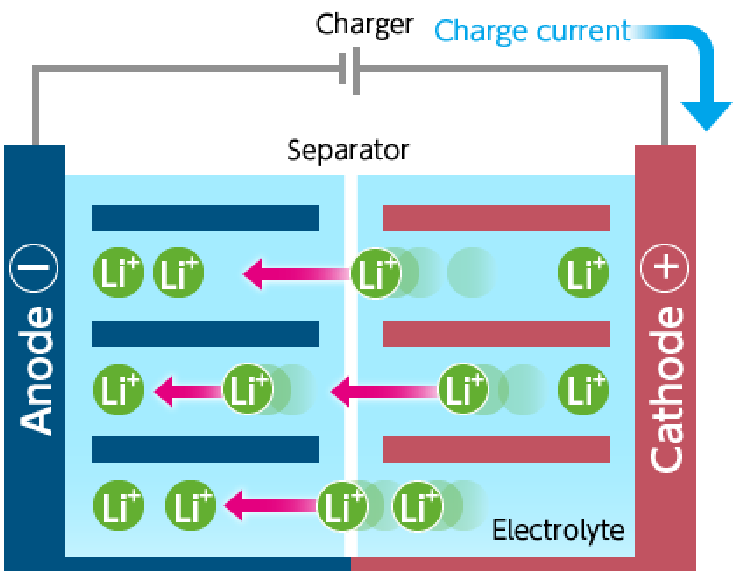

Fig.3.1 Movement of ions and electrons in charging

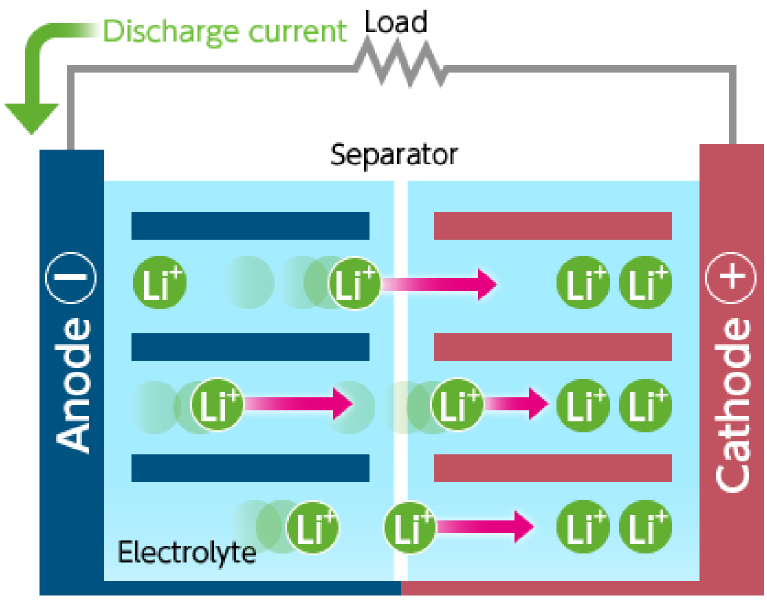

Fig.3.2 Movement of electrons and ions in electrical discharges

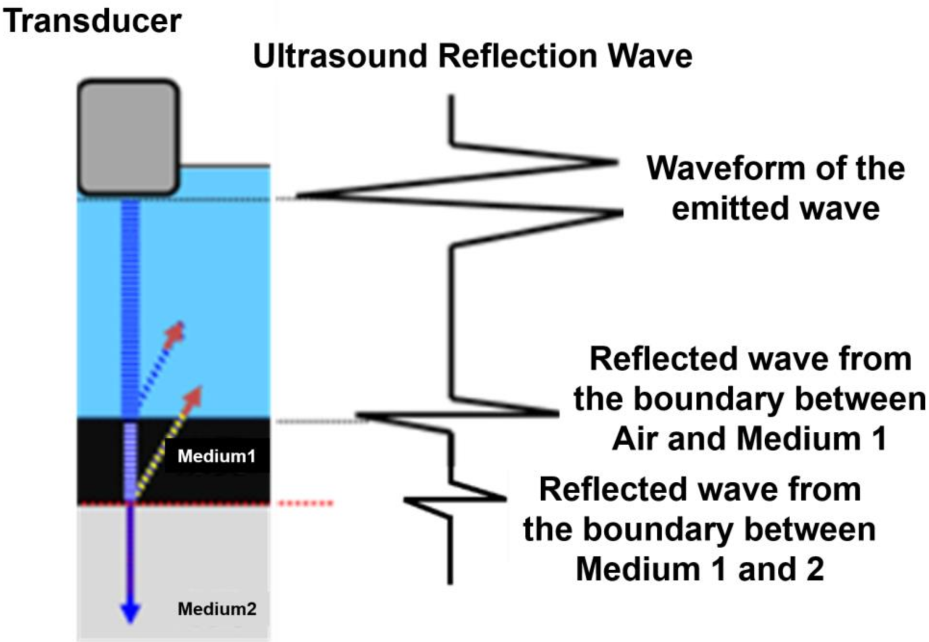

Fig.3.3 Waveform reflected at the boundary of the medium due to the difference in the acoustic impedance of the medium in ultrasonic reflection measurement

$$R(\text{Reflectivity}) = \frac{Z_2 - Z_1}{Z_2 + Z_1} \times 100$$

$\mathrm{Z(Impedance)} = \rho\mathrm{(Density)} \times \mathrm{C(Sound\ speed)}$

- Z_1: Incident acoustic impedance
- Z_2: Transmission side acoustic impedance

Fig.3.4 Reflectance and acoustic impedance

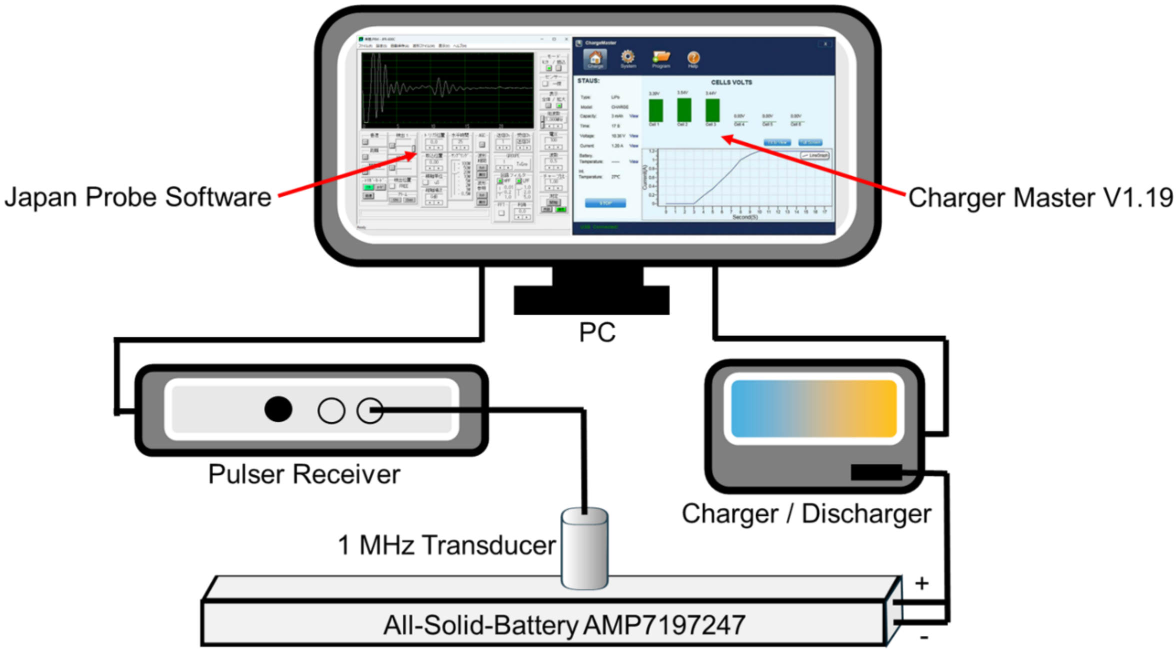

Fig 3.5 Configuration Diagram of the Ultrasonic Measurement System

Fig 3.6 Measurement of All-Solid-State AMP-Battery Using Ultrasonic Transducer

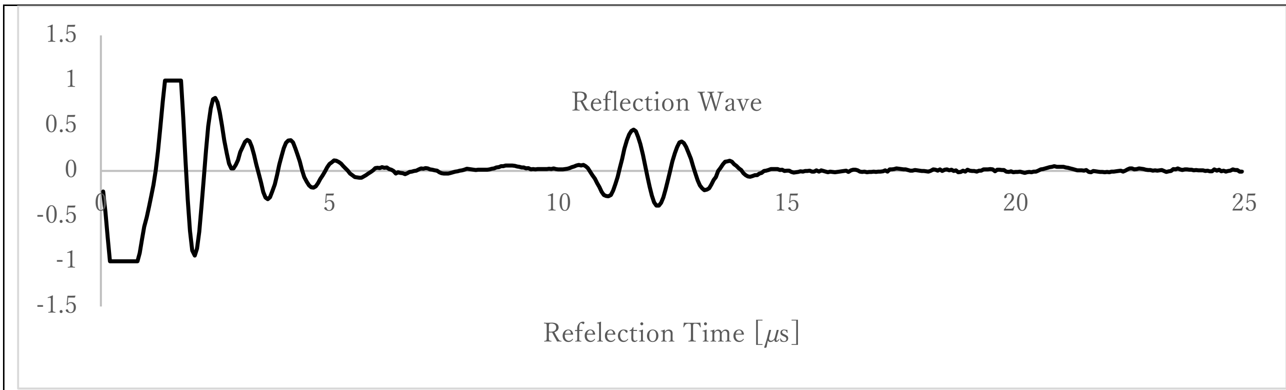

Fully Discharged All-Solid-State AMP-Battery

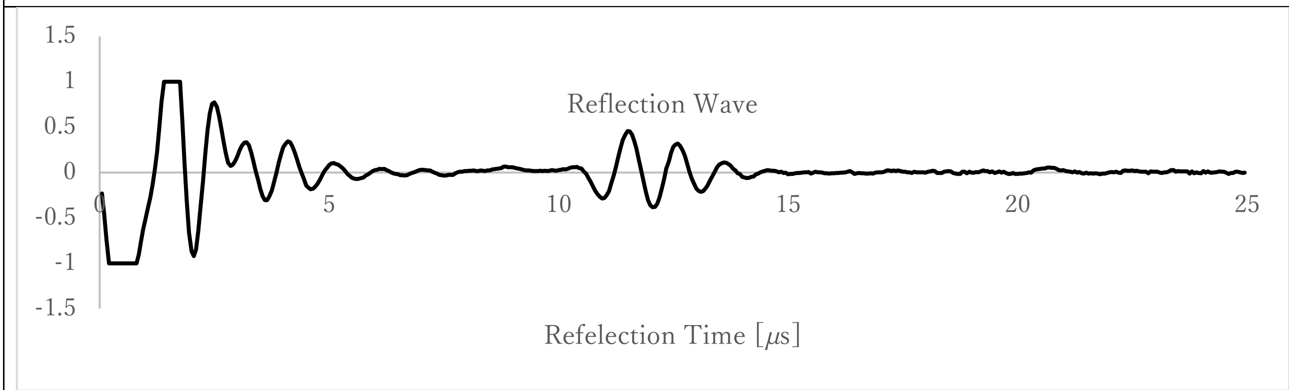

All-Solid-State AMP-Battery Charged to 1500mAh

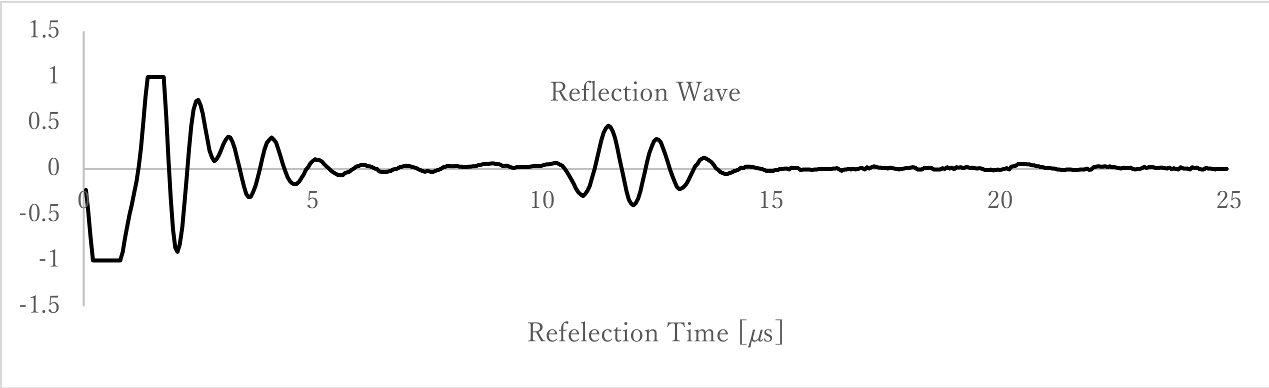

All-Solid-State AMP-Battery Charged to 3000ｍAh

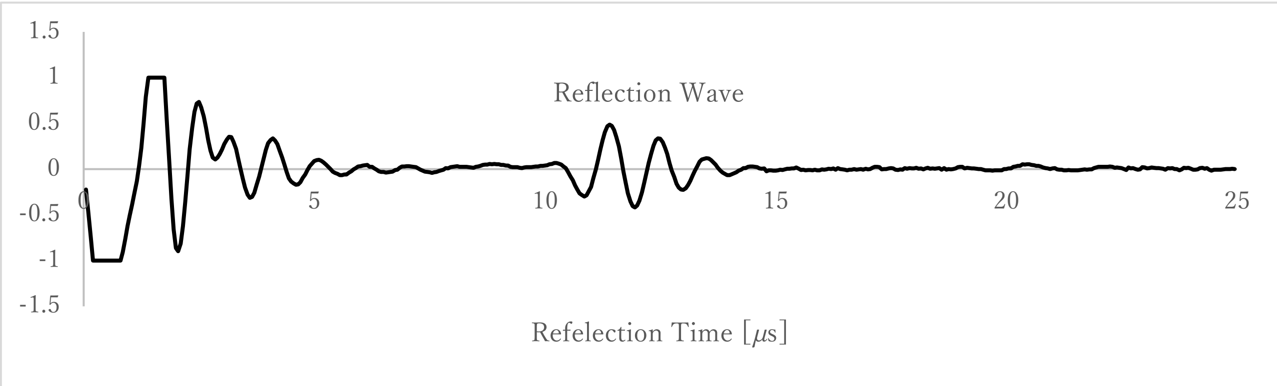

All-Solid-State AMP-Battery Charged to 4500ｍAh

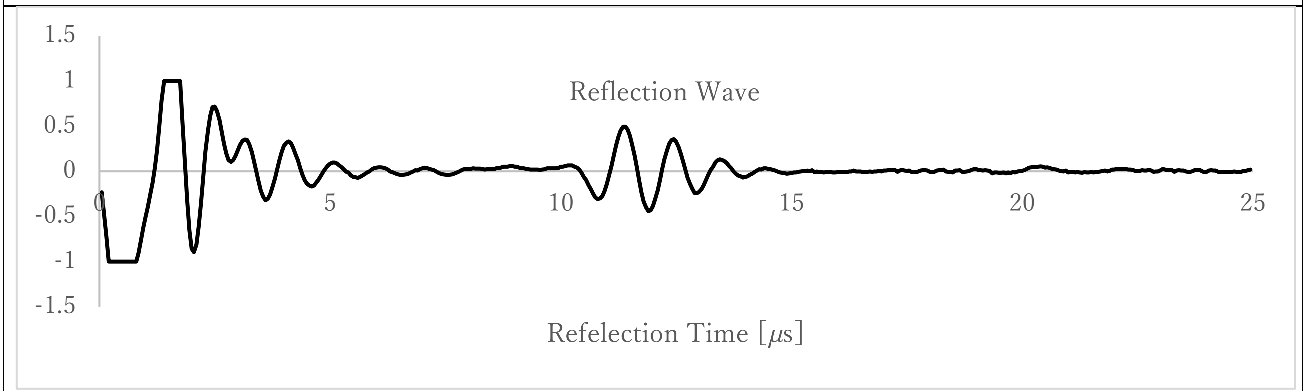

All-Solid-State AMP-Battery Charged to 6000ｍAh

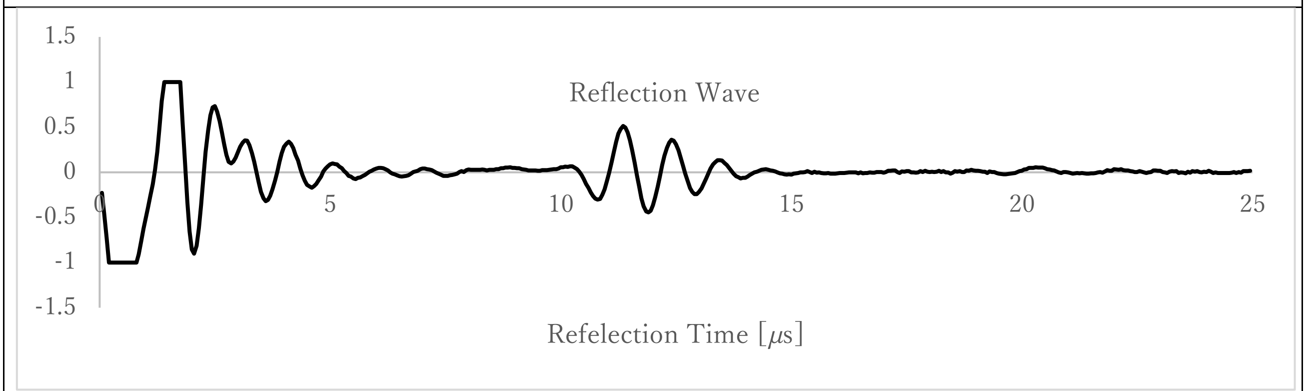

All-Solid-State AMP-Battery Charged to 7500ｍAh

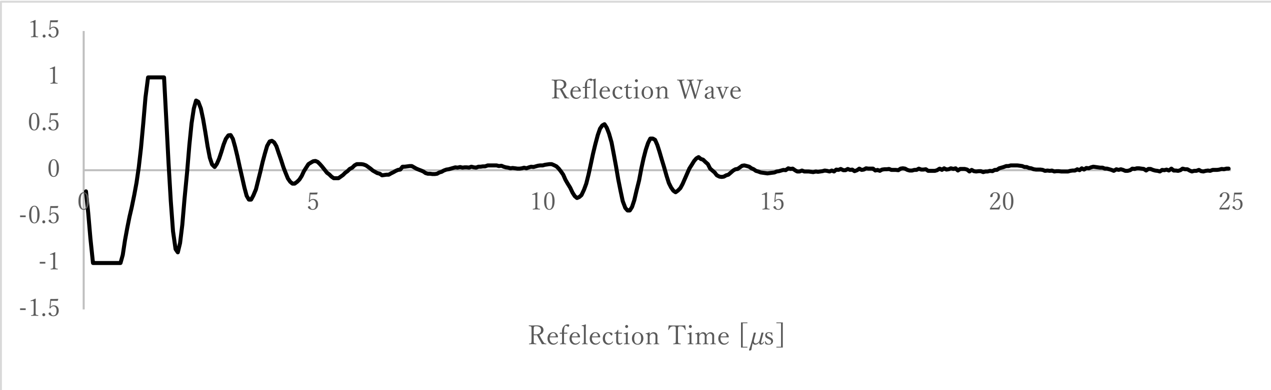

All-Solid-State AMP-Battery Charged to 9000ｍAh

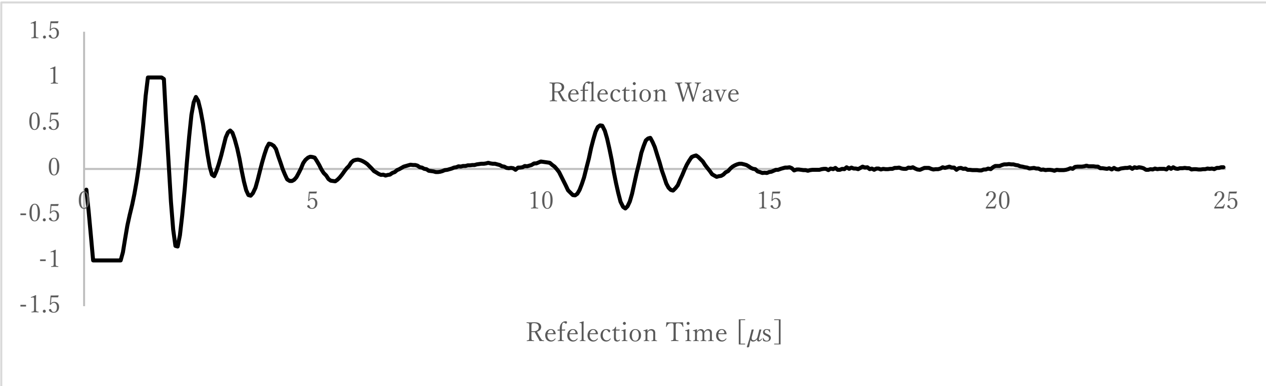

All-Solid-State AMP-Battery Charged to 10500ｍAh

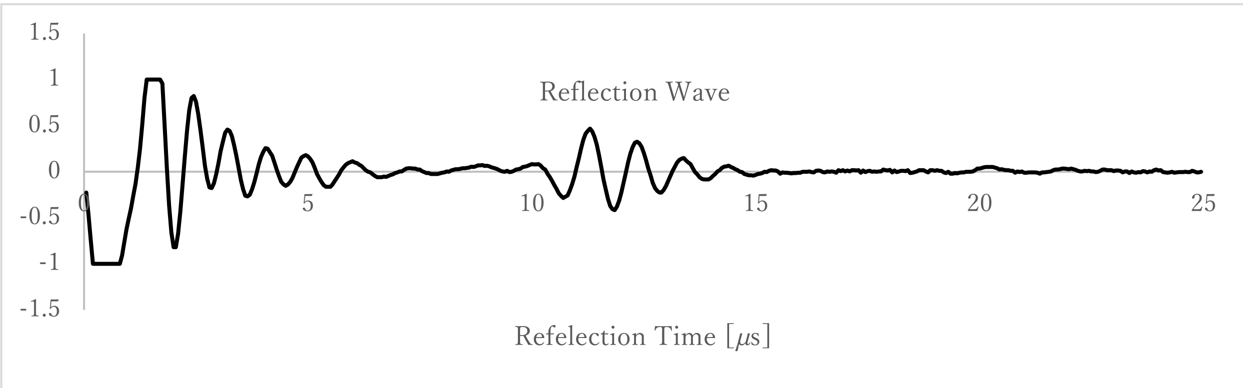

All-Solid-State AMP-Battery Charged to 12000ｍAh

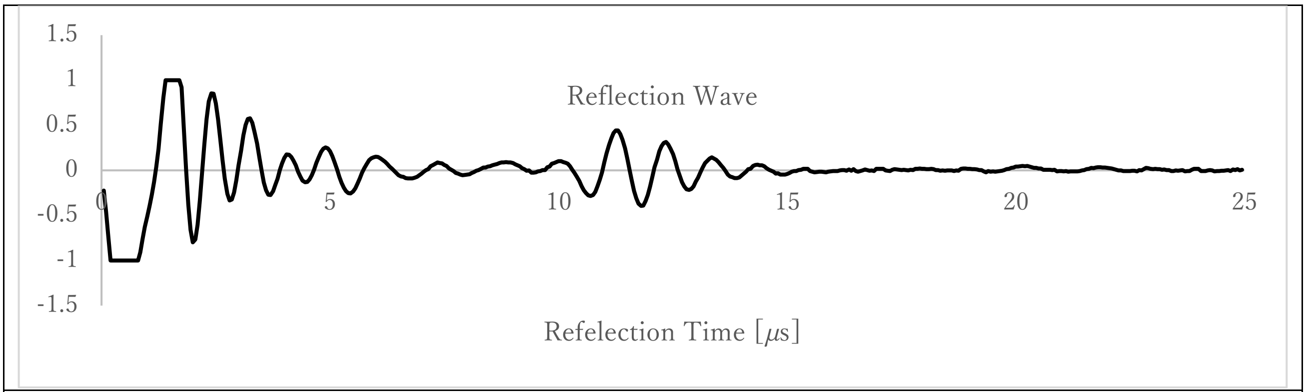

All-Solid-State AMP-Battery Charged to 13500mAh

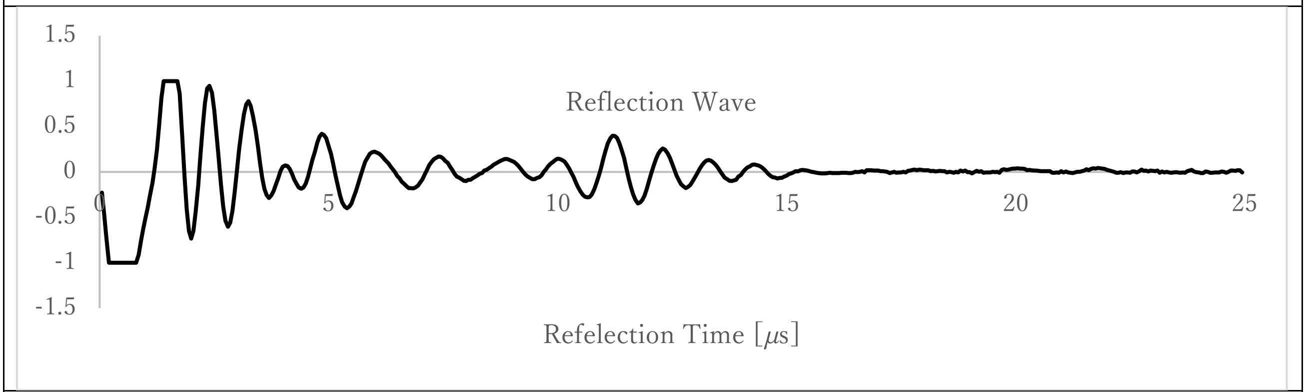

All-Solid-State AMP-Battery Charged to 15000mAh

Fig 3.7 Reflection Waveforms During Charging of All-Solid-State Battery

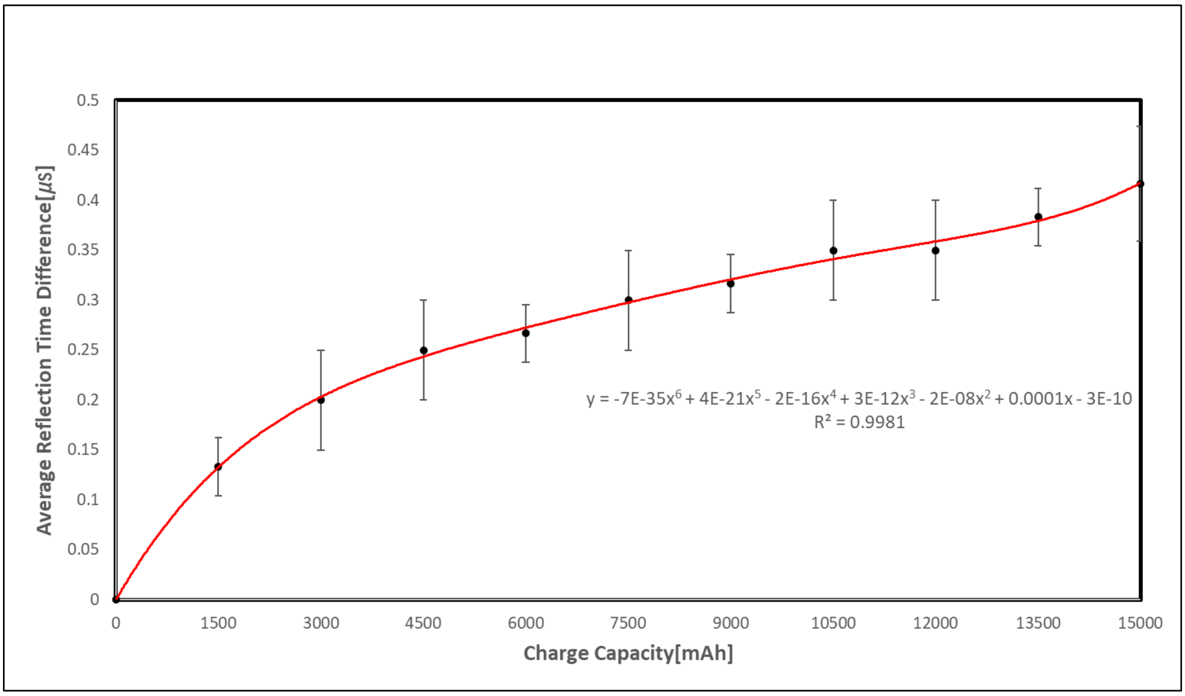

Fig 3.8 Relationship Between Charging Capacity and Waveform Shift

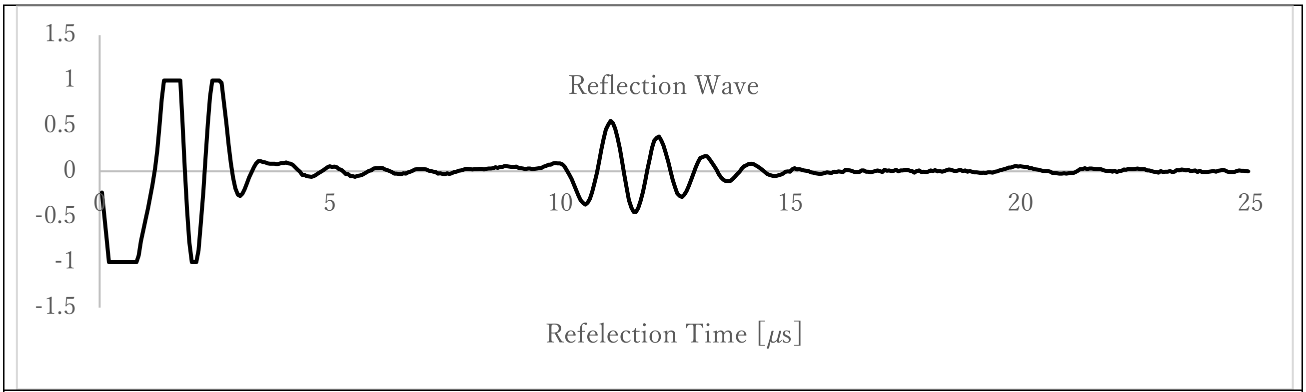

Fully Charged All-Solid-State AMP-Battery

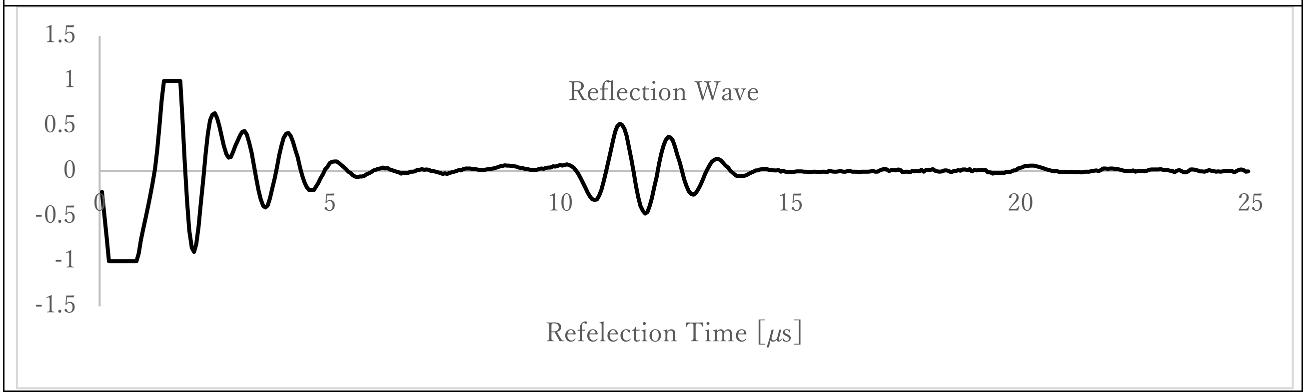

All-Solid-State AMP-Battery Discharged for 1500mAh

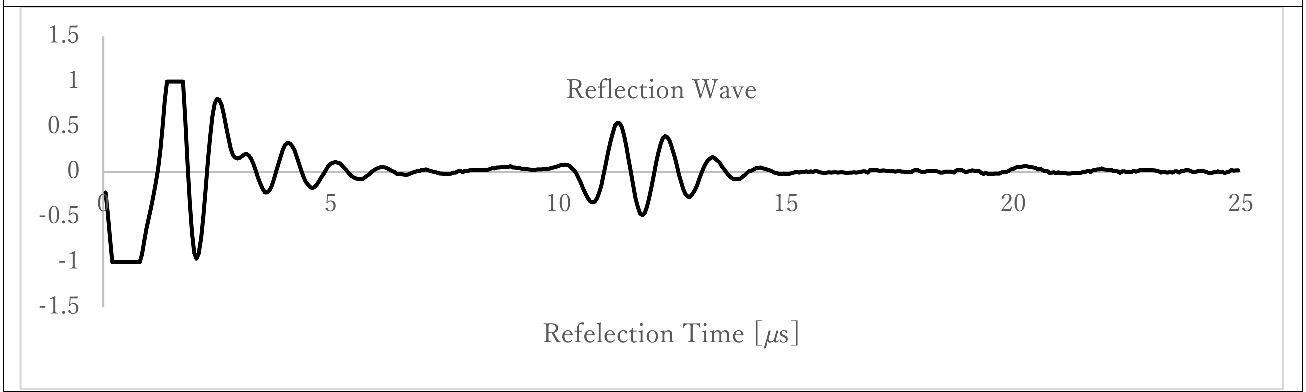

All-Solid-State AMP-Battery Discharged for 3000mAh

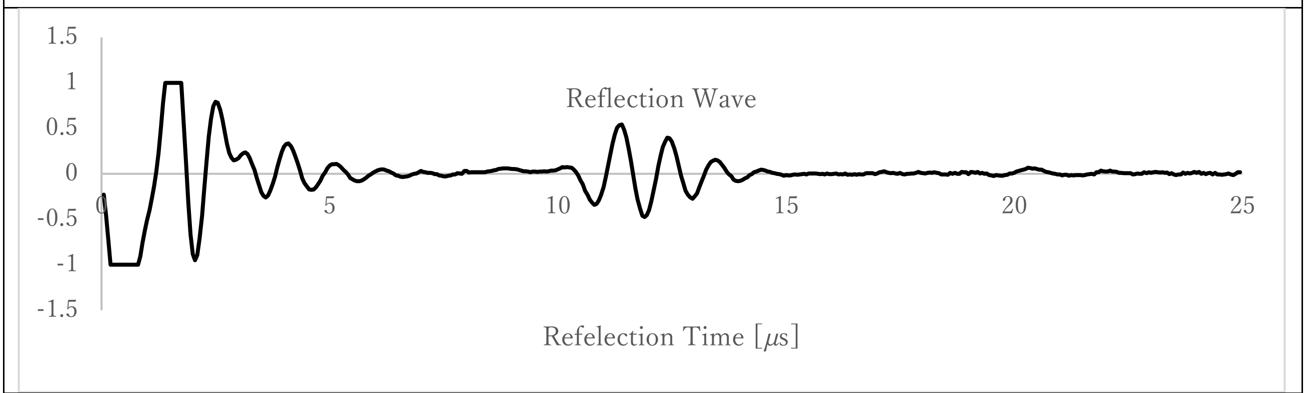

All-Solid-State AMP-Battery Discharged for 4500mAh

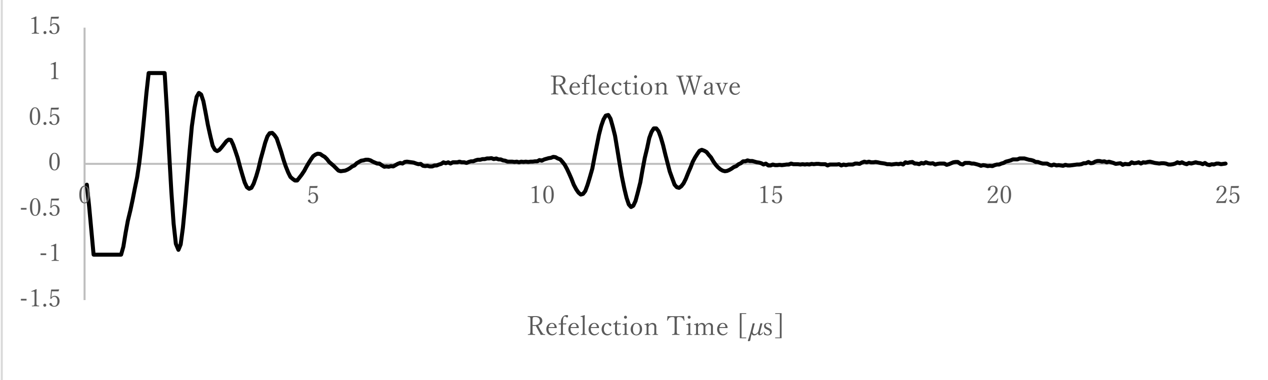

All-Solid-State AMP-Battery Discharged for 6000mAh

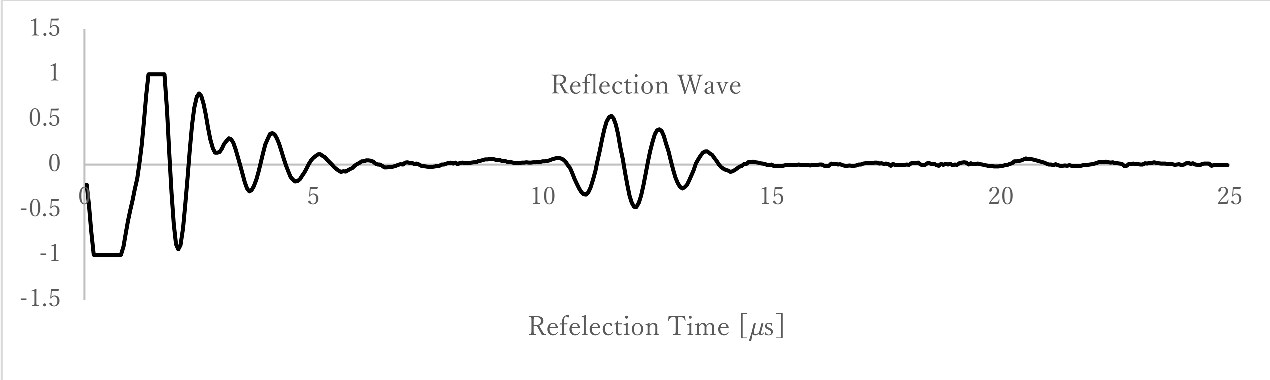

All-Solid-State AMP-Battery Discharged for 7500mAh

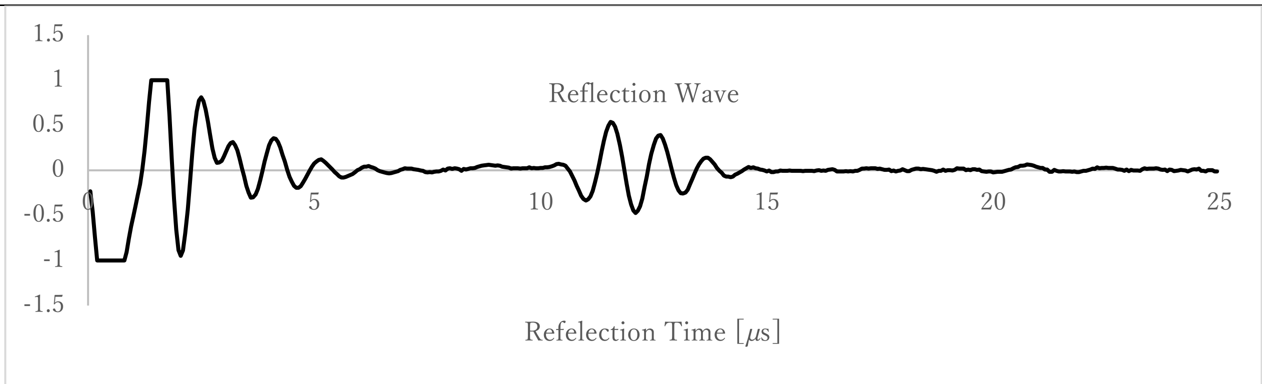

All-Solid-State AMP-Battery Discharged for 9000mAh

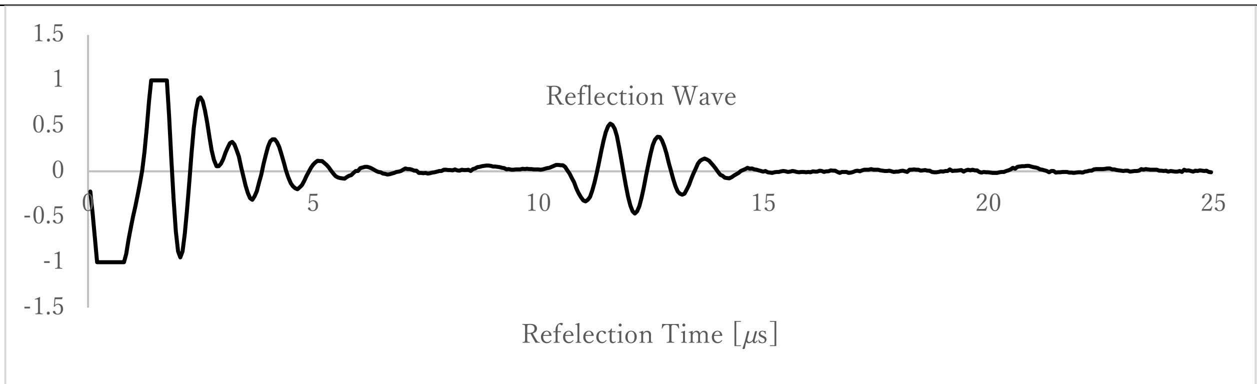

All-Solid-State AMP-Battery Discharged for 10500mAh

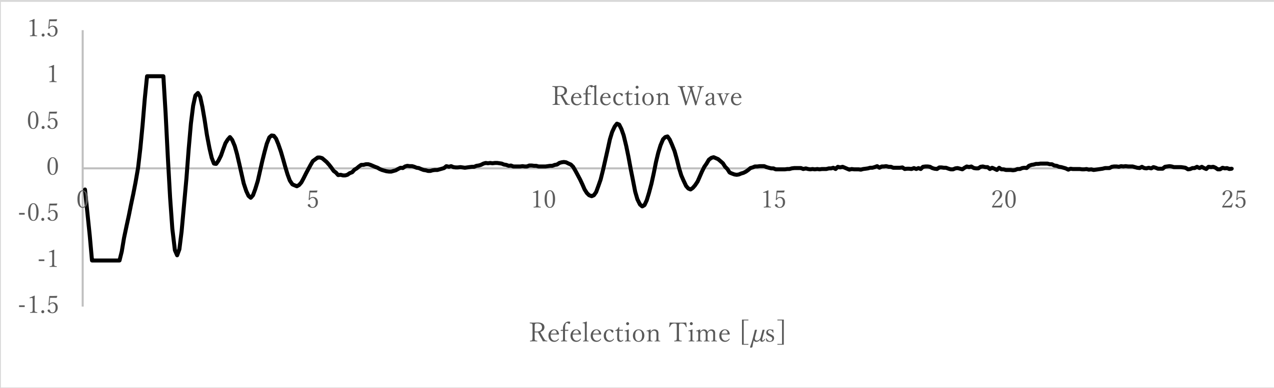

All-Solid-State AMP-Battery Discharged for 12000ｍAh

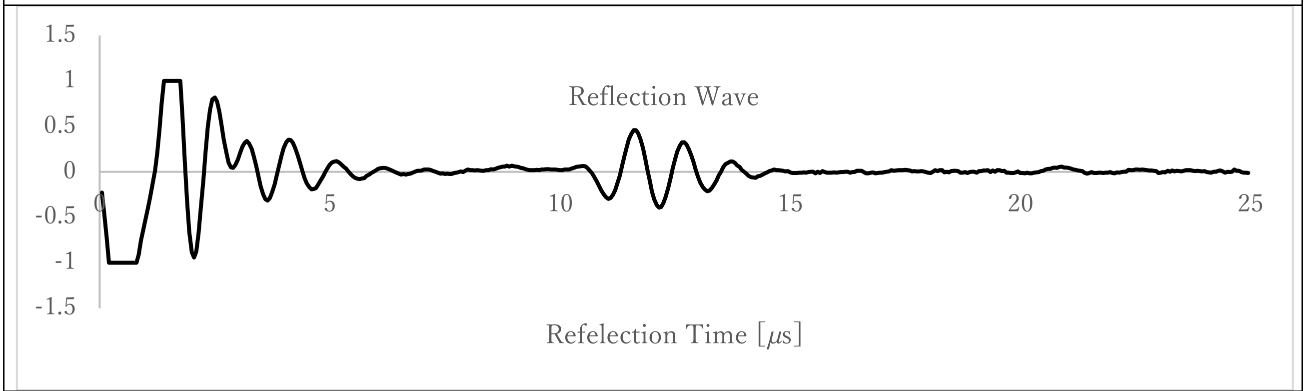

All-Solid-State AMP-Battery Discharged for 13500ｍAh

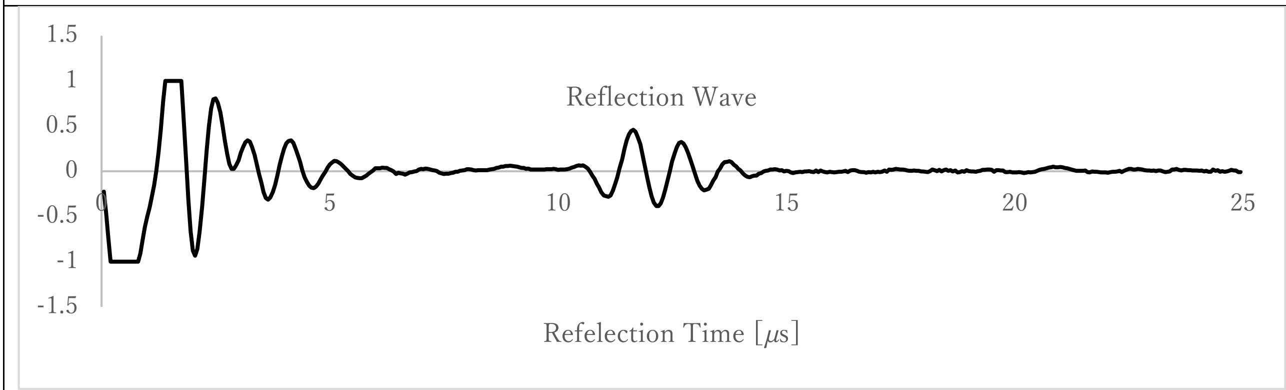

All-Solid-State AMP-Battery Discharged for 15000ｍAh

Fig 3.9 Reflection Waveforms During Discharging of All-Solid-State AMP-Battery

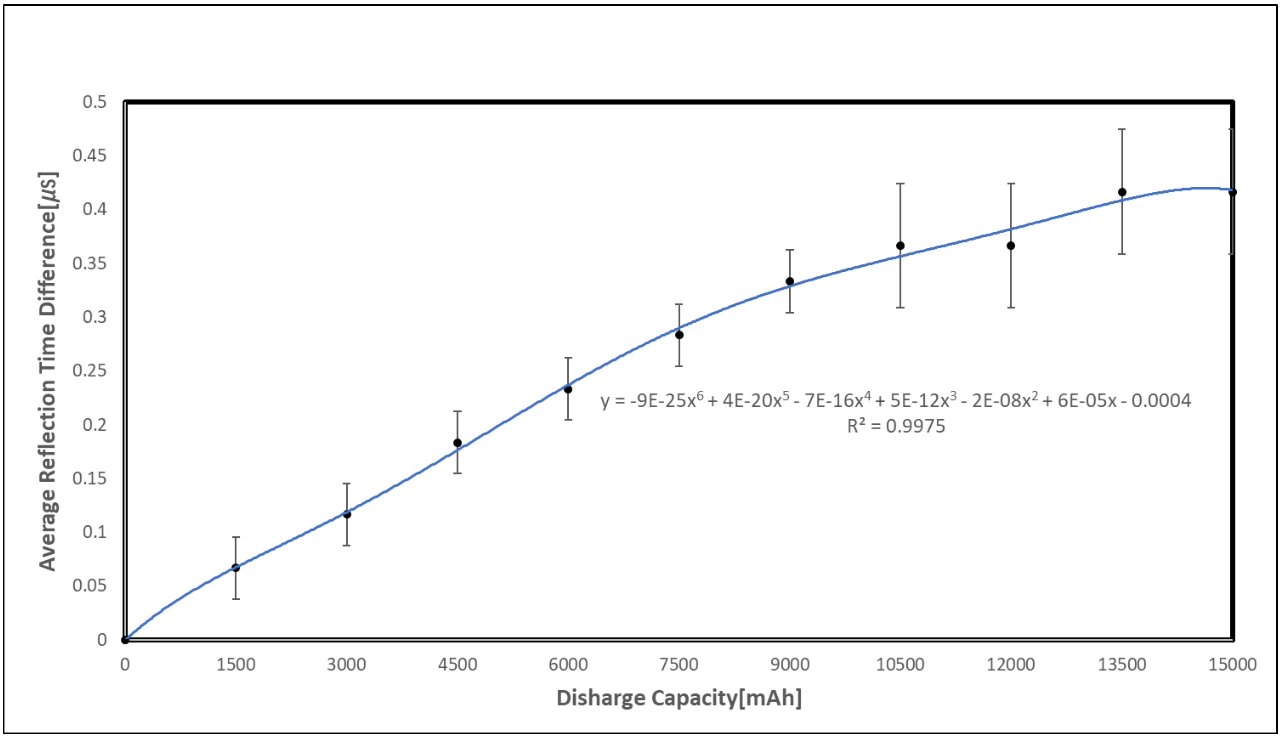

Fig 3.10 Relationship Between Discharge Capacity and Waveform Shift

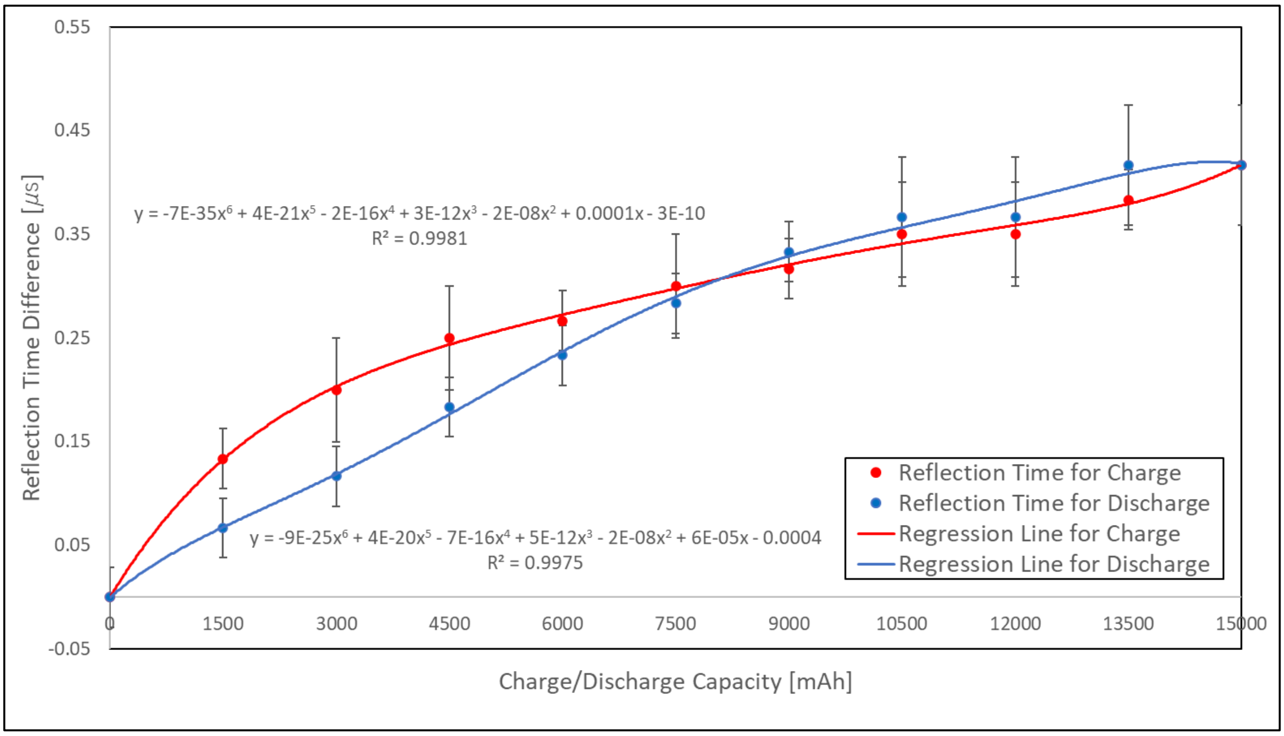

Fig 3.11 Relationship Between Battery Capacity and Time to Obtain Reflection Waveform

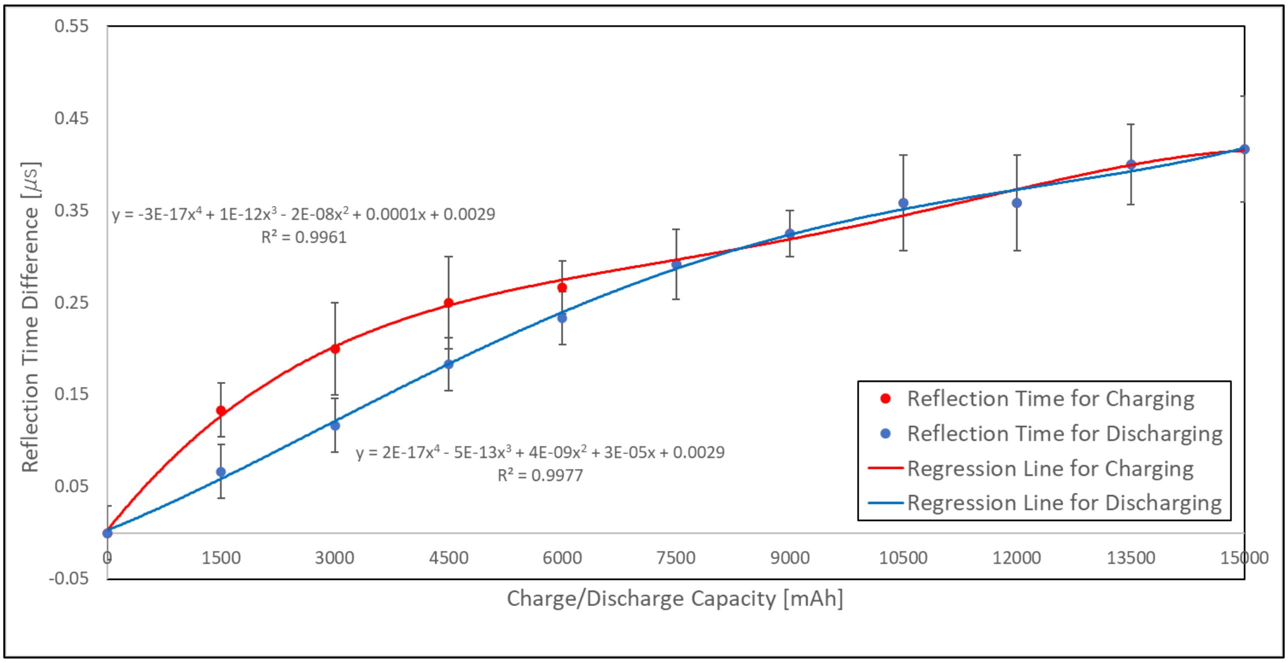

Fig 3.12 Relationship Between Battery Capacity and Time to Obtain Reflection Waveform

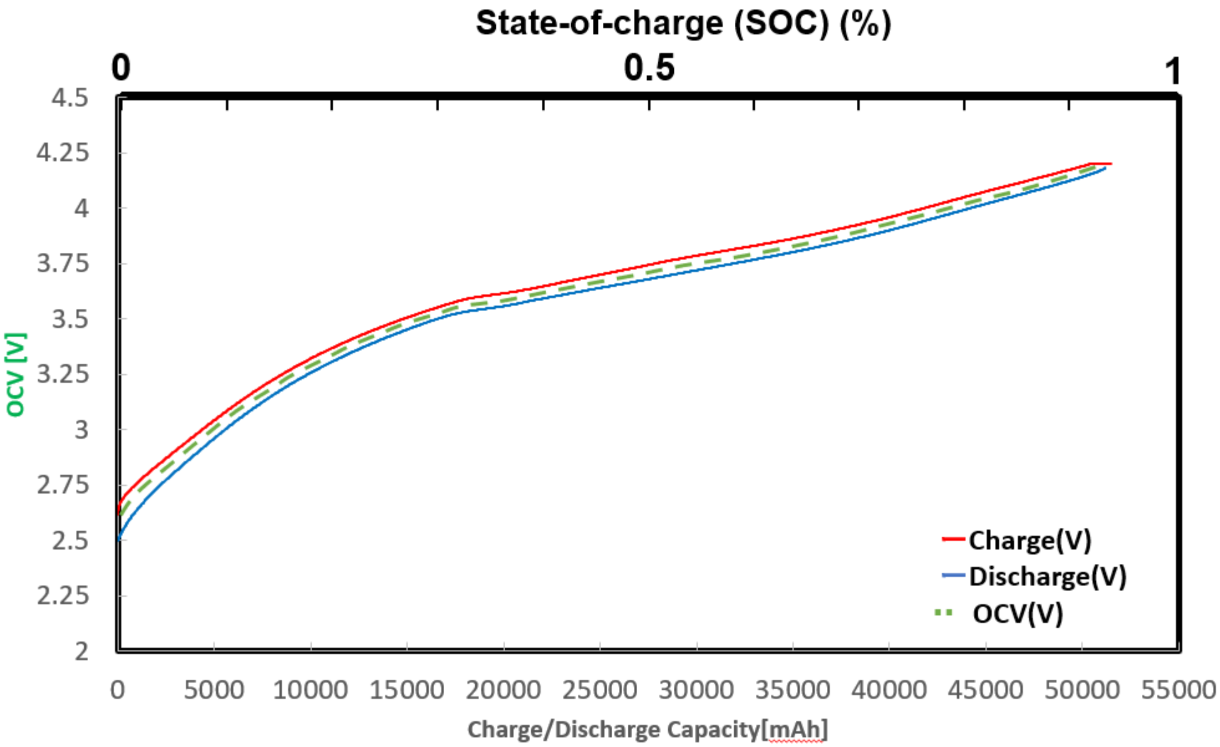

Fig.3.13 OCV line for charging-discharging cycle of All-Solid-State AMP-Battery

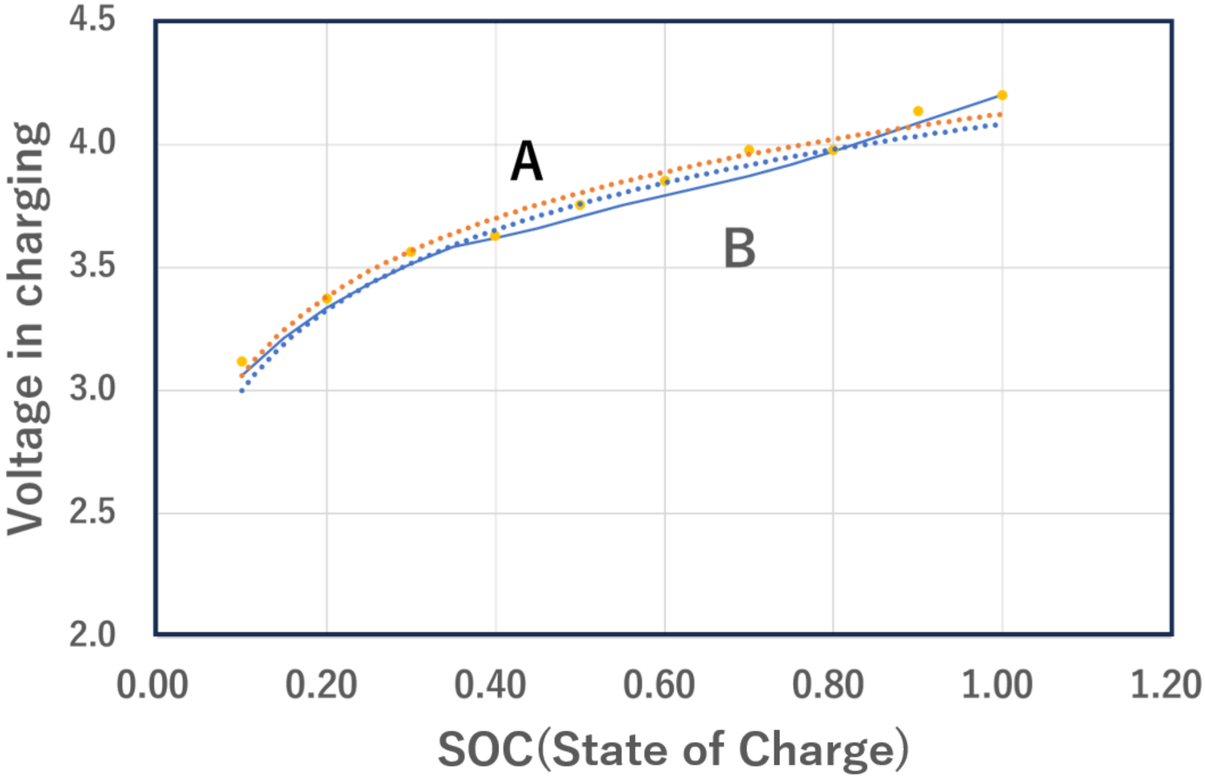

Fig.3.14 Curve A; relationship between converted voltage measured by ultrasonic measurement and SOC (yellow dot is the measured value and the doted line is the logarithmic approximation formula of y=0.4611ln(x)+4.1235), Curve B; between electrical charging voltage and SOC (blue solid line is the measured value and the doted line is the logarithmic approximation formula of y=0.4699ln(x)+4.0837).

Chapter 4

Chapter4 Radiation Resistance Evaluation of All-Solid-State Batteries

4.1 Research Background

The decommissioning of nuclear power plants is a highly technical and safety-critical process, making the use of decommissioning robots indispensable. These robots operate in environments with extremely high radiation levels, where their reliability and durability are directly linked to the success of the decommissioning process [4-1]. However, current battery technology is prone to degradation in high-radiation environments, significantly limiting the operational time and performance of these robots. Therefore, developing radiation-resistant batteries is a crucial task for enhancing the efficiency and safety of decommissioning operations.

In decommissioning operations, achieving a balance between radiation protection and operational efficiency is essential. Human workers face significant challenges in maintaining prolonged operations in high-radiation environments [4-2], which increases the reliance on robots. However, radiation-induced battery degradation limits the operational time of these robots and increases maintenance frequency. Addressing these issues requires batteries that can maintain performance and operate stably over long periods in high-radiation environments.

Lithium-ion batteries are widely used today due to their high energy density and long lifespan [4-3]. However, they face challenges in maintaining performance in high-radiation environments. Radiation significantly impacts the electrolyte and electrode materials of batteries [4-4], leading to capacity reduction and increased risk of internal short circuits. Moreover, radiation-induced chemical changes and physical degradation also affect battery performance. In contrast, ASSBs are composed entirely of solid materials and do not use liquid electrolytes, making them less susceptible to radiation damage.

ASSBs have attracted attention as next-generation batteries due to their high safety and stability [4-5]. Without liquid electrolytes, they have a lower risk of leakage and fire, and can withstand high temperatures and pressures. Additionally, ASSBs have high energy density and minimal degradation during charge-discharge cycles, contributing to their long lifespan. These characteristics suggest that ASSBs may be well-suited for use in high-radiation environments.

However, the performance evaluation of ASSBs in high-radiation environments has not been sufficiently conducted. Previous research has demonstrated the superior performance of ASSBs in high-temperature and high-pressure environments, but data on their radiation resistance is limited. This study aims to thoroughly evaluate the radiation resistance of all-solid-state lithium-ion batteries and verify their practical applicability.

This study evaluates batteries in a high-radiation environment exceeding 100 Gy using a cobalt-60 irradiation chamber to clarify the effects of radiation on the electrical performance and structure of the batteries. Additionally, using the pulse ultrasonic propagation time difference measurement method developed in Chapter 3, the internal structural changes of the batteries during charge-discharge cycles are non-destructively measured. This approach aims to elucidate the degradation mechanisms of batteries in high-radiation environments and provide design guidelines for radiation-resistant batteries.

Such research represents an important step toward the practical application of ASSBs as a power source for decommissioning robots. Radiation-resistant batteries also have potential applications in other high-radiation environments, such as space exploration and nuclear fuel cycle facilities. Therefore, this study opens new possibilities for ASSBs technology and is expected to contribute to technological innovation across various fields.

4.2 Research Objectives

The primary objective of this study is to thoroughly evaluate the radiation resistance of ASSBs in high-radiation environments and to elucidate their applicability to decommissioning robots. To achieve this goal, first, charge-discharge cycles of all-solid-state lithium-ion batteries will be conducted in a cobalt-60 irradiation chamber under high-radiation environments exceeding 100 Gy, and their electrical performance will be evaluated. Next, using the pulse ultrasonic propagation time difference measurement method developed in Chapter 3, internal structural changes in the batteries will be non-destructively measured. This method will allow for a detailed analysis of the degradation state of the electrodes and electrolytes after radiation exposure. Furthermore, the performance of the batteries will be assessed not only under short-term radiation exposure but also over long periods in high-radiation environments to verify their reliability and durability for long-term use. The internal structural changes of the batteries after 72 hours of irradiation in a high-radiation environment will be evaluated to verify their reliability and durability for long-term use.

4.3 Experiment Methods

4.3.1 Experimental Equipment and Materials

The radiation measurement system is shown in **Figure 4.1**. This measurement system includes a charger (Skyrc D200neo) and a discharger (Hitec AD350). The charging and discharging are controlled using Skyrc's dedicated software, Charge Master V1.19. The ASS-AMP-B models used in this experiment are AMP9070140 (rated capacity 7500mAh, operating voltage 3.7V, rated current 7.5A) and AMP7197247 (rated capacity 15,000mAh, operating voltage 3.85V, rated current 4.4A). The battery temperature is maintained at 25°C, and the discharge current is kept constant during measurements. The specific equipment specifications are shown in **Tables 4.1-4.4**.

4.3.2 Experimental Design

(1) Radiation Experiment with All-Solid-State AMP-Battery AMP9070140

The anode and cathode of the ASS-AMP-B are connected to the charger Skyrc D200neo, which is then connected to the discharger Hitec AD350 to discharge the ASS-AMP-B. The charger Skyrc D200neo is connected to a computer via USB, and the software Charge Master is used to record the changes in voltage, current over time, and capacity during the discharge process of the ASS-AMP-B. To prepare for the discharge experiment, the ASS-AMP-B is fully charged. After the ASS-AMP-B is fully charged, the discharge experiment is conducted in a radiation environment. The discharge process continues from 100% charge until the charger automatically stops when it can no longer discharge. The changes in voltage, current over time, and capacity data are recorded through the software Charge Master.

In this experiment, the standard charge and discharge current of 1C (7.5A) was used for the ASS-AMP-B (**Figure4.2**).

(2) Radiation Experiment with All-Solid-State AMP-Battery AMP7197247

The anode and cathode of the all-solid-state lithium battery are connected to the charger Skyrc D200neo, which is then connected to the discharger Hitec AD350 to discharge the ASS-AMP-B. The charger Skyrc D200neo is connected to a computer via USB, and the software Charge Master is used to record the changes in voltage, current over time, and capacity during the discharge process of the ASS-AMP-B. To prepare for the discharge experiment, the ASS-AMP-B is fully charged. After the ASS-AMP-B is fully charged, the discharge experiment is conducted in a radiation environment. The discharge process continues from 100% charge until the charger automatically stops when it can no longer discharge. The changes in voltage, current over time, and capacity data are recorded through the software Charge Master.

In this experiment, the standard charge and discharge current of 0.2C (4.4A) was used for the ASS-AMP-B (**Figure 4.3**).

4.4 Experimental Results and Discussion

4.4.1 Changes in Discharge Performance

(1) Radiation Experiment with All-Solid-State AMP-Battery AMP9070140

The current, voltage and capacity result for ASS-AMP-B AMP9070140 are shown as **Figure 4.4** which the source distance is 0.2m (260Gy/h) and **Figure 4.5** which source distance 0.5m (44Gy/h). The blue curve represents the voltage, red curve represents the current and the number under graph shows the capacity. From the result, even the distance of the battery to the radiation source changes from 0.2m to 0.5m, the trend of current and voltage seems similar, and the capacity of the battery for discharging is similar too. This result indicates that the effect on current, voltage and discharge capacity from the radiation is little, the battery keeps stable in electrical.

(2) Radiation Experiment with All-Solid-State AMP-Battery AMP7197247

The current, voltage and capacity result for ASS-AMP-B AMP7197247 are shown as **Figure 4.6** which the source distance is 0.2m (260Gy/h) and **Figure 4.7** which source distance 0.5m (44Gy/h). The blue curve represents the voltage, red curve represents the current and the number under graph shows the capacity. From the result, even the distance of the battery to the radiation source changes from 0.2m to 0.5m, the trend of current and voltage seems similar, and the capacity of the battery for discharging is similar too. This result indicates that the effect on current, voltage and discharge capacity from the radiation is little, the battery keeps stable in electrical.

4.4.2 Comparative Analysis

Figure 4.8 shows the current, voltage and capacity change of ASS-AMP-B AMP9070140 under radiation environment and normal environment. The blue curve represents the voltage, red curve represents the current and the number under graph shows the capacity. From the result, the trend of current and voltage seems similar, and the capacity of the battery for discharging is similar too. This result indicates that the effect on current, voltage and discharge capacity from the radiation is little, the battery keeps stable in structure.

4.4.3 The Effect of Radiation on Ultrasound Reflection Time

To test the changes in the internal structure of ASS-AMP-B under strong nuclear radiation, pulsed ultrasonic evaluation method developed in Chapter 3 has been used to detect the batteries before and after radiation exposure. As shown in the **Figure 4.9**, the upper graph represents the reflection wave curve of the ASS-AMP-B before nuclear radiation, while the lower graph shows the ultrasonic reflection wave curve after 1 hour of nuclear radiation exposure. We found that the reflection wave time corresponding to the peak of the reflection wave curve remained almost unchanged.

To further determine the internal structural changes of ASS-AMP-B under prolonged strong radiation conditions, we placed the batteries in a strong radiation environment for 8 hours, testing the reflection wave curve every hour. The experiment condition is shown in **Table 4.5**. The experimental results are shown in the **Figure 4.10**. Despite 8 hours of strong radiation exposure, the time corresponding to the peak of the ultrasonic reflection wave did not change, remaining at 11.35 microseconds. This experiment fully demonstrates that ASS-AMP-B can maintain structural stability in a strong radiation environment.

And also, a furthermore experiment has been done to check the structural and electrical stability. The battery is furthermore taken the radiation about 1000Gy/h for 72 hours, and the ultrasound reflection result is shown in **Figure 4.11.** From the ultrasound result, it indicates that the reflection wave did not move even the battery is under radiation for 72hours. The result indicates that ASS-AMP-B has an extremely good stability under high-radiation environment for both electrical and structural.

4.4.4 Analysis of Energy Imparted from Radiation and the Capability using in Decommissioning Robot

In this research, the radiation source is cobalt-60 and the main radiation of it is γ ray. Cobalt-60 emits two gamma rays with the energies about 1.17Mev and 1.33Mev. The radioactive element with the highest concentration in the Fukushima nuclear power plant waste is Cesium-137 (Cs-137). Cesium-137 emits gamma rays with the energy about 0.662Mev. Even the element of radiation source is different for experiment and Fukushima nuclear power plant waste, the type of ray is the same and the energy of Cobalt-60 is larger than Cesium-137, which means the ASSB can be used for decommissioning robot.

Furthermore, for the imparted energy of battery which used for the experiment, it can be calculated using the equation:

$$E_{\gamma} = D \times m \times t \qquad 5.1$$

Where E_γ is radiation energy, D is the radiation density, m is the battery weight and t are the time.
In this research, the radiation density is 1000Gy/h, battery weight is 0.34kg, so the radiation energy imparted for 1 hour can be calculated as:

$$E_\gamma = \frac{1000Gy}{h} \times 0.34kg \times 1h = 340J$$

Since the battery considered to be used for the robots which works for the debris removal of nuclear power plant, the radiation effect besides γ ray, such as β ray is also should be taken into consideration. β rays are streams of high-speed electrons or positrons. When a battery is exposed to β rays, the positive and negative electrode materials indeed undergo ionization, which involves the gain or loss of electrons. About the Ionization of the positive and negative electrode materials, during the normal charging and discharging process of a battery, for charging process, the positive electrode loses electrons, and the negative electrode gains electrons. And for discharging process, the positive electrode gains electrons, and the negative electrode loses electrons. Therefore, the ionization reactions caused by β-ray irradiation in the positive and negative electrode materials are not significant.

Furthermore, considering about the effect of neutron, the impact of neutron radiation on ASSBs differs from that of gamma rays, as neutrons are uncharged and possess higher penetration capabilities. Neutrons interact with atomic nuclei, potentially causing structural changes and performance degradation in materials. Firstly, neutron radiation can alter the atomic structure of materials, causing displacement damage and thermal neutron capture, thereby affecting the electrochemical performance of the battery. For example, when neutrons collide with atomic nuclei, they can displace atoms from their lattice positions, creating vacancies and interstitial atoms, leading to displacement damage. This damage can alter the mechanical strength and electrical conductivity of the materials, thus impacting the overall performance of the battery. To mitigate these effects, materials with higher neutron radiation resistance can be selected, such as certain ceramic electrolytes, which exhibit excellent radiation resistance and structural stability.

Neutron radiation may also cause the generation of gases, swelling, or other physical changes in battery materials, further affecting the mechanical integrity and electrical performance of the battery. For instance, neutron capture reactions can produce gases like hydrogen or helium. The accumulation of these gases within the material can lead to swelling or bubble formation, compromising the integrity and uniformity of the material, and impacting the long-term stability and safety of the battery.

4.4.5 Analysis of Radiation Transparency of All-Solid-State AMP-Battery

In high-radiation environments such as nuclear facilities, spacecraft, and radiation-prone areas, the stability and durability of power sources are paramount. ASSBs are increasingly being utilized in these contexts due to their inherent safety and high energy density. However, understanding the transmission of gamma rays through these batteries is crucial for ensuring their long-term performance and reliability.

Gamma rays, being highly energetic, can penetrate battery materials, potentially causing ionization and other forms of radiation damage. The ability of a battery to resist such penetration, i.e., its radiation transparency, directly impacts its structural integrity and electrochemical performance. Therefore, the study of gamma ray transmission rates through ASSBs is essential for predicting and enhancing their operational lifespan in radiation-heavy environments.

Calculating the transmission rate of gamma rays provides valuable insights into the behavior of ASSBs under radiation. This involves understanding the linear attenuation coefficients of the battery's materials—such as the cathode, anode, and electrolyte—and their combined effects on gamma ray attenuation. By determining how much gamma radiation penetrates the battery, researchers can evaluate electrical performance degradation, including changes in discharge capacity, internal resistance, and efficiency. Accurate transmission calculations aid in material selection for superior radiation resistance, optimizing battery design to maximize protection without increasing weight, and ensuring safety in high-risk applications like nuclear decommissioning and space missions.

Incorporating gamma ray transmission calculations into the development of ASSBs involves both theoretical and experimental approaches. Researchers use databases such as NIST XCOM to obtain linear attenuation coefficients for elements within the battery. Experiments are conducted to validate these theoretical models, ensuring accuracy and reliability.

ASS-AMP-B AMP7197247 has been used to calculate the transmission rate of gamma rays provided by cobalt 60. ASS-AMP-B AMP7197247 is polymer-based battery and volume of cathode, anode and electrode is about 35%, 30% and 35%, and the material of them are commonly used as lithium cobalt oxide ($LiCoO_2$), graphite and polyethylene oxide (PEO). The main elements used for cathode, anode and electrode are cobalt (Co), carbon (C) and oxygen (O). The attenuation coefficient of cobalt, carbon and oxygen can be got from "NIST XCOM Photon Cross Sections Database", which are shown in **Table 4.6** when gamma rays emitted from cobalt 60 with the energies about 1.17Mev and 1.33Mev. Since the thickness of AMP7197247 is 7.1mm, the thickness for cathode, anode and electrode are 2.485mm, 2.13mm and 2.485m. Beer–Lambert law has been used to calculate the transmission rate and the equation is shown as below:

$$I = I_0 e^{-\mu d} \tag{5.2}$$

where I is the intensity of the gamma rays after passing through the material, I_0 is the initial intensity of the gamma rays before encountering the material, μ is the linear attenuation coefficient of the material, which indicates how strongly the material absorbs or scatters the gamma rays, d is the thickness of the material.

Using equation 5.2, when energy from gamma rays is 1.17MeV, then each transmission rate of gamma rays for cathode, anode and electrode can be calculated as below:

1. Cathode ($LiCoO_2$):

$$I_1 = I_0 e^{-0.0670\times 0.2485} \approx I_0 e^{-0.0167} \approx 98.35 I_0 \tag{5.3}$$

2. Electrode (PEO)

$$I_2 = I_1 e^{-0.0325\times 0.213} \approx I_1 e^{-0.0069} \approx 99.31 I_1 \tag{5.4}$$

3.Anode (Graphite)

$$I_{final} = I_2 e^{-0.0325\times 0.2485} \approx I_2 e^{-0.0081} \approx 99.19 I_2 \tag{5.5}$$

So, the transmission rate of gamma rays in total T can be calculated as below:

$$T = \frac{I_{final}}{I_0} \approx 98.35 \times 99.31 \times 99.19 = 97.85\% \tag{5.6}$$

From the result, the transmission rate of cobalt-60 gamma rays through a 7.1 mm thick polymer-based all-solid-state battery is approximately 97.85%.

For using the same method, considering the radioactive element with the highest concentration in the Fukushima nuclear power plant waste is Cesium-137 with energy is 0.662Mev, the transmission rate of Cesium-137 is about 96.8%.

The transmission rate of cobalt-60 gamma rays through a 7.1 mm thick polymer-based ASS-AMP-B is approximately 97.85% and for Cesium-137 is 96.8%. This high transmission rate indicates that the battery materials (including polymer electrolytes and specific electrode components) have low gamma ray attenuation coefficients, allowing most of the gamma ray energy to pass through without being absorbed. Although the gamma ray transmission rate is high, the interaction primarily occurs through ionization effects rather than direct atomic displacement, thus not easily causing significant crystal defects. Gamma rays mainly interact with the electrons in the material through ionization, generating free electrons and holes. This effect may alter the internal charge distribution of the material but typically does not lead to severe crystal structure defects. Since gamma rays are uncharged, they interact with the material primarily through ionization and Compton scattering, unlike neutrons that cause direct atomic displacement, hence gamma rays generally do not cause significant crystal structure displacement damage.

4.5 Conclusion

In this study, the performance of ASSB was tested in a nuclear radiation environment. The results confirmed that ASSBs possess high radiation resistance and can discharge normally even under radiation conditions. Experimental results showed that ASSBs retained their discharge performance and maintained internal structural stability after radiation exposure. This indicates that ASSBs can be reliable energy sources for nuclear waste disposal robots and other applications in radiation environments. Long-term performance evaluations in radiation environments will enable further improvements and expand the application range of ASSBs. The transmission rate of cobalt-60 gamma rays through a 7.1 mm thick polymer-based all-solid-state battery is approximately 97.85% and for Cesium-137 is 96.8%. This high transmission rate indicates that the battery materials have low gamma ray attenuation coefficients, allowing most of the gamma ray energy to pass through without being absorbed. Since gamma rays are uncharged, they interact with the material primarily through ionization and Compton scattering, unlike neutrons that cause direct atomic displacement, hence gamma rays generally do not cause significant crystal structure displacement damage.

References

[4-1] Ioannis Tsitsimpelis, C.James Taylor, Barry Lennox, Malcolm J. Joyce, A review of ground-based robotic systems for the characterization of nuclear environments, (2019) Progress in nuclear energy, Vol.111, pp.109-124.

[4-2] Junhao Zhang, Weiwei Chen, Bingyu Ni, Jing Zheng, Kaixin Zhao, Wanyi Tian, Optimization of Personnel Work Paths During Decommissioning of Nuclear Facilities, (2024) Nuclear science and engineering, Vol.198, pp.1668-1681.

[4-3] Boucar Diouf, Ramchandra Pode, Potential of lithium-ion batteries in renewable energy, (2015) Renewable energy, Vol.76, pp.375-380.

[4-4] Muhammad Mominur Rahman, Wei-Ying Chen, Linqin Mu, Zhengrui Xu, Ziqi Xiao, Meimei Li, Xian-Ming Bai ,Feng Lin, Defect and structural evolution under high-energy ion irradiation informs battery materials design for extreme environments, (2020) Nature communications, Vol.11, paper number 4548.

[4-5] Dongsoo Lee, Hyungjun Lee, Taeseup Song, Ungyu Paik, Toward High Rate Performance Solid-State Batteries, (2022) Advanced energy materials, Vol.12, paper number 2200948.

Table 4.1 Specifications of Balance Charger/Discharger (Skyrc D200neo)

AC input voltage	100-240V
DC input voltage:	10-30V
Charging current range	0.1-20A
Discharging current range	0.1-2.0A

Table 4.2 Discharger (Hitec AD350) Device Specifications

Output voltage	5V
Input voltage	5V
Current rating	40A
Discharge power	350W
Discharge current	0.1～40A

Table 4.3. All-Solid-State Battery AMP9070140 Specifications

Operating voltage	3.7V
Maximum voltage	4.2V
Charge rate	1C
Discharge rate	1C
Cell capacity	7500mAh
Battery Thickness	9mm

Table 4.4. All-Solid-State Battery AMP7197247 Specifications

Operating voltage	3.85V
Maximum voltage	4.4V
Charge rate	0.2C
Discharge rate	0.2C
Cell capacity	15000mAh
Battery Thickness	7.1mm

Table 4.5. All-Solid-State Battery AMP7197247 Specifications

Parameter	Experimental condition
Radiation	1000Gy/h
Ultrasound frequency	1MHz
Battery capacity status	9000mAh/15000mAh (max)
Radiation time	8 hours

Table 4.6 The Attenuation Coefficient of Cobalt, Carbon and Oxygen under Gamma Rays

Element	Gamma ray energy (1.17MeV)	Gamma ray energy (1.33MeV)
Cobalt	0.0670 cm^2/g	0.0588 cm^2/g
Carbon	0.0325 cm^2/g	0.0308 cm^2/g
Oxygen	0.0292 cm^2/g	0.0277 cm^2/g

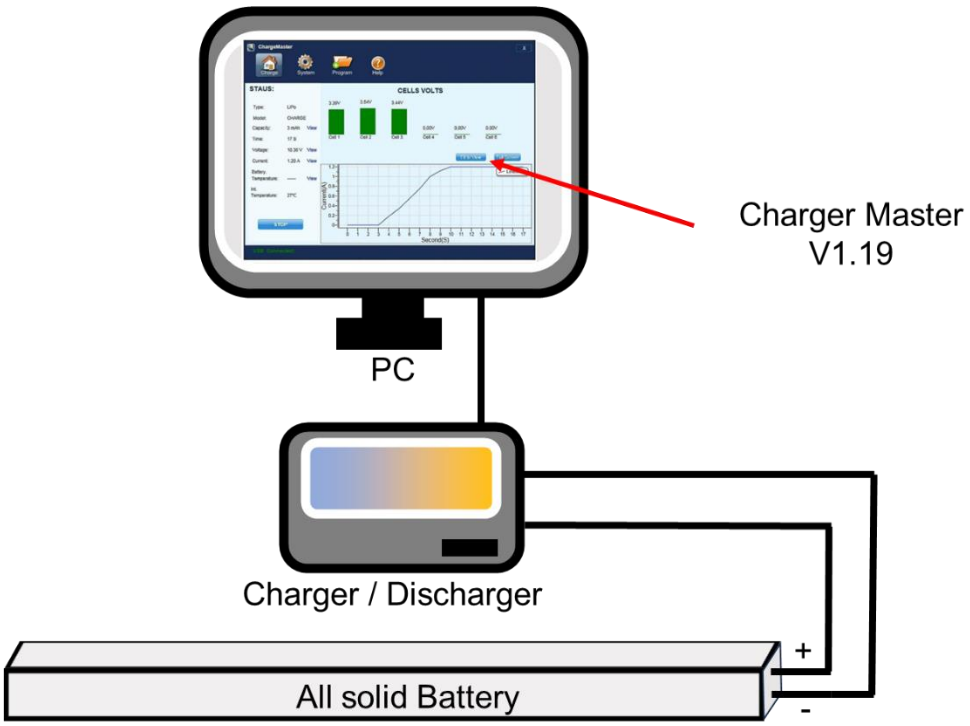

Fig.4.1 Experiment setup for ultrasonic measurement

Fig.4.2 Photo of battery in irradiation chamber

Fig.4.3 Photo of battery in irradiation chamber

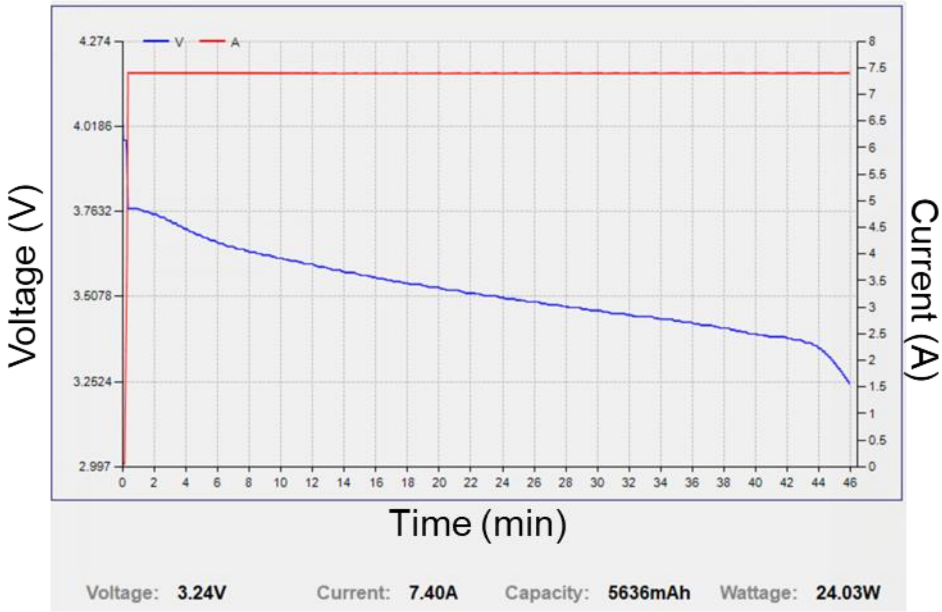

Fig4.4 Electric result for discharging (Radiation 260Gy/h)

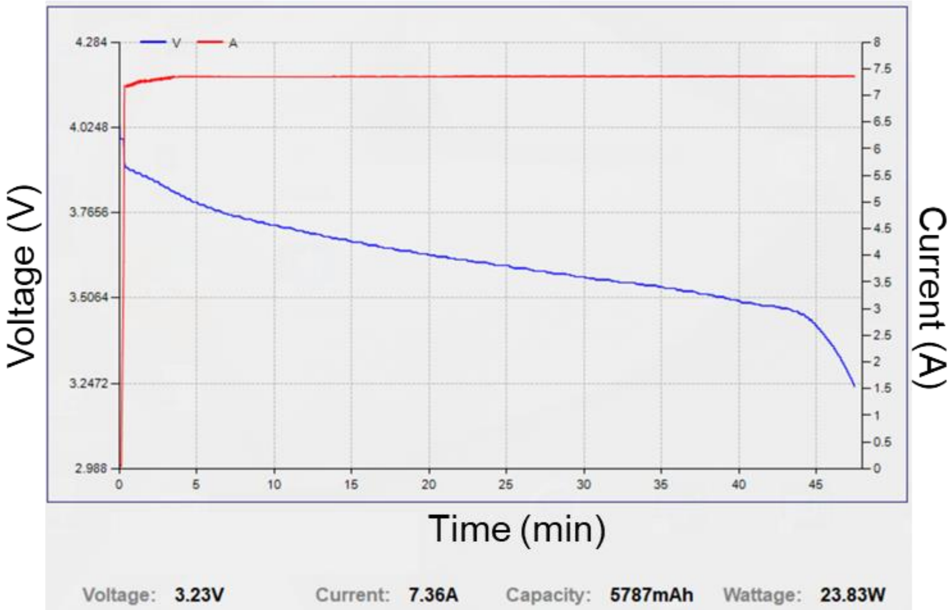

Fig4.5 Electric result for discharging (Radiation 44Gy/h)

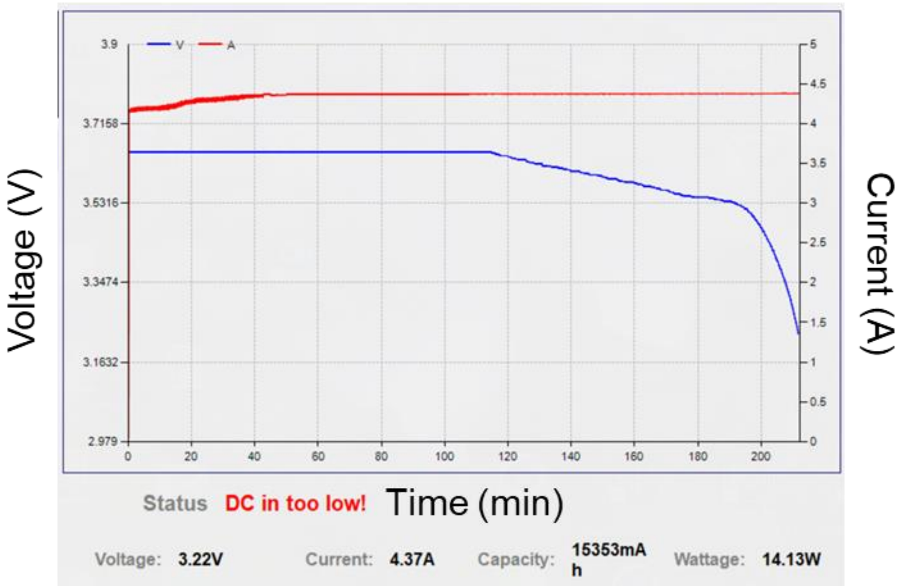

Fig4.6 Electric result for discharging (Radiation 260Gy/h)

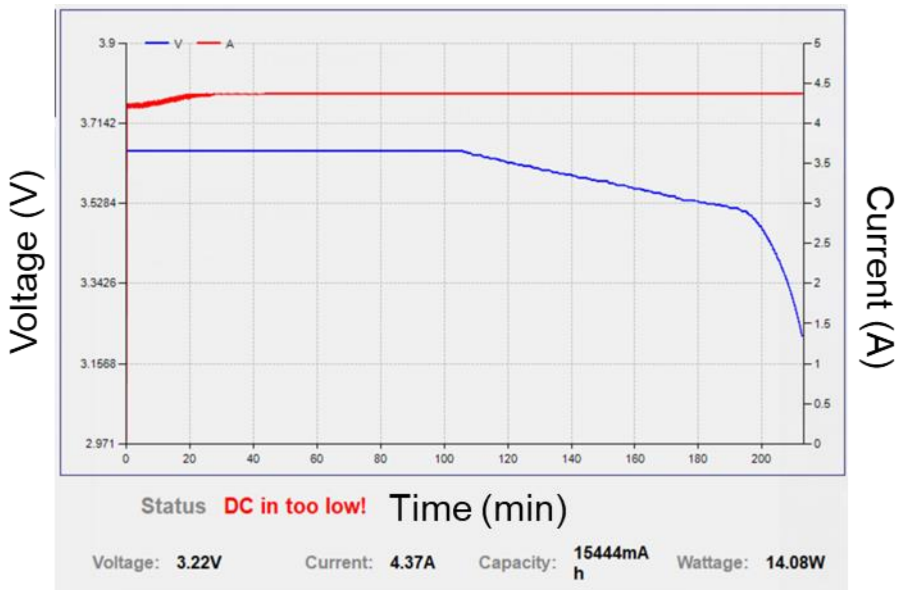

Fig4.7 Electric result for discharging (Radiation 44Gy/h)

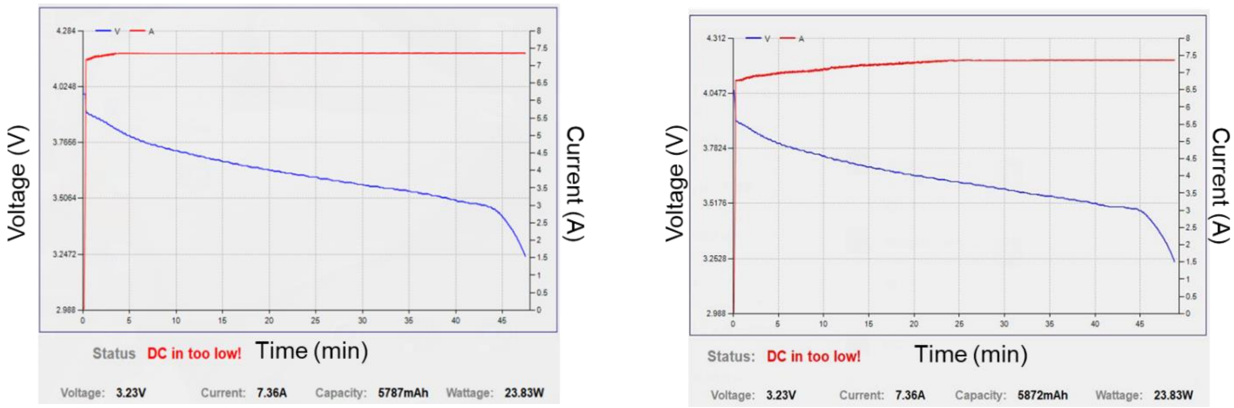

(a) Radiation environment (b) Normal environment

Fig4.8 Electric result for discharging in normal and radiation environment

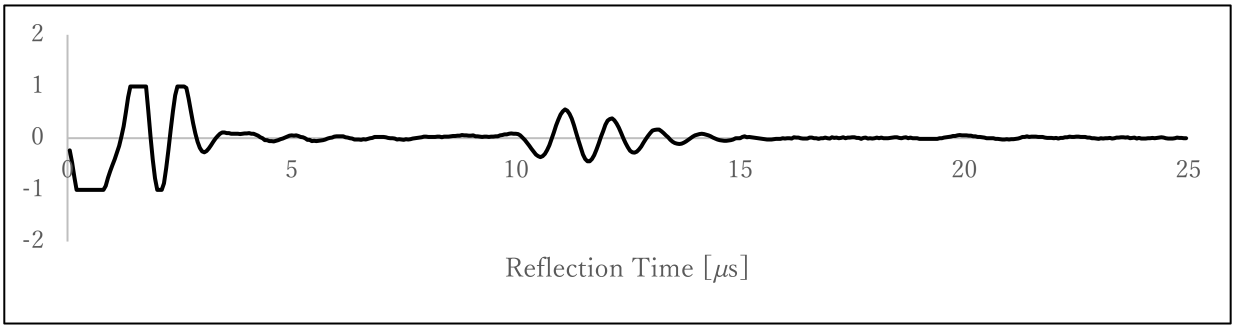

Before radiation

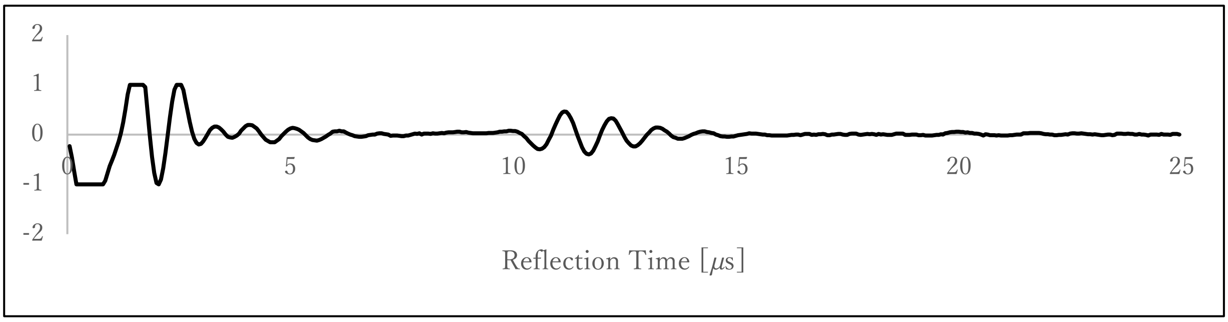

After 1 hour radiation

Fig4.9 Reflection waveform for battery before and after 1 hour radiation

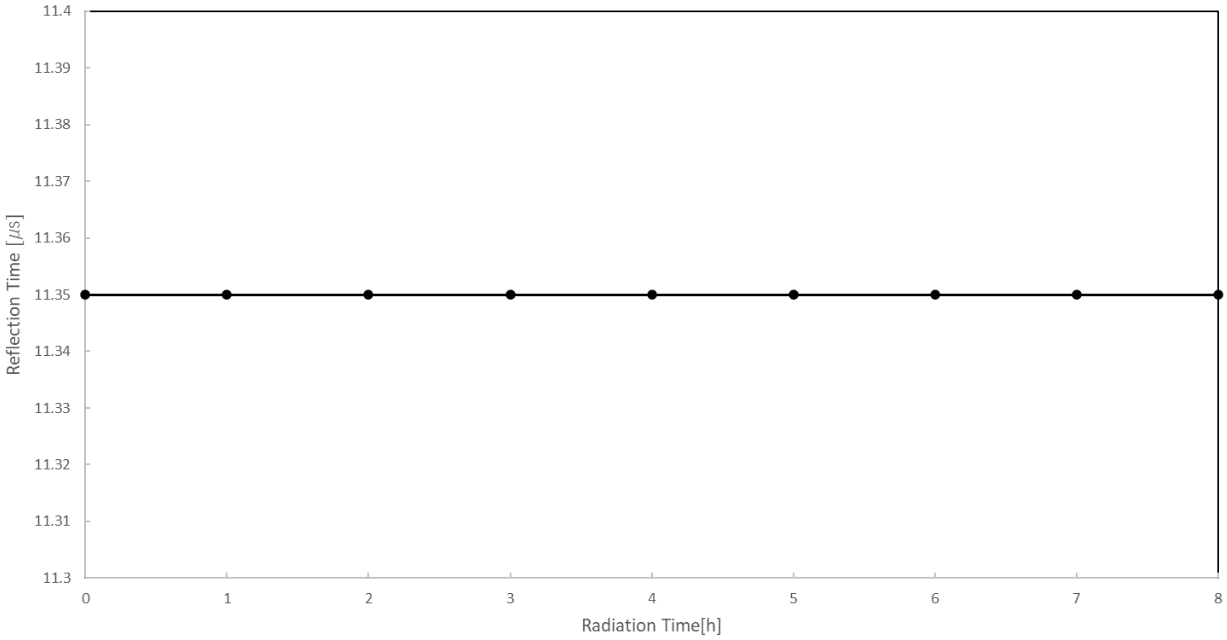

Fig.4.10 Reflection time of all-solid-state battery during 8 hours radiation

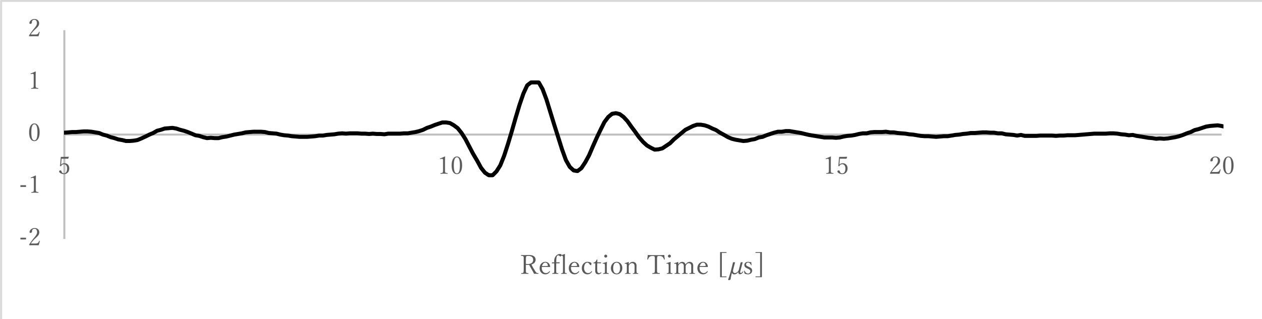

Reflection waveform of All-Solid-State AMP-Battery after radiation (0hour)

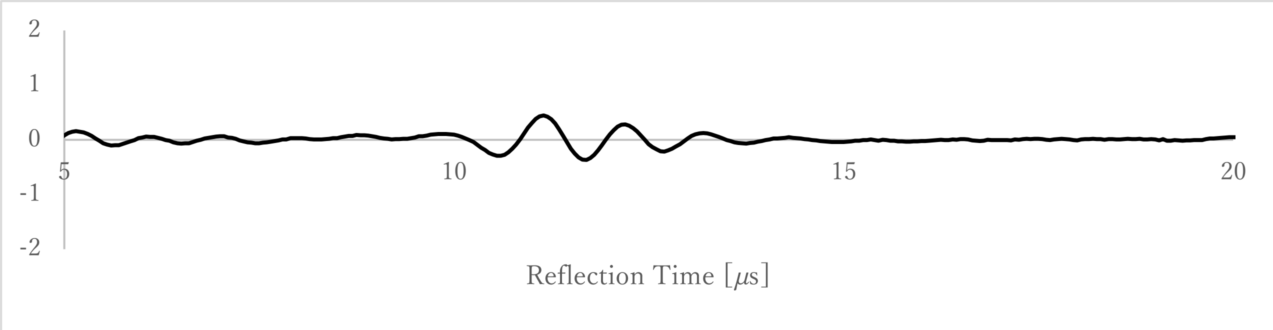

Reflection waveform of All-Solid-State AMP-Battery after radiation (24 hours)

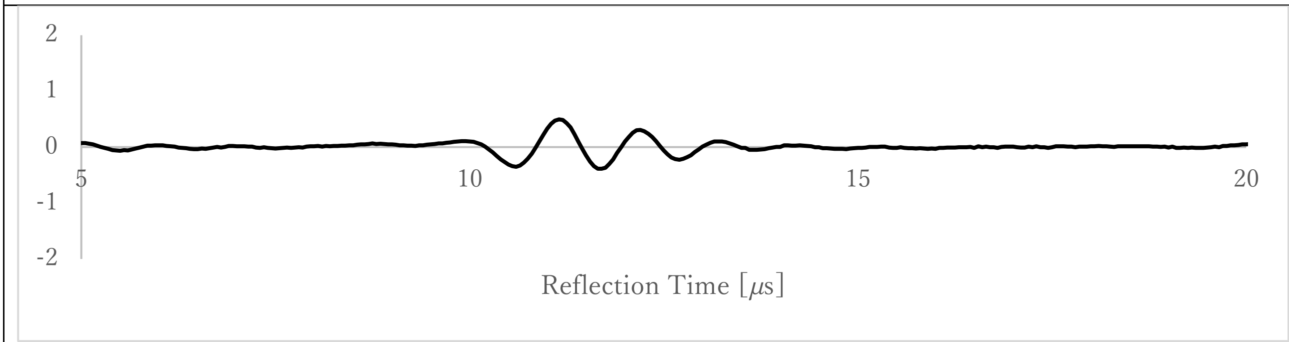

Reflection waveform of All-Solid-State AMP-Battery after radiation (48 hours)

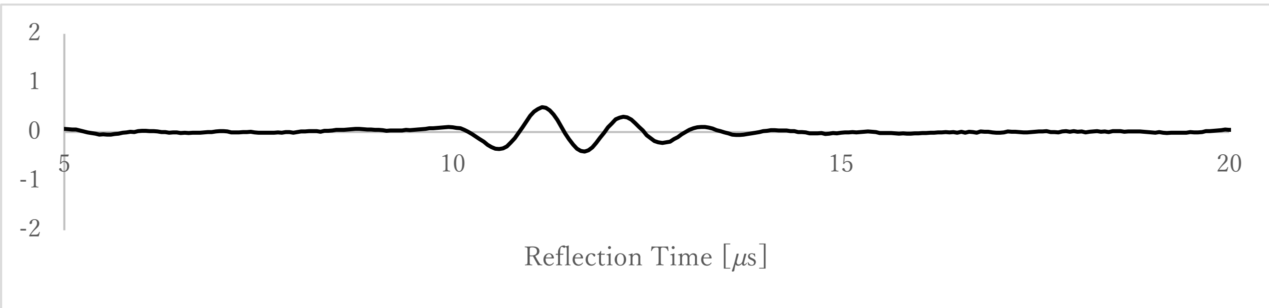

Reflection waveform of All-Solid-State AMP-Battery after radiation (72 hours)

Fig.4.11 Reflection waveform of All-Solid-State AMP-Battery after radiation for 0-72 hours

Chapter 5

Chapter5 Conclusions

5.1 Fukushima Revitalizics Front End and Back End

As a conclusion of this research, the results obtained in Chapters 2-4 are discussed on the Fukushima Revitalizics front end and back end. Figure 5.1 shows the core elements of Fukushima Revitalizics including renewable energy, education, risk communication, social experimentation, robotic measurement engineering and decontamination science. As mentioned in Chapter 1, these elements are divided into 3 parts: Front end, Inner, and Back end. For this research, Front end which is related to renewable energy and Back end which is related to decontamination science are focused on. This research provides technical solutions and contributions to the Fukushima Revitalizics front end and back end.

5.1.1 Contributions of Stone Heat Storage System (Front End)

In Chapter 2, performance evaluation of stone heat storage system has been done, highlight its potential to provide a cost-effective and efficient solution for heat energy management in Fukushima, where energy infrastructure was significantly disrupted, implementing such systems can facilitate the stabilization and optimization of local energy supply. This can be particularly beneficial for residential heating and industrial processes, promoting sustainable energy use and reducing dependence on external energy sources.

The annual electricity consumption of Namie Town residents in Fukushima for example, was 7200 MWh according to the data in 2022. Since the stone heat storage system stored excess energy from day time and then be used during periods when there is insufficient sunlight, for example in the night, in order to supply enough energy for the night usage of residents in Namie Town, the energy of heat storage system restored in the day time should be around 6570kWh, which a stone storage tank with a size of 192m^3 is enough to supply these amounts of energy when the heat to electric conversion efficiency is 25%.

5.1.2 Contributions of All-Solid-State Battery (Back End)

One of the major contributions of this study is the development and evaluation of ASSBs with superior radiation resistance. The study conducted rigorous performance tests in high-radiation environments, using a cobalt-60 irradiation chamber to expose the batteries to over 100 Gy of radiation. The results showed that these batteries maintained their electrical performance and structural integrity even after 72 hours of radiation exposure. This breakthrough is crucial for decommissioning robots operating in high-radiation environments, where conventional batteries would quickly degrade. By providing a reliable power source capable of withstanding such conditions, this study directly enhances the efficiency and safety of Fukushima decommissioning operations.

5.2 Research Prospects for Fukushima Revitalizics

5.2.1 Future Research Directions for Stone Heat Storage System

To aim for the performance improvement and practical application of heat storage system, the simulation which more similar to the real condition is necessary, the following promotion should be considered to improve the simulation data:

Model expansion for air velocity variation in porous media

Variable flow rates: In porous media, air velocity varies due to differences in porosity and structure of the medium. It is essential to consider these variations in the model to accurately capture their impact on flow and heat transfer.

Local velocity changes: The way stones are packed affects the flow paths of the gas, resulting in local velocity changes. These variations need to be captured through detailed mesh refinement and fluid dynamics simulations.

Stone stacking model

Specific stone stacking model: Replace the porous media model with a specific stone stacking model to simulate the flow of gas through the actual arrangement of stacked stones.

5.2.2 Further Applications of Ultrasound Measurement Techniques

Ultrasonic measurement technology can be applied not only to all-solid-state batteries but also to other energy storage technologies:

Application to various battery systems: Consider the application of ultrasonic measurement technology to other energy storage systems such as lithium-ion batteries and sodium-ion batteries. This will allow non-destructive observation of internal changes in various batteries, contributing to performance improvement.

Development of real-time monitoring systems: Develop real-time monitoring systems using ultrasonic measurement technology and establish techniques for practical use. This will enable real-time monitoring of battery health and early detection of abnormalities.

Application to large-scale systems: Establish monitoring and management technologies using ultrasonic measurement technology in large-scale battery systems such as energy storage systems and electric vehicles. This will enhance the reliability and efficiency of the entire system.

5.2.3 Development Prospects of Battery Technologies in Nuclear Radiation Environment

For the advancement of battery technology in nuclear radiation environments, the following research is crucial:

The performance of battery during charging and discharging under high radiation condition. In this research, radiation resistance was evaluated after the battery taken out from the radiation chamber. For the future work, radiation resistance will be evaluated using ultrasound under radiation environments.

Design of radiation-resistant batteries: Optimizing the design and structure of batteries intended for use in radiation environments is required. This includes the development of battery packaging and shielding technologies.

The results of this study represent an important step toward the further development and practical application of all-solid-state batteries. Future research should build on the insights gained from this study and continue to develop and apply more advanced battery technologies.

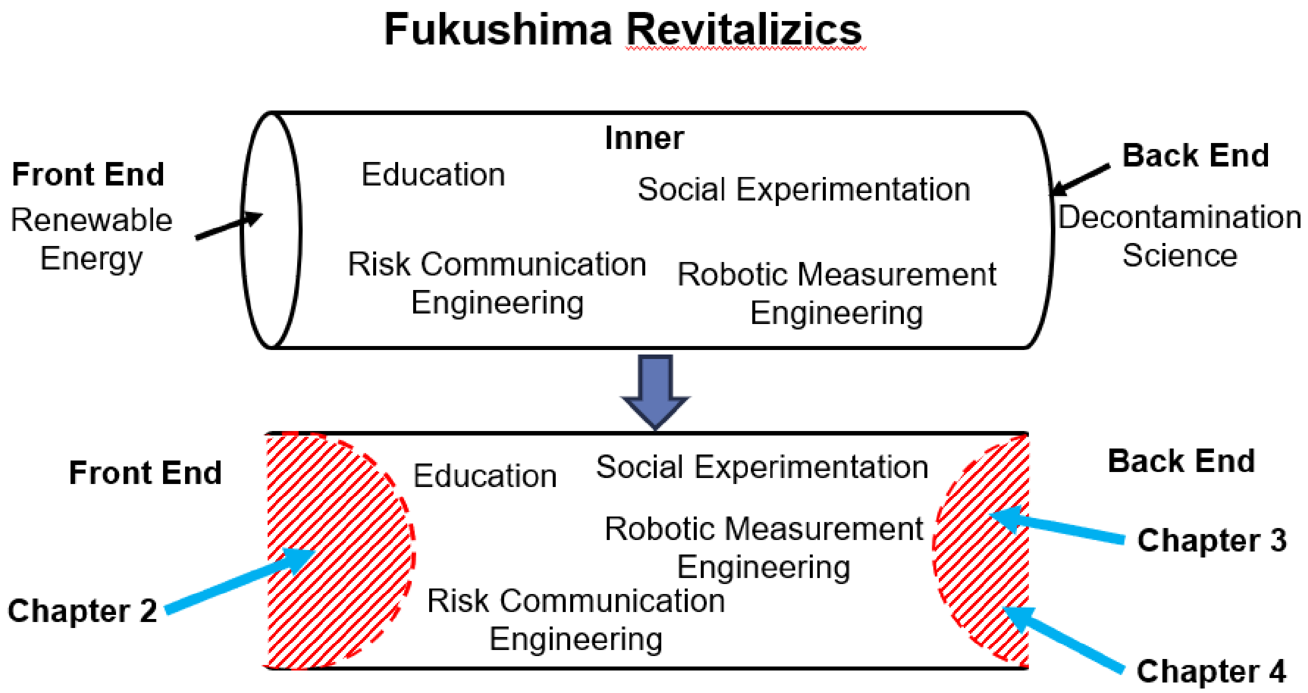

Fig.5.1 Structure of Fukushima Revitalizcs

Acknowledgments

I would like to express my deepest gratitude to Professor Kikura and Professor Tamaura for their invaluable guidance, support, and encouragement throughout my research journey. Their expertise and insights have been instrumental in shaping the direction of this study and bringing it to fruition.

I am also thankful to my colleagues and the entire research team for their collaborative spirit and assistance. Their contributions have been invaluable in conducting experiments and analyzing data.

Lastly, I would like to thank my family and friends for their unwavering support and understanding throughout this research journey. Their encouragement has been a pillar of strength, allowing me to persevere and complete this work.

This dissertation is a testament to the collective efforts and guidance of all those who have supported me, and I am deeply grateful to each one of you.